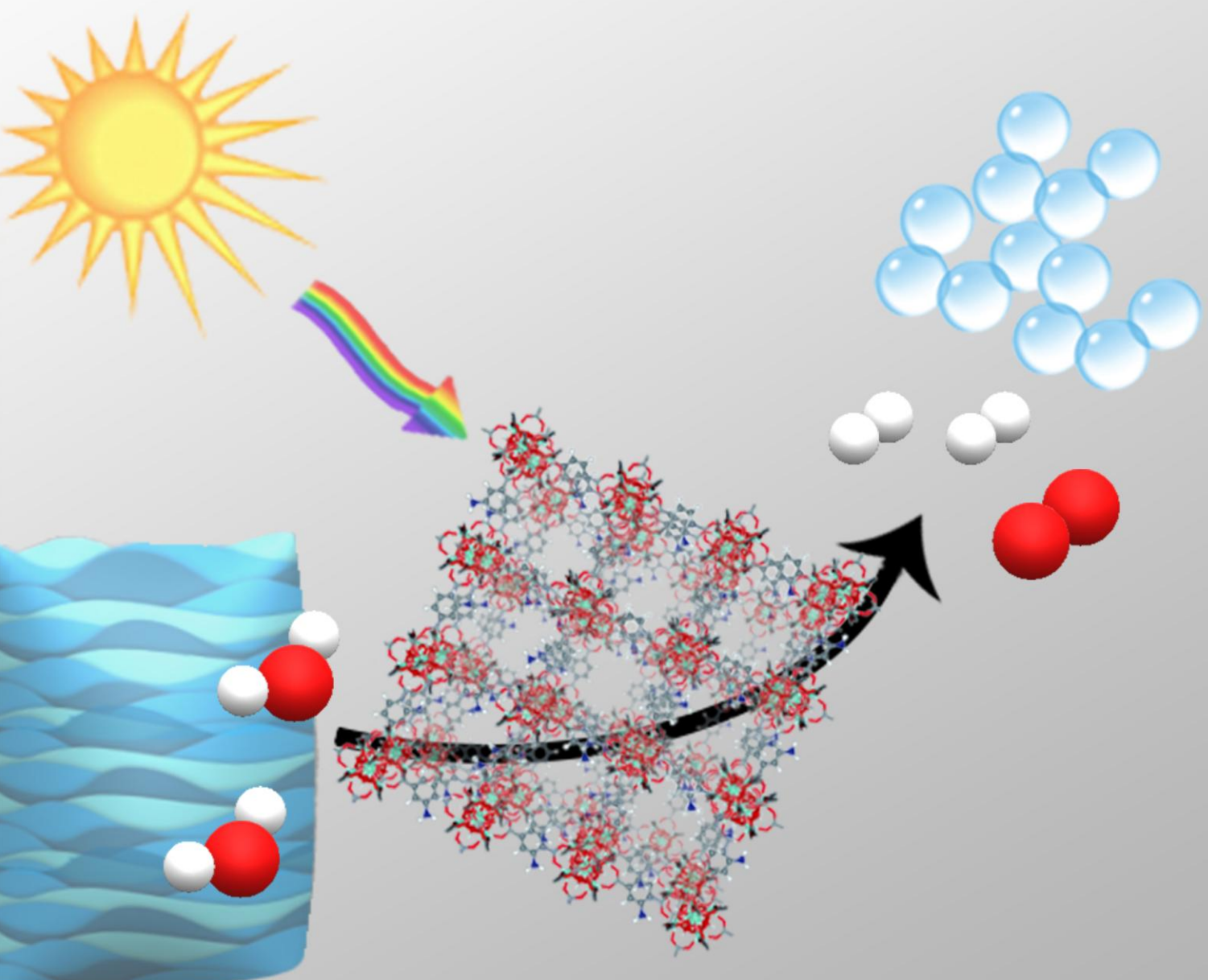


Development of Metal-Organic Frameworks for Photocatalytic Applications



Jochem Wijten

Development of Metal-Organic Frameworks for Photocatalytic applications

Masterthesis 2014-2015

By Jochem Wijten (UU-3634124)

Supervised by Dr. Monica Barroso, Dr. Jan Philipp Hofmann

and Prof. dr. ir. Bert Weckhuysen

Inorganic Chemistry and Catalysis group

Utrecht University

Financial support:



Abstract

In this research photocatalytic water splitting by metal-organic frameworks (MOFs) has been studied to replace fossil fuels by renewable energy. It has been found that MOFs can be immobilized on F:SnO₂ (FTO) as a conductive substrate. When using these photoelectrodes in photoelectrochemical tests it was observed that the materials are electrochemically unstable and that they possess no observable photoelectrochemical activity towards hydrogen generation. The metal nodes studied are based on Zr, Cu, Co and Ti, the linkers are 2-aminoterephthalic acid and 2,5-dihydroxyterephthalic acid. None of these MOFs were found to be capable of photoelectrochemical proton reduction to generate hydrogen. The MOFs were also studied as photocatalyst particles for photocatalytic activity towards proton reduction. No hydrogen evolution was observed with gas chromatography during photocatalytic tests. This agreed with the lack of photoelectrochemical activity for the photoelectrodes.

Finally to study the charge dynamics transient absorption spectroscopy was used. It was found that the charge separation in the MOFs after light absorption is mostly related to the organic linker. For MOFs with 2,5-dihydroxyterephthalic acid linkers a transient state was observed with lifetimes up to 5 ns. MOFs with 2-aminoterephthalic acid linkers show two transients, one with lifetimes up to 15 ns and another with lifetimes extending to 600 ns. The chemical transition from protons to hydrogen takes place on a microsecond scale, meaning that the competing recombination of charge carriers is at least one order of magnitude faster than the desired reaction.

This research has been conducted as part of the NIOK Solar Fuels graduate program. It was a joined research between Utrecht University and the Technical University of Eindhoven, supervised by Dr. Monica Barroso (UU), Dr. Jan Philipp Hofmann (TU/e) and Prof. dr. ir. Bert Weckhuysen (UU).

Table of Contents

List of Figures	6
List of Tables	11
1. Introduction	12
1.1. Solar to fuel energy conversion.....	13
1.1.1. Photocatalysis	14
1.1.2. Photoelectrochemistry	18
1.2 Metal-Organic Frameworks.....	21
1.2.1. MOFs as Photocatalysts and Photoelectrode materials.....	23
1.2.2. State-of-the-art	25
2. Methodology.....	29
2.1: Syntheses	29
2.1.1: Films on substrates.....	29
2.1.2: Powder samples	36
2.2: Characterization and measurements.....	39
2.2.1: X-ray diffraction	39
2.2.2: Infrared spectroscopy	39
2.2.3: Thermogravimetric analysis	40
2.2.4: Scanning electron microscopy	40
2.2.5: UV-Visible spectroscopy	40
2.2.6: Electrochemistry and photoelectrochemistry	40
2.2.7: Photocatalysis and online H ₂ detection by gas chromatography	43
2.2.8: Transient absorption spectroscopy	47
3. Results: MOF Photoelectrodes	50
3.1. Structural characterization.....	50
3.2. Photoelectrochemical characterization	58
3.3. Summary and General discussion	62
4. Results: Photocatalytic MOFs.....	64
4.1: Structural characterization.....	64
4.2: Photocatalytic tests.....	80
4.3: Photophysical characterization	81
4.4: Summary and General discussion	89
5. Conclusions	91
6. Outlook	92

References	94
Appendix	105

List of Figures

Figure 1.1: Schematic representation of a photocatalyst at work.	13
Figure 1.2: Schematic representation of charge carrier dynamics inside a semiconductor particle.	14
Figure 1.3: Schematic representation of electron trapping.	15
Figure 1.4: Band potentials for several semiconductors versus NHE at pH = 0. ^[9, 10]	16
Figure 1.5: Schematic representation of the Z-scheme.	17
Figure 1.6: Schematic representation of a semiconductor functionalized with a catalyst... ¹⁸	18
Figure 1.7: Schematic view on a complete PEC cell. On the left the photoanode is shown which performs the water oxidation. Then on the right the photocathode performs the proton reduction. A electrical bias can be applied between the electrodes.	19
Figure 1.8: Schematic representation of band bending and the effect of applying an electrical bias. A gives the representation without band bending taken into account, B a representation with band bending taking into account and C a representation where an anodic external bias is applied as well.	19
Figure 1.9: Energy diagram of an ideal combination of materials for a water splitting PEC cell. Note that band bending is omitted for clarity.	20
Figure 1.10: Energy diagram of a more realistic combination of materials for an water splitting PEC cell. Note that band bending is omitted for clarity.	20
Figure 1.11: Schematic representation of a PV-PEC cell. In the set of p-i-n junctions extra potential is generated to allow the system to perform the complete water splitting reaction. ^[20]	21
Figure 1.12: Schematic representation of two MOFs. The first is UiO-66-NH ₂ which consist of an oxometallic cluster node with Zr and 2-aminoterephthalic acid, the second is Cu ₂ (DABCO)(ATA) ₂ where the node consists of a paddlewheel structure with two Cu ²⁺ ions. Grey = C, white = H, blue = N, red = O, cyan = Zr, green = Cu. DABCO = 1,4-Diazabicyclo[2.2.2]octane, ATA =2-aminoterephthalic acid.	22
Figure 1.13: Schematic representation for the hypothesized charge carrier dynamics in photocatalytic MOFs. D represents an electron donor replenishing the electron injected into the metal node through a ligand to metal charge transfer (LMCT) where protons are reduced to hydrogen. Reductions such as proton reduction are expected to take place at the metal node, oxidations are expected to take place at the organic linker.	23
Figure 1.14: Schematic representation of a MOF immobilized on a FTO slide. In the representation the assumption is made that the MOF attaches to the FTO through the organic linker. There is no definite proof that this is indeed the case.....	25
Figure 1.15: Schematic representation of UiO-67 (upper) and the UiO-framework with tetraphenyl linkers (lower) MOFs functionalized with Ir-based complexes as linkers. After synthesis of the frameworks with the complexes Pt nanoparticles are synthesized inside the pores by photoreduction. These MOFs are then used for photocatalysis. ^[58]	26
Figure 1.16: Schematic representation of ZnO nanorods on FTO with a ZIF-8 coating. Shown is how it can select H ₂ O ₂ over ascorbic acid to perform the oxidation on ZnO. This image is taken from ref. ^[37]	27

Figure 2.1: Schematic representation of a PEC setup. Here the different electrodes, WE (working electrode), CE (counter electrode) and RE (reference electrode) are indicated. All connected to a potentiostat.....	41
Figure 2.2: Schematic representation of a photocatalytic testing setup, this particular setup is connected to a GC. The light source is indicated as well as filters cutting UV and IR radiation. The stirred reaction container is seen where proton reduction takes place and where electron donors are consumed as the oxidation half-reaction.....	44
Figure 2.3: Schematic representation of the setup for testing the photocatalytic activity. The letters represent: (A) Light source(500 W, Xe/Hg lamp), (B) Collimated condenser, (C) IR-filter (water), (D) 420 nm high-pass filter, (E) convex lens, (F) Beam splitter, (G) Photosensor, (H) Stirring plate, (I) Reactor with cooling mantel, (J) Stirring magnet, (K) Liquid with sacrificial reagent and dispersed photocatalyst, (L)&(L') manual 2- and 3-way valves resp., (M) Headspace, (O) motorized 4-way valve, (P) Pressure gauge, (Q) motorized 6-way valve, (R) 1 mL loop of tubing and (S) end caps. The numbers represent cooling water: (1) from cooler/pump, (2) from reactor to IR-filter and (3) back to cooler/pump.....	46
Figure 2.4: A schematic representation of the pump-probe measurement.....	47
Figure 2.5: Schematic representation of the TAS-setup. The black line represents the path of the pump laser beam that enters in the lower right corner, the red line represents the probe laser beam path. The acronyms stand for the following: M = Mirror, ND = Neutral density filter, L = Lens, BS = Beamsplitter, FO = Fiber optics (detectors), I = Iris (diaphragm). This image is taken from the EOS manual.....	49
Figure 3.1: XRD data for Zr(ATA)/HCl, Sur-16b (Black) and the Zr(ATA)/HCl powder, Bat-4 (Red).....	51
Figure 3.2: SEM topographs of Zr(ATA)/HCl, Sur-16b at different magnifications. Scale bars are indicated.....	51
Figure 3.3: IR spectra of Zr(ATA)/HCl, Sur-20 (Blue) and the Zr(ATA)/HCl powder Bat-4 (Red).....	52
Figure 3.4: Transmission UV-Vis spectra of Zr(ATA)/HCl, Sur-16c (Black), Sur-20 (Blue) and the Reflectance UV-Vis spectrum of the Zr(ATA)/HCl powder Bat-4 (Red).....	52
Figure 3.5: XRD data for Cu(DABCO)(ATA)/DQ, Sur-17 (Black) and the Cu(DABCO)(ATA)/DQ powder, Bat-11 (Red).....	53
Figure 3.6: IR spectra for Cu(DABCO)(ATA)/DQ, Sur-9 (Blue) and the Cu(DABCO)(ATA)/DQ powder, Bat-11 (Red).....	53
Figure 3.7: Transmission UV-Vis spectrum for Cu(DABCO)(ATA)/DQ, Sur-17 (Black) and the reflectance UV-Vis spectrum for the Cu(DABCO)(ATA)/DQ powder Bat-11 (Red)....	54
Figure 3.8: XRD data for Co(ATA)/DQ, Sur-18_1 (Black) and Sur-18_2 (Red) and the Co(ATA)/DQ powder, Bat-17 (Blue).....	55
Figure 3.9: IR spectra for Co(ATA)/DQ, Sur-18_1 (Black) and the Co(ATA)/DQ powder, Bat-17 (Blue).....	55
Figure 3.10: Reflectance UV-Vis spectra for Co(ATA)/DQ, Sur-18_1 (Black) and the Co(ATA)/DQ powder, Bat-17 (Blue).....	56
Figure 3.11: XRD data for Ti(DHTA)/DQ, Sur-19 (Black) and the Ti(DHTA)/DQ powder Bat-21 (Red)	56
Figure 3.12: IR spectra for Ti(DHTA)/DQ, Sur-19 (Black) and the Ti(DHTA)/DQ powder Bat-21 (Red)	57
Figure 3.13: Transmission UV-Vis spectrum for Ti(DHTA)/DQ, Sur-19 (Black) and reflectance UV-Vis spectrum for the powder Ti(DHTA)/DQ Bat-21 (Red)	57

Figure 3.14: SEM topographs of Ti(DHTA)/DQ, Sur-19 at different magnifications. Scale bars are indicated.....	58
Figure 3.15: CV of Zr(ATA)/HCl, Sur-1a for 4 cycles, first 3 in the dark, last under illumination. The electrolyte used was water buffered with phosphates at pH 6.8. Potentials are given versus a Ag/AgCl counterelectrode.....	59
Figure 3.16: CV of Zr(ATA)/HCl, Sur-16, for 3 cycles in the dark. The third cycle of a measurement on bare FTO is seen as a reference (Black). This measurement is performed in an MeCN based electrolyte with a non-aqueous Ag/Ag ⁺ reference electrode.....	60
Figure 3.17: CV of Cu(DABCO)(ATA)/DQ, Sur-17, for 3 cycles in the dark. The third cycle of a measurement on bare FTO is given as a reference (Black). This measurement is performed in an MeCN based electrolyte with a non-aqueous Ag/Ag ⁺ reference electrode.....	60
Figure 3.18: CV of Co(ATA)/DQ, Sur-18, for 3 cycles in the dark. The third cycle of a measurement on bare FTO is given as a reference (Black). This measurement is performed in an MeCN based electrolyte with a non-aqueous Ag/Ag ⁺ reference electrode.....	61
Figure 3.19: CV of Ti(DHTA)/DQ, Sur-19, for 3 cycles in the dark. The third cycle of a measurement on bare FTO is given as a reference (Black). This measurement is performed in an MeCN based electrolyte with a non-aqueous Ag/Ag ⁺ reference electrode.....	62
Figure 4.1: XRD data for Zr(ATA)/HCl, Bat-4 (Black), Zr(DHTA)/HCl, Bat-8 (Red) and Zr(ATA)(DHTA)/HCl, Bat-14 (Blue).	64
Figure 4.2: XRD data for Zr(ATA)/HCl, Bat-4 before (Black) and after (Red) activation....	65
Figure 4.3: XRD data for Zr(ATA)/HCl, Bat-4 (Black) and Zr(ATA)/DQ, Bat-5 (Green).	65
Figure 4.4: IR spectra of Zr(ATA)/HCl, Bat-4 (Black), Zr(DHTA)/HCl, Bat-8 (Red) and Zr(ATA)(DHTA)/HCl, Bat-14 (Blue).	66
Figure 4.5: IR spectra of Zr(ATA)/HCl, Bat-4 before (Black) and after (Red) activation....	67
Figure 4.6: TGA profiles of Zr(ATA)/HCl, Bat-4 (Black), Zr(DHTA)/HCl, Bat-8 (Red) and Zr(ATA)(DHTA)/HCl, Bat-14 (Blue) before activation.....	68
Figure 4.7: TGA profiles of Zr(ATA)/HCl, Bat-4 before (Black) and after activation (Red).68	
Figure 4.8: SEM topographs of the different Zr-MOFs, A & B for Zr(ATA)/HCl, Bat-4, C & D for Zr(ATA)/DQ, Bat-5, E & F for Zr(DHTA)/HCl, Bat-8 and G & H for Zr(ATA)(DHTA)/HCl, Bat-14. The images in the left column all have the same scale, as do all the images in the right column. Scale bars are indicated.....	69
Figure 4.9: XRD data for Cu(DABCO)(ATA)/DQ MOFs, Bat-11 before (Black) and after (Red) activation and Bat-16 (Blue).....	70
Figure 4.10: IR spectra of Cu(DABCO)(ATA)/DQ MOFs, Bat-11 before activation (Black) and Bat-16 (Blue).....	71
Figure 4.11: TGA profile of Cu(DABCO)(ATA)/DQ, Bat-11. The weight loss at 50 °C is considered an artefact.....	72
Figure 4.12: SEM topographs of the Cu(DABCO)(ATA)/DQ MOFs, Bat-11 (A and B) and Bat-16 (C and D). Scale bars are indicated in the images.....	72
Figure 4.13: XRD data for Co(ATA)/DQ, Bat-17 (Black) and Co(DABCO)(ATA)/DQ, Bat-18 (Red).....	73
Figure 4.14: IR spectra of Co(ATA)/DQ, Bat-17 (Black) and Co(DABCO)(ATA)/DQ, Bat-18 (Red).	74

Figure 4.15: TGA profiles for both Co(ATA)/DQ, Bat-17 (Black) and Co(DABCO)(ATA)/DQ, Bat-18 (Red).....	74
Figure 4.16: SEM topographs of Co(ATA)/DQ, Bat-17 (A and B) and Co(DABCO)(ATA)/DQ, Bat-18 (C and D). Scale bars are indicated.....	75
Figure 4.17: XRD data of Ti(ATA)/DQ (Bat-19, Green), Ti(ATA)/HCl (Bat-20, Purple) and Ti(ATA)/MeOH synthesized for 24 hours (Bat-26, Black) and 72 hours (Bat-27, Red) and the dried filtrate of the latter (Bat-27-F, Blue).....	76
Figure 4.18: XRD data of Ti(DHTA)/DQ (Bat-21, Green and Bat-25, Yellow), Ti(DHTA)/HCl (Bat-22, Purple), Ti(DHTA)/AcOOH (Bat-23, Orange) and Ti(DHTA)/MeOH synthesized for 24 hours (Bat-28, Black) and for 72 hours (Bat-29, Blue) and the dried filtrate of the latter (Bat-29-F, Red).....	76
Figure 4.19: XRD data of the dried filtrates of Ti(ATA)/MeOH (Bat-27-F, Blue) and Ti(DHTA)/MeOH (Bat-29-F, Red) synthesized for 72 hours.....	77
Figure 4.20: IR spectra of the Ti-MOFs Ti(ATA)/MeOH, Bat-27-F (Blue) and Ti(DHTA)/MeOH, Bat-29-F (Red).....	77
Figure 4.21: TGA profiles for the Ti-MOFs Ti(ATA)/MeOH, Bat-27-F (Green), Ti(DHTA)/HCl, Bat-22 (Purple), Ti(DHTA)/MeOH, Bat-28 (Black), Ti(DHTA)/MeOH, Bat-29 (Blue) and Ti(DHTA)/MeOH, Bat-29-F (Red).....	78
Figure 4.22: SEM topographs of the different Ti-MOFs, A & B for Ti(ATA)/HCl, Bat-20, C & D for Ti(ATA)/MeOH (24h), Bat-26, E & F for Ti(ATA)/MeOH (72h, Filtrate), Bat-27-F and G & H for Ti(DHTA)/MeOH (24h), Bat-28.	79
Figure 4.23: Hydrogen evolution over time for several mixtures. Shown are Zr(ATA)/DQ (Bat-9) with TEA in a phosphate buffer (Black), TEA in a phosphate buffer (Red), the phosphate buffer (Blue) and of the empty vessel (Green).....	80
Figure 4.24: Hydrogen evolution over time for Zr(ATA)/DQ (Bat-9) in a mixture of water en methanol (Black) and the empty vessel (Green).....	81
Figure 4.25: UV-Vis data of the UiO-66 MOFs. The MOFs shown are Zr(ATA)/HCl, Bat-4 (Black), Zr(ATA)/DQ, Bat-5 (Green), Zr(DHTA)/HCl, Bat-8 (Red), Zr(DHTA)/DQ, Bat-9 (Orange), Zr(ATA)(DHTA)/HCl, Bat-14 (Blue) and Zr(ATA)(DHTA)/DQ, Bat-15 (Purple). All data is from the MOFs after activation.....	82
Figure 4.26: UV-Vis data of the Cu(DABCO)(ATA)/DQ MOFs. The MOFs shown are Bat-11 (Black) and Bat-16 (Blue). The data for Bat-11 is after activation.....	82
Figure 4.27: UV-Vis data of the Co-MOFs. The MOFs shown are Co(ATA)/DQ (Bat-17, Black) and Co(DABCO)(ATA)/DQ (Bat-18, Red).....	83
Figure 4.28: UV-Vis data of the Ti-MOFs. The MOFs shown are Ti(ATA)/DQ and Ti(ATA)/HCl (Bat-19 and Bat-20, Black and Red respectively) and Ti(DHTA)/DQ, Ti(DHTA)/HCl and Ti(DHTA)/AcOOH (Bat-21, Bat-22, and Bat-23, Green, Blue and Purple respectively).....	83
Figure 4.29: A) Transient absorption spectra for Zr(DHTA)/HCl, Bat-8. B) Transient absorption decay traces probed at 608 nm, 554 nm and 465 nm. The pump laser beam power was 0.972 mW and the measurement was performed for 22min45s.....	84
Figure 4.30: A) Transient absorption spectra for Zr(DHTA)/DQ, Bat-9. B) Transient absorption decay traces probed at 554 nm and 436 nm. TAS data for. The pump laser beam power was 1.017 mW and the measurement was performed for 16min47s.....	85
Figure 4.31: A) Transient absorption spectra for Zr(ATA)(DHTA)/HCl, Bat-14. B) Transient absorption decay traces probed at 608 nm, 581 nm, 554 nm, 465 nm and 425 nm. The pump laser beam power was 1.745 mW and the measurement was performed for 30min56s.....	85

Figure 4.32: A) Transient absorption spectra for Zr(ATA)(DHTA)/DQ, Bat-14. B) Transient absorption decay traces probed at 608 nm, 581 nm, 554 nm, 504 nm, 465 nm and 425 nm. The pump laser beam power was 1.745 mW and the measurement was performed for 30min56s. This is the same data as given in Figure 4.31 only now at longer timescales. 86

Figure 4.33: A) Transient absorption spectra for Cu(DABCO)(ATA)/DQ, Bat-16. B) Transient absorption decay traces probed at 581 nm, 504 nm and 425 nm. The pump laser beam power was 0.978 mW and the measurement was performed for 30min44s. 87

Figure 4.34: A) Transient absorption spectra for Co(ATA)/DQ, Bat-17. B) Transient absorption decay traces probed at 581 nm, 504 nm and 425 nm. The pump laser beam power was 0.992 mW and the measurement was performed for 24min08s. 87

Figure 4.35: A) Transient absorption spectra for Ti(ATA)/MeOH, Bat-26. B) Transient absorption decay traces probed at 581 nm, 504 nm and 425 nm. The pump laser beam power was 0.980 mW and the measurement was performed for 22min24s. 88

Figure 4.36: A) Transient absorption spectra for Ti(DHTA)/MeOH, Bat-28. B) Transient absorption decay traces probed at 608 nm, 554 nm and 465 nm TAS data for. The pump laser beam power was 0.925 mW and the measurement was performed for 22min22s. 89

Figure A.1: CV of bare FTO, for 3 cycles in the dark. This measurement is performed in an MeCN based electrolyte with a non-aqueous Ag/Ag⁺ reference electrode. 107

Figure A.2: TAS of data Cu(DABCO)(ATA), Bat-11. In A representative spectra are shown at different time delays. B gives the kinetic traces at different wavelengths. 108

Figure A.3: TAS of data Cu(DABCO)(ATA), Bat-16 before purging with N₂. In A representative spectra are shown at different time delays. B gives the kinetic traces at different wavelengths. 108

Figure A.4: TAS of data Co(DABCO)(ATA), Bat-18. In A representative spectra are shown at different time delays. B gives the kinetic traces at different wavelengths. 109

Figure A.5: TAS of data Co(ATA), Bat-17 before purging with N₂. In A representative spectra are shown at different time delays. B gives the kinetic traces at different wavelengths. 109

List of Tables

Table 2.1: Details of the preparation of proto-MOF solutions	30
Table 2.2: Parameters of several solvothermal syntheses on FTO. The number given in the name corresponds to the number of the proto-MOFs presented in Table 2.1.....	30
Table 2.3: Parameters of several solvothermal syntheses on FTO.....	33
Table 2.4: Parameters of dropcasting experiments.....	34
Table 2.5: Synthesis parameters of the different powder samples.....	37
Table 4.1: Collection of lifetimes per MOF. The short lifetime is given in the middle row. The longer lifetime is given in the last row if it was observed.	90
Table A1: List of chemicals used in this work.....	105

1. Introduction

Nowadays easy to process fossil fuel sources are getting more scarce. Apart from that we are experiencing a climate change due to increasing CO₂ emissions. As an example 3.23×10^{13} kg of CO₂ was emitted in 2012 worldwide.^[1] Last year the total energy consumed was 93.2×10^{24} J, of which 36.5×10^{24} J was electric energy and 25.7×10^{24} J was for transport. Only 9.1×10^{24} J (9.8% of total energy demand) was produced by alternative energy sources.^[1] Keeping with this trend will cause the amount of greenhouse gasses emitted to reach critical levels beyond which climate changes cannot be contained anymore.^[1, 2]

To prevent these problems from escalating even further alternative, carbon-free, sources of energy should be used more.^[2-4] One can think of electricity being generated without burning carbon-based fuels such as the generation of electricity using wind turbines or solar panels, which contributed 4.7×10^{24} J, i.e. 12.9% of total electric energy demand in 2014. Another possibility is to directly produce fuels from alternative sources, for transportation, which contributed 1.2×10^{24} J (4.7% of total fuel demand) to that sector last year.^[1] Converting water or CO₂ into fuels using renewable energy sources to work towards a CO₂ deficient or neutral system would be most efficient to mitigate the current environmental problems.^[3, 4]

One of the most promising sources of alternative energy is solar energy.^[5-7] For decades, research in the field of photovoltaics has improved the conversion of solar energy into electric energy. However, long-term storage and the implementation of this energy into transport is still challenging. This is why only 0.38×10^{24} J of energy was produced last year using sunlight, and only in the form of electricity. This value corresponds to 1.0% of the total electric energy consumed.^[1]

Long-term storage is necessary since sunlight does not reach the earth's surface continuously. For example in the winter there is generally much less sunlight reaching the solar panels. This can result in power shortages during such periods. On the other hand during summer there can be too much sunlight which case the capacity of the electric net could be transcended, this occurred in Germany in 2012 for example.^[1, 7]

One alternative solution to this problem is to store the energy chemically instead of electrically. Energy which is stored chemically can be stored for longer spans of time. Chemically storing solar energy is most often done by water splitting. Photocatalytic water splitting results in hydrogen and oxygen. Photocatalytically generated hydrogen is commonly referred to as a solar fuel.^[7] Another way of storing energy chemically is by reducing CO₂ to compounds like CO or CH₄.^[3, 8] These compounds can then be implemented in existing industrial processes, replacing fossil fuel based carbon compounds.

1.1. Solar to fuel energy conversion

Water can be split into hydrogen and oxygen by using sunlight. However, it does not occur by simply illuminating a container of water. To be able to split water with sunlight a photocatalyst is necessary. The process of using a photocatalyst to capture and convert sunlight is illustrated in Figure 1.1. This catalyst is typically a semiconductor, so that light can be absorbed and promote an electronic transition from the valence band to the conduction band (Green arrow, Figure 1.1). Once excited, these electrons can either fall back into the valence band by emitting a photon or heat (Red arrow, Figure 1.1), or perform redox reactions.^[3-7, 9, 10]

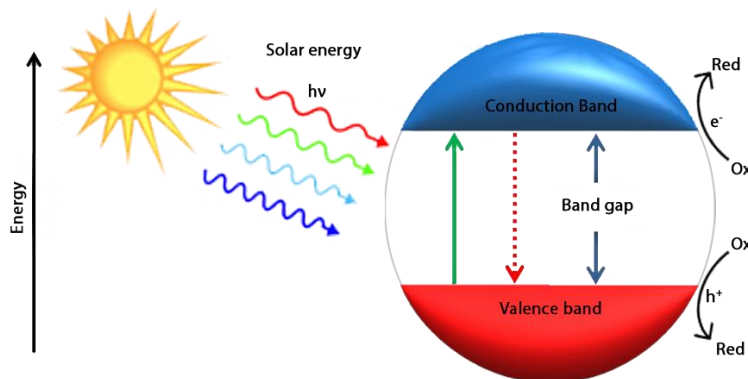
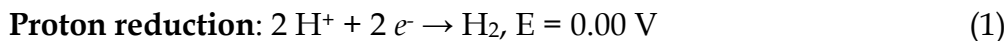


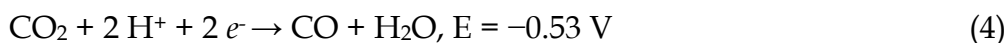
Figure 1.1: Schematic representation of a photocatalyst at work.

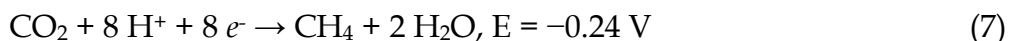
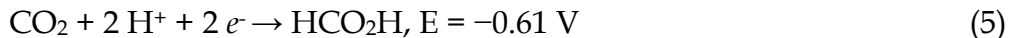
When considering photocatalytic water splitting, the redox half-reactions in question are proton reduction (1) and water oxidation (2), as described below. The overall conversion of water into H₂ and O₂ is described by (3). In the equations the reduction potentials of the redox half-reactions is reported versus a normal hydrogen electrode (NHE) at pH = 0, 25 °C, 1 atm and 1 M of each participant in the reaction.^[6]



Under standard conditions the Gibbs energy change for the total reaction (3) is 237.2 kJ/mol corresponding to an electrochemical potential of 1.23 eV. This means that for the full water splitting reaction to take place, four photons with a wavelength of 1008 nm or lower should be absorbed by the semiconductor photocatalyst. This energy of 1.23 eV is the thermodynamic barrier for this reaction however. Both the oxidation and reduction half-reactions have associated kinetic barriers, which will translate into an overpotential for the overall reaction. Due to these typical kinetic barriers the bandgap of a semiconductor, to be suitable for the direct conversion of water into H₂ and O₂, should at least be 1.6 eV, corresponding to photons of 775 nm or lower.^[7]

CO₂ reduction, on the other hand can yield different products. Examples are given in (4) to (7), where the values for E are reported versus a NHE at pH = 7, 25 °C, 1 atm and 1 M of each participant in the reaction apart from H⁺.^[3-5, 8]





As is the case with water oxidation, for CO₂ reduction an overpotential is required to overcome kinetic barriers. Such a kinetic barrier can be relatively high since some of these reactions require eight protons and eight electrons in total. The transformations occurring when reducing CO₂ are reported to be proton-coupled electron transfers (PCETs), which means an electron and a proton are transferred in a concerted manner in the reaction. Since the reduction of CO₂ to CO₂^{•-} is thermodynamically very unfavourable, requiring a potential of -1.90 V versus a NHE at pH = 7, it is avoided by the system by these concerted transfers, yielding for example formate.^[3]

1.1.1. Photocatalysis

Production of fuels from water or CO₂ is done by using photocatalysts. These catalysts are semiconductors. In these materials electron states are so close in energy that electrons can move between them using thermal energy. This results in energy bands being present in such materials. The energy gap between the bands cannot be bridged by thermal energy at ambient conditions however. This gap in energy is called the bandgap.^[9, 10]

The highest occupied band is only partially filled electrons can move freely between occupied and unoccupied states, resulting in a conductor. If however all states in the this band are occupied, electrons cannot move around freely. Such materials are semiconductors or insulators. In these materials the highest occupied band is called the valence band, the lowest unoccupied band is the conduction band. The difference between those two bands is the bandgap of the material. For semiconductors the bandgap is smaller than 3.5 eV, for insulators the gap is larger than 3.5 eV.^[5, 6, 9-13]

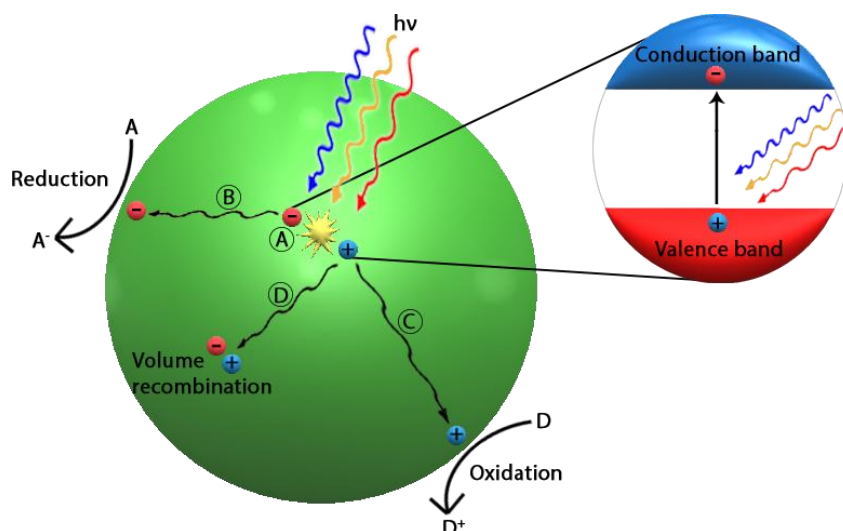


Figure 1.2: Schematic representation of charge carrier dynamics inside a semiconductor particle.

In semiconductors electrons can be promoted from the valence band to the conduction band by absorbing photons. This only happens if the photon has energy higher than that of the semiconductor's bandgap. This process is illustrated in the inset of Figure 1.2. The bandgap of a material thus determines the fraction of the light spectrum that can be absorbed.^[9, 10]

Figure 1.2A illustrates the generation of charge carriers in the semiconductor due to light absorption. The vacancy the electron leaves in the valence band, is named a hole. These charge carriers can then either travel to the surface of the material, illustrated by B and C, or they get trapped in the bulk of the material and recombine, illustrated by D. In the case of B and C the charge carriers are trapped in surface states, where they can either recombine, or react with adsorbed species at the surface. Electrons can be donated to electron acceptors, for example H^+ , and holes can be filled by electron donors like water.^[5, 6, 9-13]

The mentioned trapping of charge carriers is illustrated for electrons in Figure 1.3. When an charge carrier is trapped, the probability of recombining is lowered, thus the lifetime of the separated charges is extended. Bulk traps occur for example due to defects in the semiconductor material. Such a defect results in discontinuity in the energy band. The charge carrier can then get stuck in such an energy well and can no longer participate in redox reactions. The charge either will be recombined in this trap state or eventually be detrapped and participate in other processes.^[10]

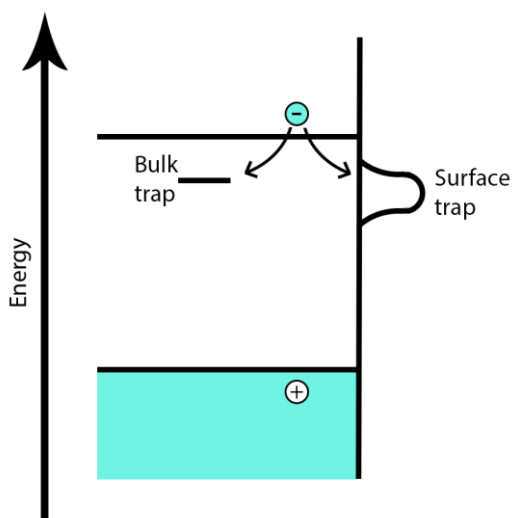


Figure 1.3: Schematic representation of electron trapping.

Surface trap states occur mainly due to adsorbed species. The electric interaction between the semiconductor and adsorbate results in an energy well where the charge carrier gets trapped. Since the carrier is now trapped at the surface of the material it can participate in redox reactions or recombine. Since surface trap states depend on adsorbates they can be influenced by changing the surrounding electrolyte. For example changing the pH affects these states. This can be used to improve the charge carrier density at the surface.^[10]

Not every semiconductor can perform the desired redox reactions. Not only the charge carrier dynamics inside the material are important but also the potentials of the bands. Figure 1.4 shows the potentials of the conduction and valence bands of several semiconductors. To perform a reduction the potential of the conduction band of a material should be more negative than the potential of the redox couple. For oxidation reactions the potential of the valence band should be more positive than that of the redox couple.^[5, 6, 9, 10, 12]

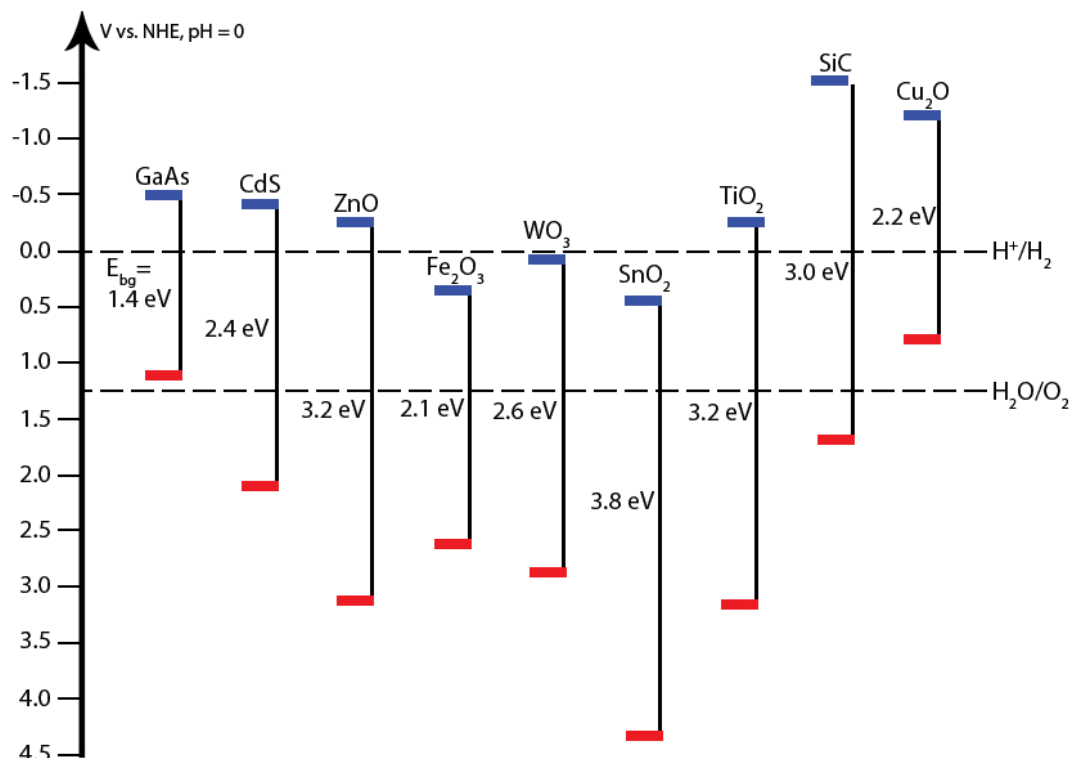


Figure 1.4: Band potentials for several semiconductors versus NHE at pH = 0.^[9, 10]

The first experimental demonstration of photocatalytic water splitting was done by Fujishima and Honda using TiO₂ particles.^[14] As can be seen in Figure 1.4 the potentials of both water splitting redox couples are positioned inside the bandgap of TiO₂. This means that TiO₂ is thermodynamically suitable to perform the complete water splitting reaction. The problem with TiO₂ is that it has a wide bandgap of 3.2 eV meaning it absorbs only in the UV region, up to 400 nm, of the light spectrum. This is the case for most semiconductors with suitable band potentials.^[9, 10, 14]

This is not true for all semiconductors however. Fe₂O₃ for example has a bandgap of about 2.1 eV meaning it can absorb light with wavelengths up to 600 nm, meaning a significant portion of the visible light can be used. The potential of its valence band is suitable to perform the water oxidation reaction, but the potential of the conduction band is too positive to reduce protons. This means materials like Fe₂O₃ are unsuitable to perform the complete water splitting reaction. There are also materials capable of proton reduction but not water oxidation, Cu₂O is an example of this with a bandgap of 2.2 eV, absorbing light up to 570 nm.^[9, 10]

There are a few semiconductors which have a relatively low bandgap and suitable band positions however. An example of this is CdS with a bandgap of 2.4 eV, absorbing light up to 520 nm. These materials, however, tend to be unstable under water splitting reaction conditions, and are often based on expensive and toxic components like Cd. In the case of CdS the S²⁻ gets oxidized to S instead of water being oxidized. This also results in toxic Cd²⁺ ions leaching into solution.^[9]

Materials which can perform only one half-reaction are not useless however. To be able to make use of the visible light response of these materials while still completely splitting water the two semiconductors can be combined. In a hypothetical example Fe₂O₃ particles to oxidize water can be combined with Cu₂O particles to reduce protons would complete the water splitting reaction. This strategy mimics the Z-scheme in natural photosynthetic systems. After the half-reactions have occurred, the electrons remaining on Fe₂O₃ will have to recombine with the holes on Cu₂O, this can be facilitated by using a redox mediator. A redox mediator is a couple like Fe²⁺/Fe³⁺ or IO³⁻/I⁻. A suitable redox couple will have a redox potential between the potentials of the Fe₂O₃ conduction band and Cu₂O valence band. The Z-scheme is illustrated in Figure 1.5.^[5, 6, 11, 12]

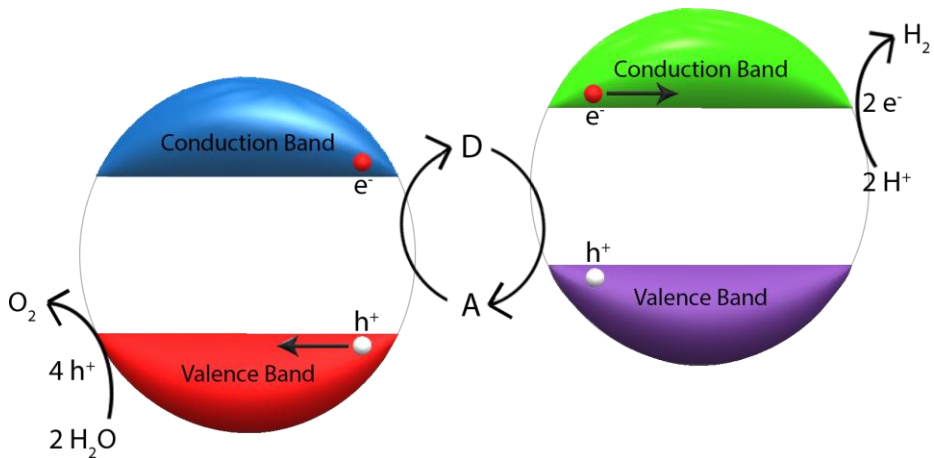


Figure 1.5: Schematic representation of the Z-scheme.

The illustrated combination of metal oxides will not work however. The problem is that most semiconductors are only stable in a certain pH range and in the given example either Cu₂O or Fe₂O₃ is unstable. There are several semiconductor combinations known to be capable of performing complete photocatalytic water splitting, however these systems use catalysts based on expensive materials like Pt and Ru, making them economically unviable.^[15]

The catalytic activity of photocatalyst semiconductor materials is also important. Even when a semiconductor is thermodynamically suited to perform the desired redox reactions does not mean that it is an efficient catalyst. If a semiconductor happens to be catalytically inactive it can be functionalized with catalyst particles. For example Pt nanoparticles are very suitable for the catalysis of the hydrogen evolution reaction. For the oxygen evolution reaction cobalt phosphate Co-Pi is an example of a suitable catalyst material. Figure 1.6 gives a schematic representation of a semiconductor particle functionalized with a co-catalyst.^[5, 6, 9]

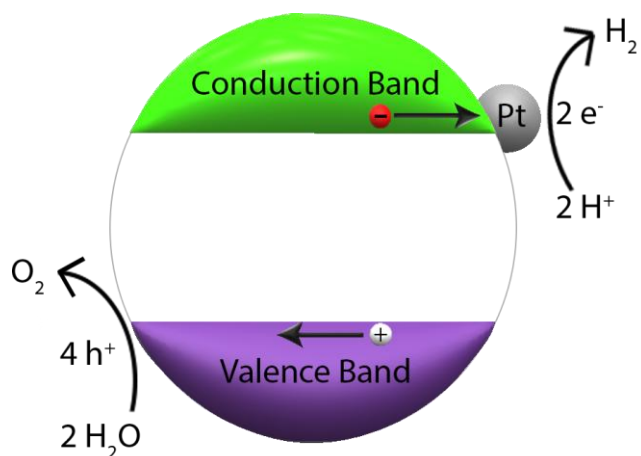


Figure 1.6: Schematic representation of a semiconductor functionalized with a catalyst.

When considering photocatalytic water splitting over semiconductor particles there is a significant practical problem. Hydrogen and oxygen gas will be evolved from a single vessel. When considering larger scale applications separating these gasses becomes a vital part, since this is a highly explosive mixture. Gas separation can be done by using separation membranes. Another solution to this problem is by separating the different redox reactions. This is the case for photoelectrochemical cells, which will be explained in the next section.

1.1.2. Photoelectrochemistry

In a photoelectrochemical setup (PEC) the reduction and oxidation reactions occur at different electrodes. Three different electrode combinations can be considered in this type of devices: 1) a photocathode and an anode, 2) a cathode and photoanode and 3) a photocathode and photoanode, as shown in Figure 1.7. The basic principles governing the previous arrangements are the same, so for the sake of simplicity the representation given in Figure 1.7 will be elaborated. A PEC cell with two photoelectrodes is very similar to the Z-scheme in photocatalysis.^[3, 6, 7] For a photoelectrode, the photoactive material present is normally in the form of a thin homogeneous film or a nanostructured assembly such as nanorods.^[3, 7, 10, 16-19]

In Figure 1.8 an effect called band bending is illustrated. Band bending occurs at interfaces of semiconductors with for example an electrolyte or another semiconductor. At an electrolyte-semiconductor interface band bending depends mostly on the adsorbates, if these are positively charged, such as protons, there is an electric field directing electrons in the semiconductor towards the surface. This is described by the bands bending down at the interface. If the adsorbates are negatively charged electrons would be directed away from the interface resulting in the bands bending upward, this is depicted in Figure 1.8B.^[7, 10, 16]

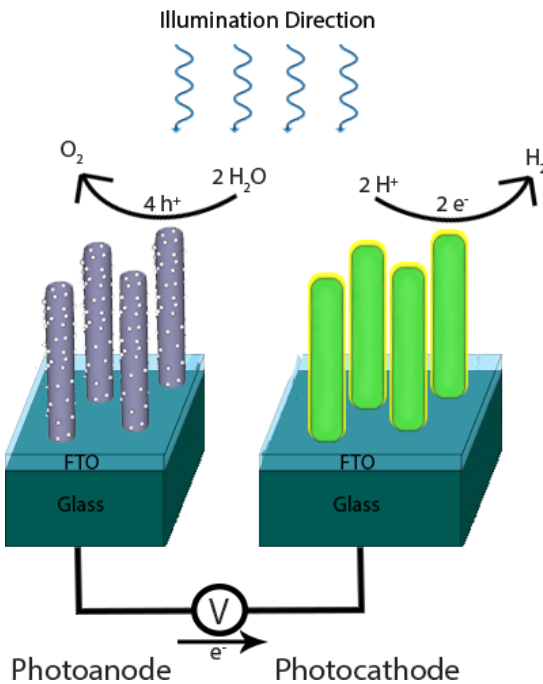


Figure 1.7: Schematic view on a complete PEC cell. On the left the photoanode is shown which performs the water oxidation. Then on the right the photocathode performs the proton reduction. A electrical bias can be applied between the electrodes.

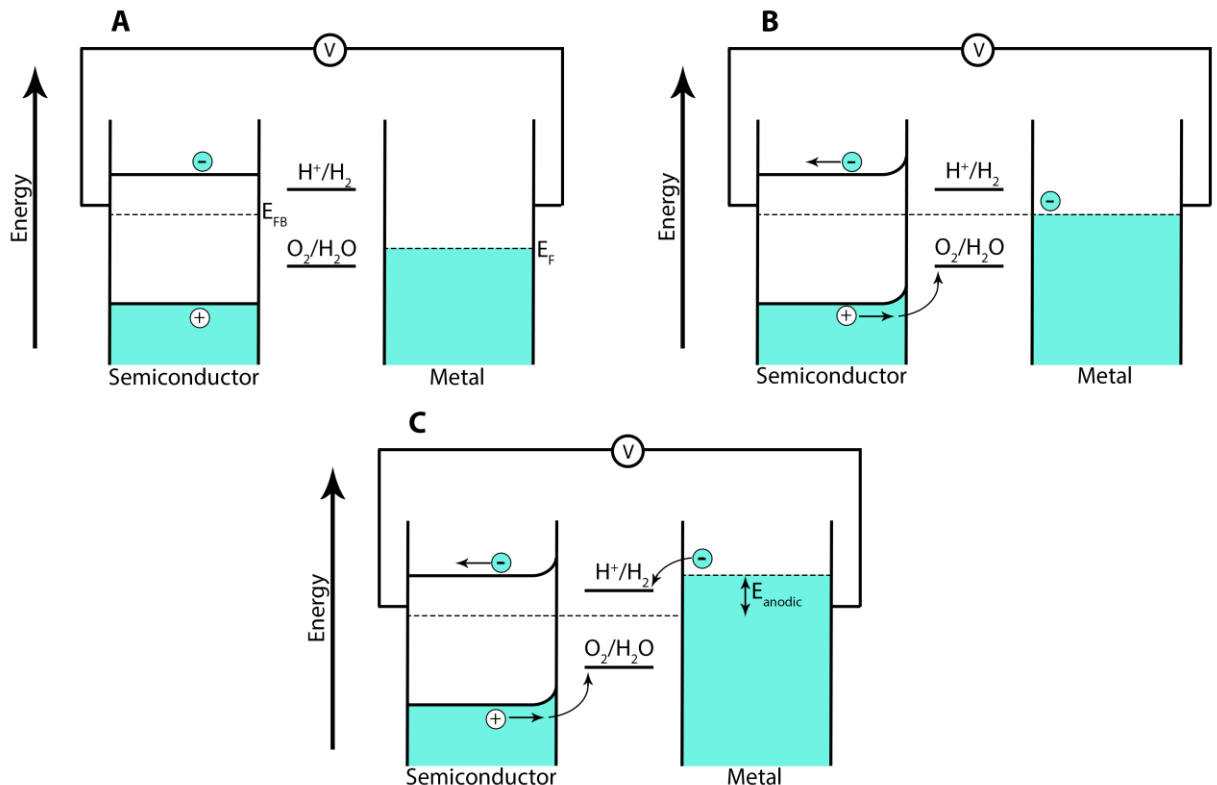


Figure 1.8: Schematic representation of band bending and the effect of applying an electrical bias. A gives the representation without band bending taken into account, B a representation with band bending taking into account and C a representation where an anodic external bias is applied as well.

The oxidation and reduction reactions take place at the anode and cathode, respectively. The difference between a photoelectrode and an electrode is that a photoelectrode absorbs photons to generate potential. An electrode requires an external electrical bias to change the potential. In Figure 1.8C the effect of applying such an electrical bias is represented, in this case an anodic one. As can be seen in the diagram this bias is capable of changing the potential of the bands in the bulk, improving charge separation.^[7, 10, 16]

When designing a photoelectrochemical setup the electrochemical potentials of all materials should be carefully considered. A material added to protect a semiconductor material might trap the electrons. If this protecting layer is not capable of actually reducing protons because the potential is too positive the charge carrier is lost. When all materials are combined optimally the electrons and holes can flow as shown in Figure 1.9. However current known combinations of materials, which are stable under the same conditions all have relatively large bandgaps and do not absorb visible light.^[7, 10, 16, 19]

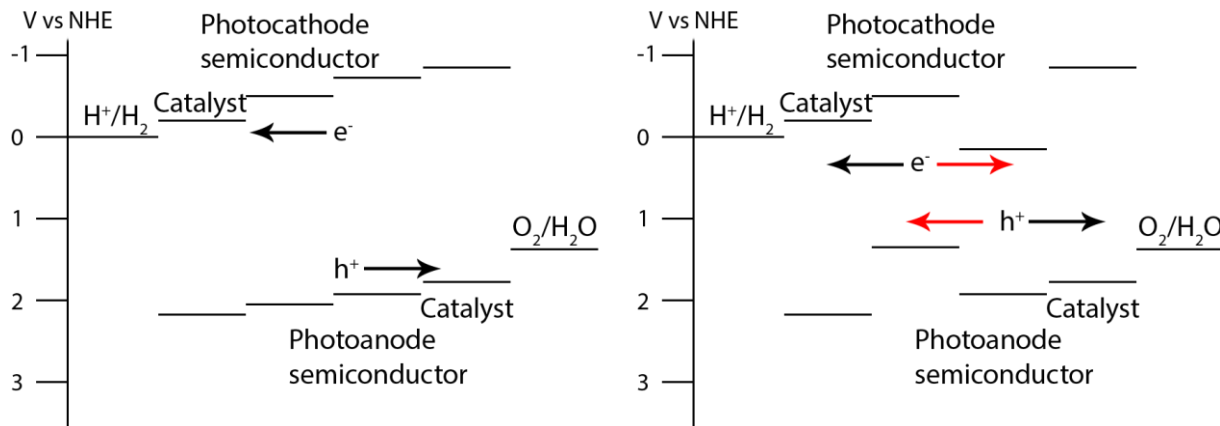


Figure 1.9: Energy diagram of an ideal combination of materials for a water splitting PEC cell. Note that band bending is omitted for clarity.

Figure 1.10: Energy diagram of a more realistic combination of materials for a water splitting PEC cell. Note that band bending is omitted for clarity.

A more realistic diagram can be seen in Figure 1.10. Here the potentials do not match well between the two semiconductors resulting in unfavorable charge carrier movements, indicated by the red arrows. By applying a bias between those two semiconductors one makes sure that the electrons and holes move in the right direction by pushing them over the energy barrier this mismatch presents.^[7]

However, when applying an electrical bias energy is introduced to system from a different source than direct illumination. When discussing renewable energy conversion this is a significant drawback, but in a smart design this external energy source could be a photovoltaic cell making sure the system still runs solely on solar power, of which an example is shown in Figure 1.11.^[20]

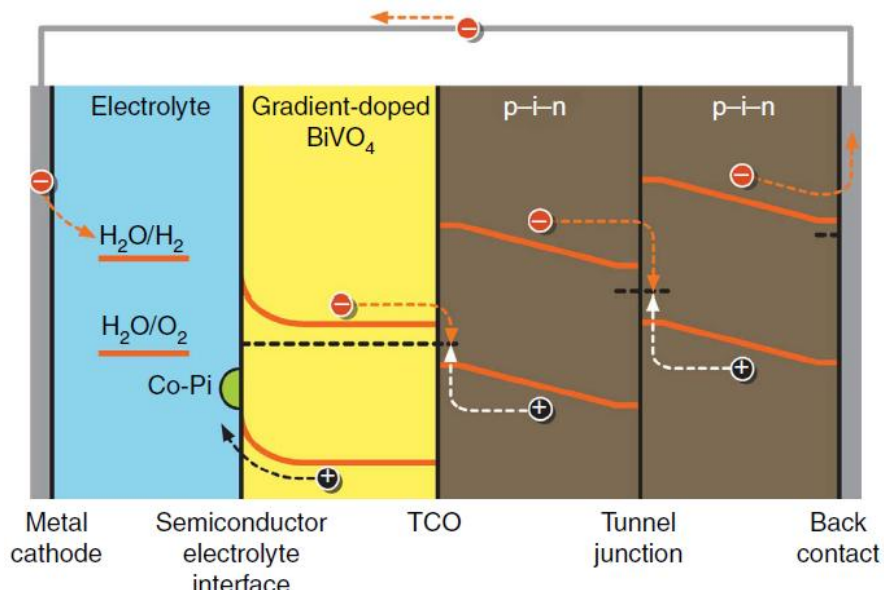


Figure 1.11: Schematic representation of a PV-PEC cell. In the set of p-i-n junctions extra potential is generated to allow the system to perform the complete water splitting reaction.^[20]

As has been shown in the previous two sections both PC and PEC setups have their advantages and disadvantages. To summarize, PC is relatively simple and cheap to produce and maintain. However finding systems which are suitable to perform complete water oxidation and which are sufficiently stable is difficult, but this issue can be tackled by the Z-scheme strategy. A fundamental problem with a PC setup is that a dangerous mixture of hydrogen and oxygen is formed in a single vessel. This can be solved by utilizing the PEC setup. Here the reactions are split spatially and thus the evolved gasses can be collected separately. The PEC is also more versatile when choosing materials because an electrical bias can be applied to overcome a possible mismatch of the bands. This does require extra input of energy which lowers the overall efficiency however, which can be tackled by using photovoltaic cells. Photoelectrochemical and photovoltaic cells are expensive so a high efficiency and stability is necessary.

1.2 Metal-Organic Frameworks

In recent years MOFs are reported as candidates for photocatalytic conversions. MOFs are a class of materials, sometimes also referred to as porous coordination polymers (PCPs), that have received increasing attention over the last years. [21-23] A MOF is a highly porous, often crystalline, material which consists of metal ions and organic linkers.^[24] MOFs are being researched for purification^[25] or storage of gasses^[26, 27], membranes for sensing^[28, 29], catalysis^[30-34] and many more applications.^[24] The metal ions are often d-metals or f-metals and make up the nodes in the framework of MOFs.^[24] The nodes exist in different forms which can for example be just the metal ion^[35-37], a paddlewheel of two ions^[38] (Figure 1.12, right) or an oxometallic cluster^[39, 40] (Figure 1.12, left). These nodes are linked together by

organic moieties. Most MOFs have linkers based on imidazolates or aromatic carboxylates. When an imidazolate is the linker, the resulting material is often referred to as a ZIF (zeolitic imidazolate framework) named this way because it forms crystal structures similar to that of zeolites.^[35-37] MOF structures are very versatile since a plethora of metals and linkers can be combined.

MOFs can be found with many different metal ions, like Cu²⁺^[38, 41-45], Zn²⁺^[35-37], Zr⁴⁺^[39, 46-59], Fe²⁺^[60, 61], Ti⁴⁺^[40, 62-68] and Co²⁺^[43, 69, 70] and others.^[71-76] Depending on the metal ion the structure of the node is different. Zn²⁺ for example forms the node on its own, Zr⁴⁺ is an example that forms oxometallic clusters as nodes, an example, UiO-66-NH₂, is given in Figure 1.12 (left). Cu²⁺ is an example which forms paddlewheel like nodes where two copper ions are together, an example, Cu₂(DABCO)(ATA)₂, is given in Figure 1.12 (right). The structure of the node determines the structure the MOF is likely to have with a family of linkers.^[23, 24, 33, 77-79] When MOFs with similar linkers have the same structure they are called isoreticular.^[24]

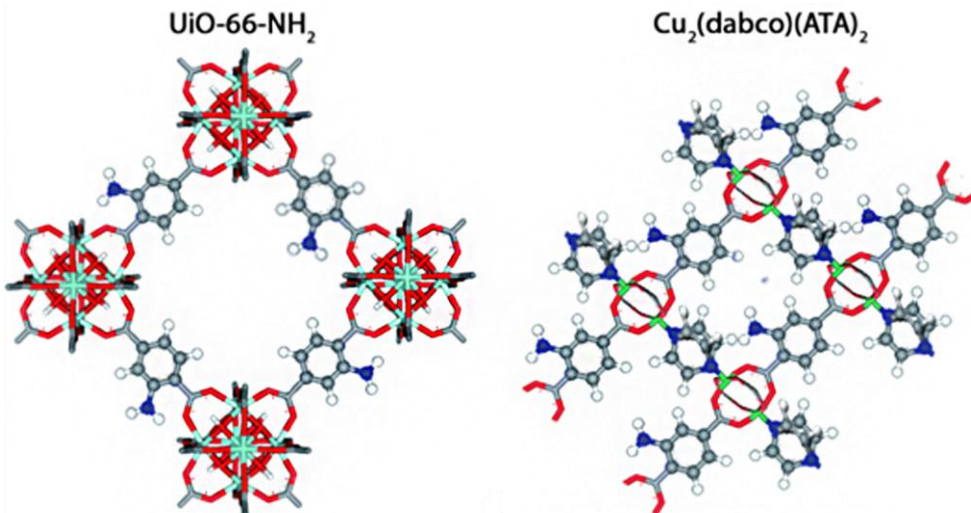


Figure 1.12: Schematic representation of two MOFs. The first is UiO-66-NH₂ which consists of an oxometallic cluster node with Zr and 2-aminoterephthalic acid, the second is Cu₂(DABCO)(ATA)₂ where the node consists of a paddlewheel structure with two Cu²⁺ ions. Grey = C, white = H, blue = N, red = O, cyan = Zr, green = Cu. DABCO = 1,4-Diazabicyclo[2.2.2]octane, ATA = 2-aminoterephthalic acid.

An example of a family of linkers is that of para-aromatic dicarboxylates where, for the same metal node, 1,4-benzenedicarboxylate and 2-amino-1,4-benzenedicarboxylate often result in the same framework. The same type of framework can even be observed with 4,4'-biphenyldicarboxylic acid, although the pores are wider in these MOFs.^[24, 39, 49] An example of a linker which is not part of this family is benzenetricarboxylate. Since this linker is sterically different, it forms a structurally different framework.

Like other catalysts MOFs have active sites, which can be the metal node or a group on the organic linker. In MOFs the activity of homogeneous catalysts can be combined with the ease of recovery and to some extent the stability of heterogeneous

catalysts.^[33, 80, 81] Most MOFs are unstable at high temperatures, making them unsuited for high temperature applications, but are mechanically robust. This makes MOFs, along with other properties a potential candidate for photodriven reactions.

1.2.1. MOFs as Photocatalysts and Photoelectrode materials

In section 1.1.1, the fundamental aspects of semiconductor photocatalysts were discussed. MOF-based photocatalysis is different to that in some respects. Since MOFs do not consist of a set of repeating orbitals which can combine into clear bands their electromagnetic behavior is more comparable to that of molecules. In other words when a photon is absorbed by a MOF its electron is excited from the highest occupied molecular orbital (HOMO, equivalent to the valence band) to the lowest unoccupied molecular orbital (LUMO, equivalent to the conduction band).^[33, 70, 82, 83] The transition following excitation is hypothesized to be a charge transfer where the organic linker injects an electron into the metal node.^[82, 84] This process is shown in Figure 1.13. To move inside the material the electron has to travel a significant distance to reach the next metal node. This is why MOFs are found to have a relatively poor conductivity.^[33, 70, 84] This is further hampered by the fact that carboxylate groups are insulating, meaning the electron can only “hop” to the next metal node.^[70, 84] To improve the conductivity of the MOFs ions like iodine can be added into the pores of the framework. These can act as redox mediators to transport the electron from one node to another. This occurs by the redox mediator being reduced by one node, this reduced mediator can then be oxidized by other nodes.^[45, 85]

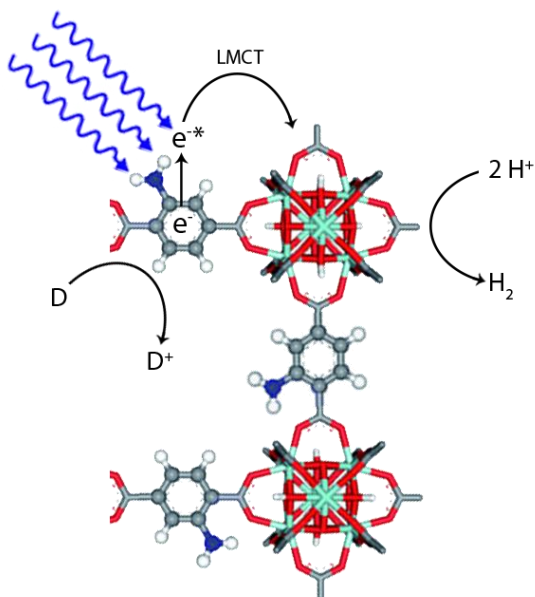


Figure 1.13: Schematic representation for the hypothesized charge carrier dynamics in photocatalytic MOFs. D represents an electron donor replenishing the electron injected into the metal node through a ligand to metal charge transfer (LMCT) where protons are reduced to hydrogen. Reductions such as proton reduction are expected to take place at the metal node, oxidations are expected to take place at the organic linker.

That both the linker and node play a role in the catalysis is supported by several studies. Transitions like for example Ti^{4+} to Ti^{3+} ^[63] and Zr^{4+} to Zr^{3+} ^[56] have been observed with electroparamagnetic resonance spectroscopy (EPR). For the linkers it has been found that different substitutions (amino, hydroxy) on the aromatic ring of for example terephthalic acid influence the bandgap. ^[86-88] Since functional groups like amino groups donate electrons more easily than the hydrogen atoms they replace, it makes sense that it would be easier to excite electrons and transfer it to the metal node.^[88] This explains why 2-aminoterephthalic acid based frameworks absorb lower energy photons (higher wavelengths) than terephthalic acid based frameworks.

After the ligand to metal charge transfer there are an electron and a hole which can perform redox reactions.^[33] There are reports on several reduction reactions with MOFs as photocatalysts. Since the electron is present on the metal node it is reported that the node is the catalytically active component for reduction reactions. Since MOFs have low conductivity performing reduction reactions get increasingly difficult when they require more electrons.^[84] This is of course true for every photocatalytic material but in many the conductivity is better and thus the material is better capable of transporting charges to the reaction site. For MOFs this can be quite difficult. Reports are either on proton reduction, the reduction of CO_2 to CO or HCOO^- or reduction of organic pollutants. All these reactions require the transfer of two charge carriers at most. A reaction like the formation of methanol from CO_2 , involving six electrons, is more challenging from the point of view of kinetics.

The holes remaining on the linker do not oxidize water in most cases, so other materials are added to the electrolyte to scavenge these charge carriers. This is why in photocatalytic studies of these materials sacrificial agents like triethylamine (TEA) or triethanolamine (TEOA) are present. If there is no hole scavenger the material either self-oxidizes and falls apart or the charges recombine.^[84]

MOFs can also be considered to functionalize semiconductors both for photoelectrodes and photocatalytic systems^[21, 89], where they can function as light absorber^[68, 90, 91], catalyst^[92, 93] or to increase (selective) reactant uptake^[35-37, 91, 94]. Functionalizing an electrode with a MOF is not necessarily trivial however since the adhesion of the MOF to the material is an important issue to consider. A good contact is necessary to have sufficient electric interaction and stability.^[37] It is also possible to functionalize the cages in the MOFs with catalysts.^[68, 90]

Research into producing MOF films is a growing field. Functionalization of a substrate with a self-assembled monolayer (SAM), which facilitates the formation and adhesion of the MOF film, is one of the most used methods. ^[95, 96] For electrochemical purposes this strategy is not likely to work however. The organic molecules that have been reported to form this SAM do not conduct electrons and will act as an insulating layer. This is why methods to immobilize MOFs directly on a conductive substrate have been considered, ideally yielding a film as shown in Figure 1.14.^[96] These methods include dropcasting^[65, 68, 85], hydrothermal synthesis^[97-99], layer-by-layer synthesis^[45, 85, 100], electrochemical synthesis^[101-108] and others^[109, 110].

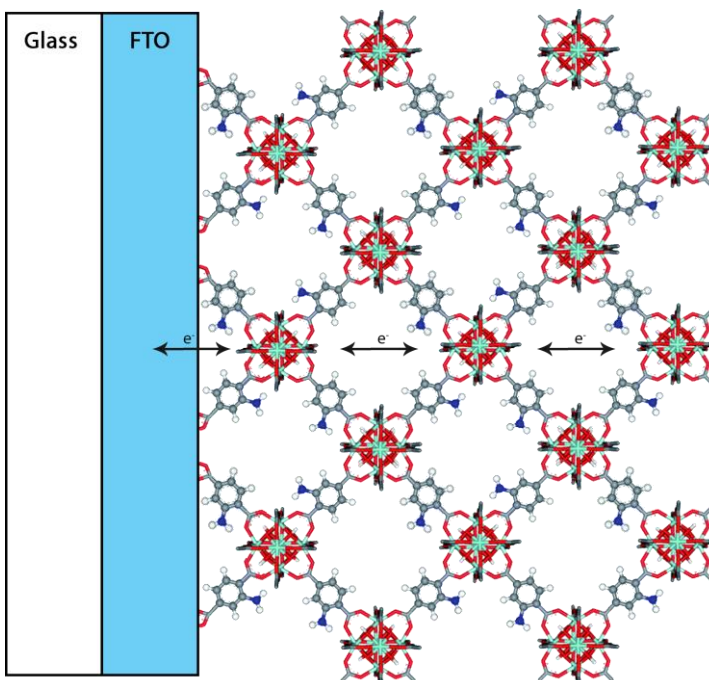


Figure 1.14: Schematic representation of a MOF immobilized on a FTO slide. In the representation the assumption is made that the MOF attaches to the FTO through the organic linker. There is no definite proof that this is indeed the case.

1.2.2. State-of-the-art

In literature, several MOFs have been reported as photocatalysts. The MOF that has been most extensively investigated in this context is the Zr^{4+} based MOF with linkers based on terephthalic acid. This MOF is identified as UiO-66 (after University of Oslo). The effect of functionalizing the linker with amino groups has been explored and it has been observed that both the catalytic activity and the absorption from the visible region of the light spectrum improved. Most reports on this MOF study CO_2 reduction and proton reduction.^[47, 55, 56] Proton reduction over UiO-66 has also been considered when a part of the terephthalic acid linkers have been replaced with a diiron based catalyst and a Ru-complex as a photosensitizer, improving the solar to hydrogen efficiency.^[111]

Similar MOF structures with biphenyl linkers have been considered as well, these are referred to as UiO-67. In these cases some of the linkers were replaced with organometallic complexes, mostly based on Ir or Re. For these systems water oxidation, proton reduction and CO_2 reduction have been studied. In Figure 1.15 an example is presented where Pt was added as a co-catalyst. Higher conversion rates have been reported for these MOFs compared to ones without these organometallic clusters and Pt co-catalysts. A problem with these systems however is the fact that the organometallic complexes are unstable and that the expensive and toxic Ir and Re ions leach into the solvent.^[58, 59, 78, 83] In all the upper cases sacrificial agents have been used to make sure the remaining charge carriers were removed.

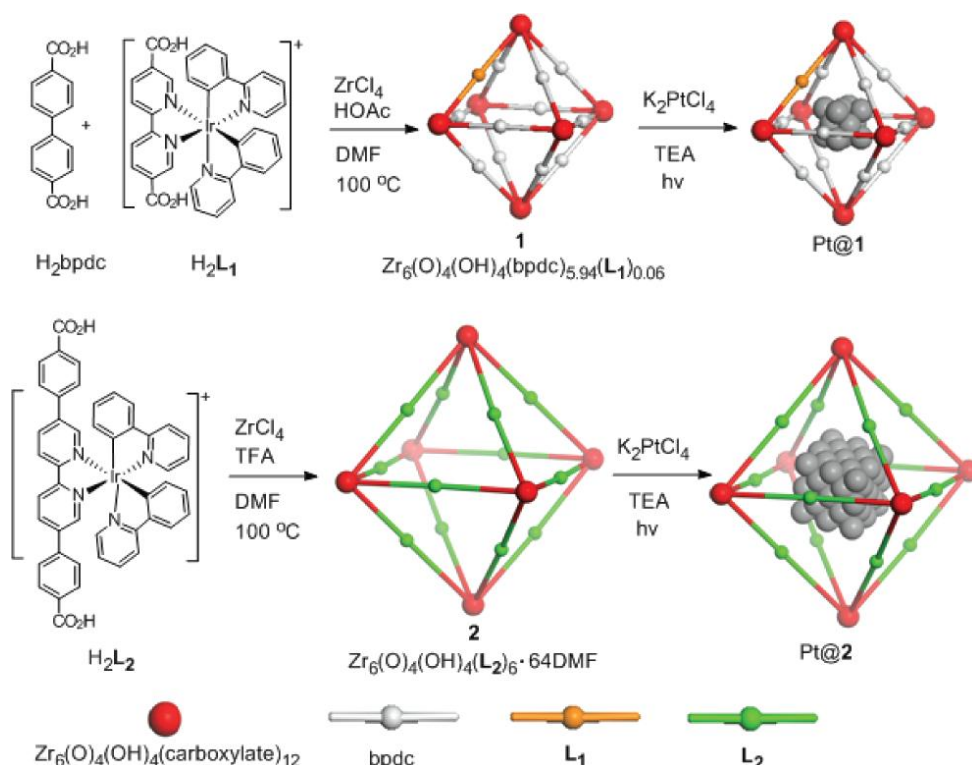


Figure 1.15: Schematic representation of UiO-67 (upper) and the UiO-framework with tetraphenyl linkers (lower) MOFs functionalized with Ir-based complexes as linkers. After synthesis of the frameworks with the complexes Pt nanoparticles are synthesized inside the pores by photoreduction. These MOFs are then used for photocatalysis.^[58]

Another family of MOFs that has been extensively studied for photocatalysis consists of Ti^{4+} with terephthalic acid derivatives known as the MIL-125(Ti) family, (after Materials Institute Lavoisier).^[62–66, 68] The degradation of organic molecules with $\text{NH}_2\text{-MIL-125(Ti)}$ has been studied and they were found to be as active as TiO_2 ^[62, 63]. Others combined this same MOF with Pt nanoparticles and studied the reduction of either protons^[68] or CO_2 ^[66]. Another research group added a cobaloxime complex instead of Pt as a co-catalyst and showed improved activity towards the hydrogen evolution reaction compared to the Ti-MOF without co-catalyst.^[67] Other studies show $(\text{OH})_2\text{-MIL-125(Ti)}$ as a photocatalyst for dye degradation as well as immobilizing this MOF by dropcasting on FTO and studying its photoelectrochemical properties.^[65]

Cu and Co based MOFs have also been studied.^[41–43, 69, 70, 112] For Cu^{2+} MOFs the focus is on the linker benzenetricarboxylate, resulting in the MOF HKUST-1 (after Hongkong University of Science and Technology). These MOFs have been studied for electrochemical reduction of oxygen^[41] and CO_2 ^[42] as well as the photocatalytic oxidation of cyclohexene^[43]. Pyrazole linkers have also been considered for Cu^{2+} MOFs for the degradation of dyes.^[112] Co^{2+} MOFs have been studied with the linker dihydroxyterephthalic acid (DHTA) for the photocatalytic oxidation of cyclohexene^[43] and with imidazole as a linker (ZIF-9(Co)) for the reduction of CO_2 ^[69]. In the latter case a Ru-based complex was present in the solution as a photosensitizer. Finally a Co^{2+} based MOF with porphyrin linkers has been studied for the electrocatalytic reduction of CCl_4 .^[70]

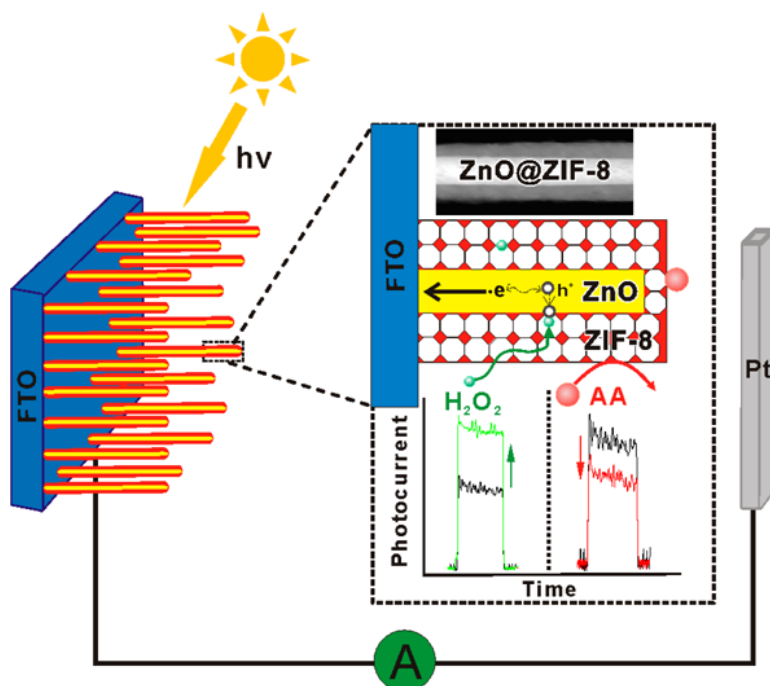


Figure 1.16: Schematic representation of ZnO nanorods on FTO with a ZIF-8 coating. Shown is how it can select H_2O_2 over ascorbic acid to perform the oxidation on ZnO. This image is taken from ref.^[37]

ZIF-8 has also been studied in several photocatalytic and photoelectrochemical systems.^[35-37, 94] ZIF-8 consists of Zn^{2+} and 2-methylimidazole. ZIF-8 is not photocatalytic by itself and it does not absorb light in the visible region. When combined with other materials however it can yield interesting systems. Gao et al.^[35] synthesized Ag/AgCl particles in ZIF-8 and then studied the degradation of organic dyes under visible light excitation. Zhan et al^[37] used FTO glass substrates as a conductive support for ZnO nanorods and then used an electrochemically dissolved part of the Zn. The resulting Zn ions led to the formation of ZIF-8 at the surface of the nanorods. This photoelectrode system was used to selectively oxidize H_2O_2 instead of to ascorbic acid. This is possible because the pores of ZIF-8 are too small for ascorbic acid but can allow smaller molecules like H_2O_2 in, this example is shown in Figure 1.1. Liu et al.^[36] functionalized Zn_2GeO_4 nanorods with ZIF-8 where the ZIF-8 improved the activity towards CO_2 reduction by selectively adsorbing CO_2 from the electrolyte. Wee et al. ^[94] transformed powders and films of ZIF-8 partially into ZnO which they then studied for the degradation of the organic dye methylene blue.

Other MOFs have also been studied for photocatalysis or photoelectrochemistry. These include MOFs based on Fe ^[60, 61, 93] or Cd for dye degradation^[74] and porphyrins with Al nodes and filled with Zn for proton reduction using Pt co-catalysts^[75] or filled with Cu for CO_2 reduction^[113]. A large number of studies have focused on selective CO_2 capture from gasses or aqueous media in MOFs as well. ^[80, 81, 113-116] Although these have not been directly considered for CO_2 reduction purposes, it is an interesting aspect of MOFs that can be used to functionalize semiconductors. For example -NH₂ groups are shown to be able to capture CO_2 by forming carbamates which is useful for the MOFs with 2-aminothephthalic acid linkers.^[76, 117]

A typical value for hydrogen evolution reported for MOFs without co-catalysts is 837 $\mu\text{mol g}_{\text{cat}}^{-1} \text{ h}^{-1}$, which is for UiO-66-NH₂ systems.^[55] However this activity was not found for MIL-125-NH₂, for which an activity of just 17.5 $\mu\text{mol g}_{\text{cat}}^{-1} \text{ h}^{-1}$ was obtained. However functionalizing this MOF with a cobaloxime complex increased its activity to 350 $\mu\text{mol g}_{\text{cat}}^{-1} \text{ h}^{-1}$.^[67] Such activity is still lower than TiO₂, which produces 10000 $\mu\text{mol g}_{\text{cat}}^{-1} \text{ h}^{-1}$ of hydrogen under UV illumination. However, the MOFs maintain their production under visible light irradiation, while for TiO₂ the production goes down a hundredfold.^[5]

State-of-the-art MOFs nowadays are either used as photocatalysts or porous layers on photoelectrodes. However, studies on MOFs being used as photoelectrodes are few.^[65, 68] For this reason one of the focuses of this study is on MOF photocathodes for the evolution of hydrogen. Various MOFs will be studied to observe potential influences of changing the metal node or linker.

2. Methodology

2.1: Syntheses

The syntheses that have been done in this research will be described in this section. The samples can be divided in two clear groups. First the MOF films or particles immobilized on substrates will be described in Section 2.1.1. The second group consists of MOF particles that have been synthesized as a powder for photocatalysis, which are described in Section 2.1.2. In these sections all weights mentioned have been determined by either a Sartorius CPA225D analytical balance or a Mettler AE163 analytical balance, to keep the determined amounts of material more comparable each has been rounded down to three decimals. Chemicals used in this work are listed in Table A1 in the Appendix.

2.1.1: Films on substrates

In all cases the substrate used is F:SnO₂ (FTO) on glass. FTO is a transparent and conductive metal oxide used often for photoelectrodes. Before the syntheses FTO slides were rigorously cleaned. First the substrates were cleaned with detergent. Then they were immersed in a mixture of demiwasser (DQ), ethanol (EtOH) and acetone and sonicated for about 15 minutes. Following this the substrates were flushed with DQ and immersed in a 1 M HCl solution and sonicated again for about 15 minutes. Again the substrates were flushed with DQ and then dried with pressurized air. Finally they were put under an UV-lamp for 15 minutes before use. Once cleaned the substrates were handled with nitrile gloves to prevent contaminating the samples. Several different routes have been explored to immobilize MOFs on FTO and they will all be discussed in this section.

2.1.1.1: Solvothermal synthesis on pretreated FTO

In the solvothermal synthesis route FTO slides are (partially) immersed into a solution containing both precursors of the MOF. This solution is then heated in an oven or oil bath for 24 hours, and after cooling the slides are removed and flushed with ethanol and methanol.

For the first set of samples the FTO had been pretreated with proto-MOFs to form an initial layer of MOF nuclei from which the layer could grow. These proto-MOFs were formed by preparing a solution containing both precursors and storing them in the dark for some time (24h or 72h). The details of each proto-MOF synthesis are presented in Table 2.1.

Once these proto-MOF solutions had aged they were used to pretreat the FTO slides used in several solvothermal syntheses. To form a tiny layer of proto-MOFs 40 µL of the dispersion was spincoated on the FTO slides. The Electronic Microsystems Ltd Model 4000 spincoater was spun with 1500 rpm for 15 seconds per slide. The slides

Table 2.1: Details of the preparation of proto-MOF solutions.

No.	Metal precursor (g)	Linker (g)	Pillar (g)	Solvent (mL)	Formation time (h)
1	0.210 ZrCl ₄	0.167 ATA	-	5 (DMF:HCl, 14:1)	72
2	0.215 ZrCl ₄	0.166 ATA	-	5 (DMF:DQ, 14:1)	72
3	0.047 ZrCl ₄	0.034 ATA	-	5 (DMF:HCl, 14:1)	72
4	0.048 ZrCl ₄	0.034 ATA	-	5 (DMF:DQ, 14:1)	72
5	0.211 ZrCl ₄	0.165 ATA	-	5 (EtOH:DQ, 1:1)	72
6	0.049 ZrCl ₄	0.033 ATA	-	5 (EtOH:DQ, 1:1)	72
7	0.051 ZrCl ₄	0.035 ATA	-	5 (EtOH:DQ, 1:1)	24
8	0.023 CuCl ₂	0.032 ATA	0.020 DABCO	5 (DMF:HCl, 14:1)	24
9	0.024 CuCl ₂	0.033 ATA	0.021 DABCO	5 (DMF:DQ, 14:1)	24

Table 2.2: Parameters of several solvothermal syntheses on FTO. The number given in the name corresponds to the number of the proto-MOFs presented in Table 2.1.

Name	Metal precursor (g)	Linker (g)	Pillar (g)	Solvent (mL)	Heating
1 a	0.170 ZrCl ₄	0.133 ATA	-	15 (DMF:HCl, 14:1)	393K in oven
1 b	0.034 ZrCl ₄	0.027 ATA	-	15 (DMF:HCl, 14:1)	393K in oven
1 c	0.169 ZrCl ₄	0.134 ATA	-	15 (DMF:DQ, 14:1)	393K in oven
1 d	0.034 ZrCl ₄	0.027 ATA	-	15 (DMF:DQ, 14:1)	393K in oven
1 ^a e	0.169 ZrCl ₄	0.132 ATA	-	15 (EtOH:DQ, 1:1)	393K in oven
1 ^a f	0.034 ZrCl ₄	0.026 ATA	-	15 (EtOH:DQ, 1:1)	393K in oven
2 a	0.170 ZrCl ₄	0.133 ATA	-	15 (DMF:HCl, 14:1)	393K in oven
2 b	0.034 ZrCl ₄	0.027 ATA	-	15 (DMF:HCl, 14:1)	393K in oven
2 c	0.169 ZrCl ₄	0.134 ATA	-	15 (DMF:DQ, 14:1)	393K in oven
2 d	0.034 ZrCl ₄	0.027 ATA	-	15 (DMF:DQ, 14:1)	393K in oven
2 ^a e	0.169 ZrCl ₄	0.132 ATA	-	15 (EtOH:DQ, 1:1)	393K in oven
2 ^a f	0.034 ZrCl ₄	0.026 ATA	-	15 (EtOH:DQ, 1:1)	393K in oven
3 a	0.170 ZrCl ₄	0.133 ATA	-	15 (DMF:HCl, 14:1)	393K in oven
3 b	0.034 ZrCl ₄	0.027 ATA	-	15 (DMF:HCl, 14:1)	393K in oven
3 c	0.169 ZrCl ₄	0.134 ATA	-	15 (DMF:DQ, 14:1)	393K in oven
3 d	0.034 ZrCl ₄	0.027 ATA	-	15 (DMF:DQ, 14:1)	393K in oven
3 ^a e	0.169 ZrCl ₄	0.132 ATA	-	15 (EtOH:DQ, 1:1)	393K in oven
3 ^a f	0.034 ZrCl ₄	0.026 ATA	-	15 (EtOH:DQ, 1:1)	393K in oven

Name		Metal precursor (g)	Linker (g)	Pillar (g)	Solvent (mL)	Heating
3	g	0.087 ZrCl ₄	0.067 ATA	-	10 (DMF:HCl, 14:1)	383K in oil bath
3	h	0.017 ZrCl ₄	0.013 ATA	-	10 (DMF:HCl, 14:1)	383K in oil bath
3	i	0.086 ZrCl ₄	0.066 ATA	-	10 (EtOH:DQ, 1:1)	363K in oil bath
3	j	0.017 ZrCl ₄	0.013 ATA	-	10 (EtOH:DQ, 1:1)	363K in oil bath
4	a	0.170 ZrCl ₄	0.133 ATA	-	15 (DMF:HCl, 14:1)	393K in oven
4	b	0.034 ZrCl ₄	0.027 ATA	-	15 (DMF:HCl, 14:1)	393K in oven
4	c	0.169 ZrCl ₄	0.134 ATA	-	15 (DMF:DQ, 14:1)	393K in oven
4	d	0.034 ZrCl ₄	0.027 ATA	-	15 (DMF:DQ, 14:1)	393K in oven
4 ^a	e	0.169 ZrCl ₄	0.132 ATA	-	15 (EtOH:DQ, 1:1)	393K in oven
4 ^a	f	0.034 ZrCl ₄	0.026 ATA	-	15 (EtOH:DQ, 1:1)	393K in oven
4	g	0.087 ZrCl ₄	0.067 ATA	-	10 (DMF:HCl, 14:1)	383K in oil bath
4	i	0.086 ZrCl ₄	0.066 ATA	-	10 (EtOH:DQ, 1:1)	363K in oil bath
4	j	0.017 ZrCl ₄	0.013 ATA	-	10 (EtOH:DQ, 1:1)	363K in oil bath
5	c	0.169 ZrCl ₄	0.134 ATA	-	15 (DMF:DQ, 14:1)	393K in oven
6	a	0.170 ZrCl ₄	0.133 ATA	-	15 (DMF:HCl, 14:1)	393K in oven
6	b	0.034 ZrCl ₄	0.027 ATA	-	15 (DMF:HCl, 14:1)	393K in oven
6	c	0.169 ZrCl ₄	0.134 ATA	-	15 (DMF:DQ, 14:1)	393K in oven
6	d	0.034 ZrCl ₄	0.027 ATA	-	15 (DMF:DQ, 14:1)	393K in oven
6 ^a	e	0.169 ZrCl ₄	0.132 ATA	-	15 (EtOH:DQ, 1:1)	393K in oven
6 ^a	f	0.034 ZrCl ₄	0.026 ATA	-	15 (EtOH:DQ, 1:1)	393K in oven
7	g	0.087 ZrCl ₄	0.067 ATA	-	10 (DMF:HCl, 14:1)	383K in oil bath
7	h	0.017 ZrCl ₄	0.013 ATA	-	10 (DMF:HCl, 14:1)	383K in oil bath
8	a	0.045 CuCl ₂	0.065 ATA	0.040 DABCO	10 (DMF:HCl, 14:1)	383K in oil

Name	Metal precursor (g)	Linker (g)	Pillar (g)	Solvent (mL)	Heating
8 b	0.045 CuCl ₂	0.065 ATA	0.040 DABCO	10 (DMF:HCl, 14:1)	bath 383K in oil bath
8 c	0.009 CuCl ₂	0.013 ATA	0.008 DABCO	10 (DMF:HCl, 14:1)	383K in oil bath
9 a	0.045 CuCl ₂	0.065 ATA	0.040 DABCO	10 (DMF:HCl, 14:1)	383K in oil bath
9 b	0.045 CuCl ₂	0.065 ATA	0.040 DABCO	10 (DMF:HCl, 14:1)	383K in oil bath
9 c	0.009 CuCl ₂	0.013 ATA	0.008 DABCO	10 (DMF:HCl, 14:1)	383K in oil bath

^a These samples failed because the solvent evaporated due to too high temperatures. In text these samples will be referred to with the prefix “Sur-” and as M(linker)/promotor to directly clarify which MOF is being addressed.

were then subjected to the solvothermal route described above. In Table 2.2 the details of each synthesis are given. The number corresponds to the proto-MOF that was coated on the sample. The letter corresponds to the solvothermal synthesis that was used.

Other routes utilizing the solvothermal synthesis have also been attempted. Films of the UiO-66(NH₂) MOF have been attempted to be made by pretreating the FTO with a NaOH solution and optionally with a solution of just ATA as well. This set is referred to as Sur-10, where a refers to untreated FTO, b to FTO treated with a NaOH solution and c to FTO treated with a NaOH solution and a solution of ATA. In short cleaned FTO slides (3.0 x 1.2 cm²) where immersed in a solution of NaOH (pH of about 10) for 20 minutes. Then they were rinsed and treated with UV. Afterwards a few of these slides were immersed in a ATA solution (0.00181 g/100 mL DMF) overnight. Then they were immersed in solutions of ZrCl₄ and ATA (8.535 g/L and 6.628 g/L resp. in 14:1 DMF:HCl). They were fixed vertically in sample flasks. These were heated to 383K in an oil bath overnight.

2.1.1.2: Solvothermal synthesis on untreated FTO

Samples have also been prepared without pretreating the FTO, apart from cleaning it. For these samples FTO slides (3.0 x 1.2 cm²) were partially immersed in a solution of the precursors. Then the samples were heated in an oil bath to 383K for a defined time. After this they were rinsed with ethanol and methanol and the backside of each

sample was cleaned by using a cotton swab wetted with ethanol. In Table 2.3 the details of each synthesis using this route are given.

Table 2.3: Parameters of several solvothermal syntheses on FTO.

Name	Metal precursor (g)	Linker (g)	Pillar (g)	Solvent (mL)	Time (h)
13^a	0.191 Ti(O-Bu) ₄	0.110 DHTA	-	15 (DMF:HCl, 14:1)	24
16^b a	0.853 ZrCl ₄	0.668 ATA	-	100 (DMF:HCl, 14:1)	2
16^b b	0.853 ZrCl ₄	0.668 ATA	-	100 (DMF:HCl, 14:1)	16
16^b c	0.853 ZrCl ₄	0.668 ATA	-	100 (DMF:HCl, 14:1)	24
17^c	0.070 CuCl ₂	0.100 ATA	0.064 DABCO	15 (DMF:DQ, 14:1)	24
18^c	0.127 CoCl ₂ · 6 H ₂ O	0.100 ATA	-	15 (DMF:DQ, 14:1)	24
19^c	0.189 Ti(O-Bu) ₄	0.112 DHTA	-	15 (DMF:DQ, 14:1)	24
20	0.067 ZrCl ₄	0.051 ATA	-	7.5 (DMF:HCl, 14:1)	24
21^d	0.095 Ti(O-Bu) ₄	0.054 DHTA	-	7.5 (DMF:DQ, 14:1)	24

^a This synthesis was performed on two FTO slides, they were clamped together in the same reaction vessel, the clamp however dissolved partially during the synthesis. ^b These syntheses were performed in triplicate in separate flasks. ^c These syntheses were performed in duplicate in separate flasks. ^d The DHTA was dissolved in the solvent before adding the Ti(O-Bu)₄ precursor. In the text the samples will be referred to with the prefix "Sur-" and as M(linker)/promotor to directly clarify which MOF is being addressed.

2.1.1.3: Dropcasting synthesis on FTO

A completely different route that has been explored is dropcasting. Here a presynthesized batch of the desired MOF is dispersed in a solvent by stirring it for 24 hours while heating. A small amount of this dispersion is dropped on a FTO slide, and spread over the FTO. A part of the FTO is masked with tape during this. Then the slides were dried on a hot plate of 333K for 60 seconds. Then the slides were cooled down for 60 seconds before adding the dispersion again. Several cycles were performed on each sample. After the immobilization the films were rinsed with ethanol and methanol. The adhesion of the films was tested by tapping the slides to a table, by blowing over pressurized air and by scratching with a cotton swab. They were stable to the tapping and air current but were easily removed with the cotton swab. Table 2.4 gives the details of each dropcasting experiment performed in this research.

Table 2.4: Parameters of dropcasting experiments.

Name		MOF	Dispersion solvent and temperature	Size of drop per cycle (μL)	Cycles
11	a	UiO-66(NH ₂), Residue of Sur-1a, 0.010 g	1 mL Ethanol, 338K	36	2
11	b	UiO-66(NH ₂), Residue of Sur-1a, 0.010 g	1 mL Ethanol, 338K	36	4
11	c	UiO-66(NH ₂), Residue of Sur-1a, 0.010 g	1 mL Ethanol, 338K	36	6
11	d	UiO-66(NH ₂), Residue of Sur-1a, 0.010 g	1 mL Ethanol, 338K	36	7
12	a	UiO-66(NH ₂), Residue of Sur-1a, 0.99 mg	10 mL Ethanol, 348K	30	4
12	b	UiO-66(NH ₂), Residue of Sur-1a, 1.04 mg	9 mL Ethanol, 1 mL polyethylene glycol, 348K	30	4
12	c	UiO-66(NH ₂), Residue of Sur-1a, 10.10 mg	10 mL Ethanol, 348K	30	4
12	d	UiO-66(NH ₂), Residue of Sur-1a, 10.42 mg	9 mL Ethanol, 1 mL polyethylene glycol, 348K	30	4
12	e	UiO-66(NH ₂), Residue of Sur-1a, 25.10 mg	10 mL Ethanol, 348K	30	4
12	f	UiO-66(NH ₂), Residue of Sur-1a, 25.08 mg	9 mL Ethanol, 1 mL polyethylene glycol, 348K	30	4
12 ^a	g	UiO-66(NH ₂), Residue of Sur-1a, 0.99 mg	10 mL Ethanol, 348K	30	4

Name	MOF	Dispersion solvent and temperature	Size of drop per cycle (μL)	Cycles
12 ^a	h UiO-66(NH ₂), Residue of Sur-1a, 1.04 mg	9 mL Ethanol, 1 mL polyethylene glycol, 348K	30	4
12 ^a	i UiO-66(NH ₂), Residue of Sur-1a, 10.10 mg	10 mL Ethanol, 348K	30	4
12 ^a	j UiO-66(NH ₂), Residue of Sur-1a, 10.42 mg	9 mL Ethanol, 1 mL polyethylene glycol, 348K	30	4
15 ^b	a UiO-66(NH ₂), Bat-5, 4.95 mg	5 mL DQ	-	5
15 ^{bc}	b UiO-66(NH ₂), Bat-5, 4.95 mg	5 mL DQ	-	5
15 ^{bd}	c UiO-66(NH ₂), Bat-5, 4.95 mg	5 mL DQ	-	5

^a In these experiments the samples were dried at 393K for 60 seconds, instead of 333K. ^b These samples were dipped into the dispersion of the MOF because the surface tension of water did not allow drops to spread over the entire surface. ^c The FTO substrates used in these experiments were pretreated by spincoating 40 μL of a 5 mM Ti sol for 15 seconds and then heating them to 733K for 1 hour and finally cooling it down for 15 minutes.

^d The FTO used in these experiments was pretreated by spincoating 40 μL of a 50 mM Ti sol for 15 seconds and then heated to 733K for 1 hour and finally cooled in air for 15 minutes. In the text the samples will be referred to with the prefix "Sur-" and as M(linker)/promotor to directly clarify which MOF is being addressed.

2.1.1.4: Other synthesis routes

The last types of attempted syntheses included a layer-by-layer type of solvothermal synthesis and electrodeposition. The layer-by-layer synthesis (referred to as Sur-14) had failed because of several reasons. First of all the clamps dissolved as with Sur-13a. Secondly the flasks were not suitable to decently transfer the slides from one solution to another and lastly the different solutions were cross-contaminated despite the washing step that was included. These experiments were performed as following. 1.166 g ZrCl₄ was dissolved in 50 mL DMF:DQ (14:1) and distributed over 3 flasks. 0.907 g ATA was dissolved in 50 mL DMF:DQ and distributed over another 3 flasks. Finally a mixture of DMF:DQ (14:1) was distributed over 3 more flasks as a washing liquid. 3 sets of 3.0 x 1.2 cm² FTO slides were prepared, where two were pretreated with a Ti sol as explained for Sur-15b & c. The slides were then sequentially submerged in the ATA solution (30 minutes at 323K in an oil bath), the washing liquid (shaken), the ZrCl₄ solution (30 minutes 323K in an oil bath) and again in the washing liquid. After two cycles it was all liquids became contaminated and the synthesis route was abandoned.

Electrodeposition was abandoned as a route because no suitable electrical bias could be found for the deposition of UiO-66(NH₂). Electrodeposition was attempted with FTO as a working electrode, Pt as the counterelectrode and a non-aqueous Ag/AgCl reference electrode (preparation of this reference electrode can be found in Section 2.2). A solution of NaNO₃, tetrabutylammoniumbromide (TBAB), ZrCl₄ and ATA in DMF and the separate components with TBAB were tested with cyclic voltammetry. NaNO₃ was added to supply nitrate ions, which are suggested to play a vital role in electrodeposition for MOFs, TBAB was added as a supporting electrolyte to improve the conductivity of the solutions used. However no reduction or oxidation could be seen, suggesting there was no redox chemistry happening which could result in a film. Later tests with XRD and IR also pointed out there had been no deposition. These results will not be shown any further.

2.1.2: Powder samples

Each powder sample has been synthesized through the solvothermal route. Equimolar amounts of metal precursor and linker have been dissolved in dimethylformamide (DMF):Promotor (14:1 volume ratio for DQ and HCl as a promotor, 12:3 for MeOH as a promotor) through sonication. These samples were then heated in an oven or oil bath for 24 hours and cooled down for some time. After cooling down the dispersions were filtrated and washed four times with circa 15 mL solvent each time. The remaining residues were then dried in air overnight and collected. The samples washed with DMF & methanol, once collected, were dispersed in methanol for 24 hours, this step is repeated three times. After this the samples were dried in an oven at 373 K for 24 hours. The samples are listed in Table 2.5.

Table 2.5: Synthesis parameters of the different powder samples.

Name	MOF	Linker (g)	Metal precursor (g)	Pillar (g)	Solvent (mL)	Heating	Washing method
Bat-4	UiO-66(NH ₂)/HCl	0.099 ATA	0.127 ZrCl ₄	-	15	393K in oven	2x DMF, 2x MeOH
Bat-5	UiO-66(NH ₂)/DQ	0.101 ATA	0.124 ZrCl ₄	-	15	393K in oven	2x DMF, 2x MeOH
Bat-6^a	Cu(ATA)/HCl	0.110 ATA	0.072 CuCl ₂	-	15	393K in oven	-
Bat-7^a	Cu(ATA)/DQ	0.100 ATA	0.072 CuCl ₂	-	15	393K in oven	-
Bat-8	UiO-66((OH) ₂)/HCl	0.221 DHTA	0.249 ZrCl ₄	-	30	393K in oven	2x DMF, 2x MeOH
Bat-9	UiO-66((OH) ₂)/DQ	0.223 DHTA	0.252 ZrCl ₄	-	30	393K in oven	2x DMF, 2x MeOH
Bat-10^a	Cu(DABCO)(ATA)/HCl	0.201 ATA	0.145 CuCl ₂	0.127 DABCO	30	393K in oven	2x DMF, 2x MeOH
Bat-11	Cu(DABCO)(ATA)/DQ	0.199 ATA	0.147 CuCl ₂	0.125 DABCO	30	393K in oven	2x DMF, 2x MeOH
Bat-12^a	Cu(DABCO)(DHTA)/HCl	0.220 DHTA	0.148 CuCl ₂	0.128 DABCO	30	393K in oven	2x DMF, 2x MeOH
Bat-13^a	Cu(DABCO)(DHTA)/DQ	0.223 DHTA	0.145 CuCl ₂	0.124 DABCO	30	393K in oven	2x DMF, 2x MeOH
Bat-14	UiO-66(NH ₂ /(OH) ₂)/HCl	0.104 ATA, 0.111 DHTA	0.254 ZrCl ₄	-	30	393K in oven	2x DMF, 2x MeOH
Bat-15	UiO-66(NH ₂ /(OH) ₂)/DQ	0.105 ATA, 0.115 DHTA	0.250 ZrCl ₄	-	30	393K in oven	2x DMF, 2x MeOH
Bat-16	Cu(DABCO)(ATA)/DQ	0.102 ATA	0.071 CuCl ₂	0.064 DABCO	15	393K in oven	2x EtOH, 2x MeOH
Bat-17	Co(ATA)/DQ	0.101 ATA	0.127 CoCl ₂ ·6H ₂ O	-	15	393K in oven	2x EtOH, 2x MeOH
Bat-18	Co(DABCO)(ATA)/DQ	0.100 ATA	0.126 CoCl ₂ ·6H ₂ O	0.063 DABCO	15	393K in oven	2x EtOH, 2x MeOH

Name	MOF	Linker (g)	Metal precursor (g)	Pillar (g)	Solvent (mL)	Heating	Washing method
Bat-19	MIL-125(Ti)(NH ₂)/DQ	0.100 ATA	0.186 Ti(O-Bu) ₄	-	15	393K in oven	2x EtOH, 2x MeOH
Bat-20	MIL-125(Ti)(NH ₂)/HCl	0.100 ATA	0.187 Ti(O-Bu) ₄	-	15	393K in oven	2x EtOH, 2x MeOH
Bat-21	MIL-125(Ti)((OH) ₂)/DQ	0.110 ATA	0.192 Ti(O-Bu) ₄	-	15	393K in oven	2x EtOH, 2x MeOH
Bat-22	MIL-125(Ti)((OH) ₂)/HCl	0.112 DHTA	0.189 Ti(O-Bu) ₄	-	15	393K in oven	2x EtOH, 2x MeOH
Bat-23^b	MIL-125(Ti)((OH) ₂)	0.151 DHTA	0.2 mL Ti(O-Bu) ₄	-	3	383K in oil bath	2x EtOH, 2x MeOH
Bat-24	UiO-66(NH ₂)/HCl	0.100 ATA	0.128 ZrCl ₄	-	15	383K in oil bath	2x EtOH, 2x MeOH
Bat-25^c	MIL-125(Ti)((OH) ₂)/DQ	0.113 DHTA	0.185 Ti(O-Bu) ₄	-	15	383K in oil bath	2x EtOH, 2x MeOH
Bat-26^c	MIL-125(Ti)(NH ₂)/MeOH	0.100 ATA	0.189 Ti(O-Bu) ₄	-	15	383K in oil bath	2x EtOH, 2x MeOH
Bat-27^{cd}	MIL-125(Ti)(NH ₂)/MeOH	0.101 ATA	0.190 Ti(O-Bu) ₄	-	15	383K in oil bath	2x EtOH, 2x MeOH
Bat-28^c	MIL-125(Ti)((OH) ₂)/MeOH	0.111 DHTA	0.188 Ti(O-Bu) ₄	-	15	383K in oil bath	2x EtOH, 2x MeOH
Bat-29^{cd}	MIL-125(Ti)((OH) ₂)/MeOH	0.111 DHTA	0.188 Ti(O-Bu) ₄	-	15	383K in oil bath	2x EtOH, 2x MeOH

^a These syntheses yielded no solid product. ^b This synthesis was performed in a different manner, first DHTA was weighed then 3 mL of acetic acid was added to dissolve, then Ti(O-Bu)₄ was added. ^c This synthesis was performed in a slightly different manner, first the linker was dissolved in the solvent before Ti(O-Bu)₄ was added. ^d These samples were heated for 72 hours and the filtrate was collected, dried in air and the samples were kept as Bat-#-F without any further washing steps. In the text the MOFs will be referred to with the given name and as M(linker)/promotor to directly clarify which MOF is being addressed.

2.2: Characterization and measurements

In this section the techniques used in this work will be discussed in terms of settings. First X-ray diffraction (XRD) will be discussed in Section 2.2.1. Next infrared spectroscopy (IR) in Section 2.2.2 and thermogravimetric analysis (TGA) in Section 2.2.3. Then scanning electron microscopy (SEM) in Section 2.2.4 and UV-visible spectroscopy in Section 2.2.5. Photoelectrochemistry (PEC, Section 2.2.6) and photocatalysis with online H₂ detection by gas chromatography (GC, Section 2.2.7) will be discussed afterwards. The last technique that will be experimentally explained is transient absorption spectroscopy (TAS) in Section 2.2.8.

2.2.1: X-ray diffraction

XRD measurements were performed on a Bruker D2 Phaser using Co K $\alpha_{1,2}$ radiation ($\lambda = 190.26$ pm). Powder samples were ground and the fine powder was then prepared in a sample holder making sure the surface was as flat as possible to get a good diffraction signal. The measurements that were performed had a range of 5-35° 2θ or 5-50° 2θ. At all times points had increments of 0.016° 2θ. The integration time per point was 0.2 seconds in general. The sample holder was rotated at 15 rotations per minute. In the event other settings were used than the ones mentioned here this will be indicated in the results section.

For the immobilized samples a custom made sample holder was used. This was designed to make sure the height of the samples was correct with the beam. This is because diffraction peaks shift if the height of the sample is incorrect. These samples were measured with the following settings: 5-35° 2θ range, 0.016° 2θ increments between points, an integration time of 0.1 second per point and 15 rotations per minute.

2.2.2: Infrared spectroscopy

IR measurements were performed on a Bruker Tensor 37 spectrometer with the MIRacle ATR stage from Pike Technologies. Powders and substrates (face-down) were pressed to the ATR crystal ensuring optimal contact and then the spectrum was taken. The range that has been looked into is 4000-600 cm⁻¹. In general 32 scans were averaged per spectrum. The resolution is 4 cm⁻¹. In all cases the background was measured in ambient conditions without any material on the crystal.

2.2.3: Thermogravimetric analysis

TGA has been performed on a TA instruments Q50 TGA. The samples were held in a platinum pan which was cleaned first by a blowtorch and then was loaded with about 10 mg of material. The analyses were started at room temperature and heating was done up to 1000 °C. The heating rate was 5 °C/min. During the analysis a gentle stream of N₂ was applied.

2.2.4: Scanning electron microscopy

SEM was performed using a Philips/FEI XL30 SFESEM. The acceleration voltage is 15 kV unless noted otherwise. Images were acquired using the detector for back-scattered electrons. If another detector was used this will be mentioned. The scale of each topograph will be mentioned in the image.

2.2.5: UV-Visible spectroscopy

UV-Vis measurements were performed on two different devices. First on an Varian Cary 50 UV-Vis spectrometer. Measurements were done in the range of 1000 nm to 300 nm. For immobilized samples a clean FTO substrate was used for the baseline. For powdered samples the solvent in which they were dispersed was used for a baseline. Other UV-Vis spectra were taken on a Craic technologies microscope spectrophotometer. These were done in a range from 800 nm to 300 nm using the reflectance mode with a 75 W power supply Xenon light source.

2.2.6: Electrochemistry and photoelectrochemistry

The configuration of a photoelectrochemical cell or a PEC cell is shown in Figure 2.1. A three-electrode setup is used in this research, and will be explained. The three electrodes are the working electrode (WE), the counter electrode (CE) and the reference electrode (RE).^[118] The working electrode is the most interesting of the three, being the studied sample. This is the electrode at which the potential is applied and absorbs light when performing photoelectrochemical tests. Since only the reduction or oxidation is being studied on the WE at a certain point there is need for another electrode to perform the other reaction. This is the counter electrode. The counter electrode often is Pt, because Pt can catalyze many redox reactions. This is necessary because it is important to make sure the reaction at the CE is not the limiting half reaction while studying the WE. Finally there is the reference electrode. This electrode is connected to the WE and measures which potential is present at the

WE. Preferably this reference electrode is the reversible hydrogen electrode (RHE) since it takes into account the pH of the electrolyte. Other examples of reference electrodes are the normal hydrogen electrode (NHE) and the Ag/AgCl reference electrode.^[118]

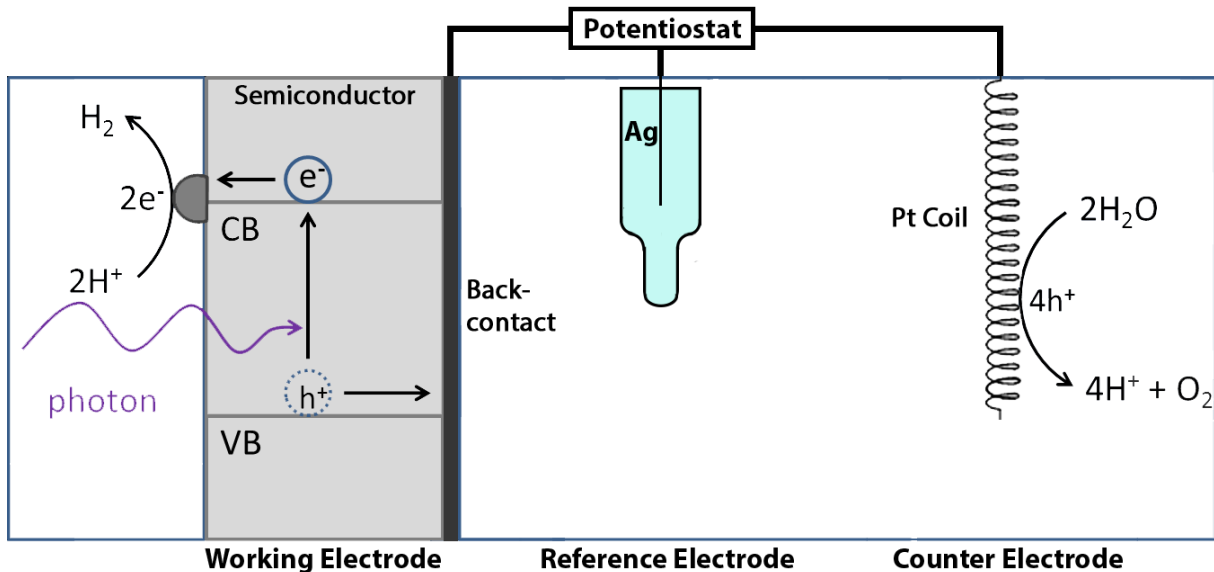


Figure 2.1: Schematic representation of a PEC setup. Here the different electrodes, WE (working electrode), CE (counter electrode) and RE (reference electrode) are indicated. All connected to a potentiostat.

The last practical aspect to consider is the evolution of products. Since the catalyst is confined to a single location in the electrolyte issues like mass transport limitations of the reactants can occur. This cannot be simply solved by stirring the electrolyte, because stirring disturbs the electrical interaction between the electrodes and in turn disturbs the electrochemical measurement. Slowing the scan rate on the sample allows the electrolyte more time to equilibrate lowering the effects of mass transport limitation. Another way this problem is sometimes tackled is by using the rotating disk electrode. The rotation of this electrode lowers mass transport limitations while the influence on the electrical response is limited.^[118]

During electrochemical tests the most general manner to plot the results is in a linear or cyclic voltammogram. Here the current (or current density if the surface of the WE is known) is measured while the potential is being changed. In a linear voltammogram the potential is moved from the starting potential to the ending potential once. For cyclic voltammetry (CV) the potential is swept between two potentials for several cycles. The current that is being measured corresponds to the amount of charge carriers being transported through the electrolyte, through redox chemistry. These techniques can be applied with or without illuminating the sample, allowing for a comparison between dark and light behavior and giving an extent to which the material is catalytically active and how well it can utilize light to perform

this catalysis. This yields information what property of the material should be improved.^[118]

By definition the potential at the WE electrode is positive if it is accepting electrons, meaning oxidations are taking place at the surface. If it is negative it is donating electrons and thus reductions are taking place at the WE. Take heed that in a PEC cell the photoanode is the electrode where the oxidation takes place, and the photocathode is the electrode where the reduction takes place.^[118]

Electrochemical measurements were performed using an Autolab PGstat204 potentiostat. During measurements a Pt wire or coil was used as a counter electrode while an aqueous Ag/AgCl electrode or DMF-based Ag electrode was used as a reference electrode. The electrodes were arranged in a glass container so that the reference was behind a frit, and the counter and working electrodes were far apart. The glass cell was filled with electrolyte (aqueous, DMF or acetonitrile (MeCN) based). The aqueous electrolyte was buffered with phosphate salts (0.0054 M NaH₂PO₄ and 0.0046 M Na₂HPO₄, pH of about 6.8). In the organic electrolytes TBAB (0.01 M) was dissolved as a supporting electrolyte to improve conductivity. Cyclic voltammetry was the electrochemical measurement of choice and was run with different rates and voltage ranges, these will be mentioned by the voltammograms in the results.

For photoelectrochemical testing a teflon cell with quartz windows was used, along with an Ivium CompactStat potentiostat. Similar to the electrochemical measurements the cell was filled with an electrolyte which was buffered or contained a supporting electrolyte. Cyclic voltammetry was again the measurement of choice and the parameters will be mentioned at the results. During the measurements the sample could be illuminated with a light beam ($35 \text{ W/cm}^2 \pm 2\text{W/cm}^2$) with a 75W Xenon arc lamp from the Optical Building Blocks Corporation as a light source, filtered with UV and IR filters from Optical Building Blocks Corporation to cut off parts of the UV (<420 nm) and IR (>1000 nm) to simulate the solar spectrum better. When illuminated the cycle will be referred to as "light", when the light was stopped from reaching the sample the cycle is referred to as "dark".

Three different electrolytes have been used: water with a phosphate buffer, water with sodium sulfate and acetonitrile (MeCN) with tertbutylammonium bromide (TBAB). For the first electrolyte 0.13182 g of HNa₂PO₄ and 0.12869 g of H₂NaPO₄ were dissolved in 200 mL demiwasser. As the second electrolyte a 0.2 M NaSO₄ solution was prepared. When using either of these two electrolytes a commercial Ag/AgCl reference electrode was used.

The third electrolyte was prepared by dissolving 4.33933 g TBAB in 150 mL MeCN (aged so that there was some water present), before measuring with this electrolyte it was deoxygenated by bubbling through nitrogen for 20 minutes. For some measurements using this electrolyte the sample was first treated with I₂. In these cases the samples were immersed in a solution of 25.781 g/L I₂ in MeCN for 2 hours.

A non-aqueous reference electrode was prepared for measurements with this electrolyte.

This electrode was prepared as follows. A cleaned glass body was filled with DMF and stored in a vial containing DMF for one hour to make sure the frit was mostly saturated with DMF. After that, the glass body was emptied and filled with a solution of 2.472 mM AgNO₃ and 100.38 mM TBAB in DMF. Finally a Ag wire, cleaned with sandpaper, demiwater and finally acetone, was added and the system was closed with parafilm. This electrode was stored in DMF for at least 72 hours to make sure it was stabilized.

2.2.7: Photocatalysis and online H₂ detection by gas chromatography

Generally photocatalysis is performed in slurry reactors. Such a reactor can be described as a vessel containing a suspension of the photocatalyst particles which is often stirred. This reactor can be designed to optimize the flux of light into the suspension and the suspension in turn can be optimized (for example concentration, stirring speed) to optimize light absorption by the particles. In the case of water splitting these particles are suspended in the reactant, water. The particles can donate their electron to protons to generate hydrogen. In concert they can accept electrons from water to generate oxygen.^[5, 6]

When testing the photocatalytic activity of a sample there are several important things to consider for the setup and several parameters which can greatly influence the experiment. The first thing that will be discussed is the light source (Figure 2.2). It is necessary to know the output of the lamp and the spectrum, otherwise comparing results becomes very hard. Generally light sources are Xe arc lamps or Hg halide lamps, since both emit a spectrum quite similar to the solar spectrum. Apart from the spectrum the intensity of the light is also important to know. 1 sun refers to a beam with an intensity of 1360 W/m² with a spectrum similar to that of sunlight at 1.5AM. This is the intensity that is often chosen to perform photodriven reactions because it is an intensity that corresponds to that of actual sunlight. Lower or higher intensities are also possible to be chosen, as long as it is known what intensity is measured at.

The intensity and composition of the light beam reaching the sample can be regulated by optics and filters (Figure 2.2). The spot size of the beam is also important. Generally not the entire sample will be illuminated and then the spot size will certainly influence the amount of photons being absorbed. For example if 0.10 W of light is concentrated on 1 cm² of the sample more will pass than when 0.10 W is concentrated on 2 cm². In the latter case photons are two times more likely to be absorbed, because there is two times as much particles being encountered by the photons.^[119, 120]

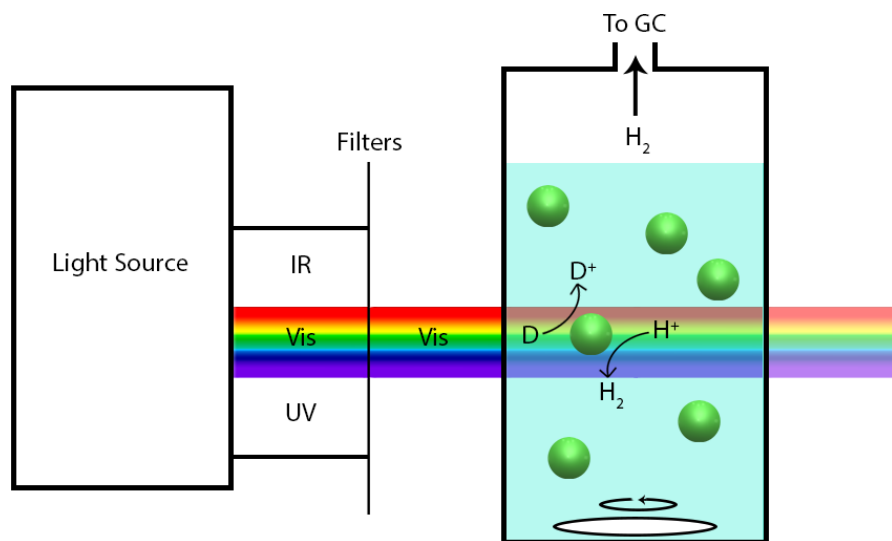


Figure 2.2: Schematic representation of a photocatalytic testing setup, this particular setup is connected to a GC. The light source is indicated as well as filters cutting UV and IR radiation. The stirred reaction container is seen where proton reduction takes place and where electron donors are consumed as the oxidation half-reaction.

The mentioned lamps emit a spectrum that is comparable to the spectrum of the sun, but only in the visible (420-700 nm) region of the spectrum. The intensity of these lamps in the UV-region of the spectrum (<420 nm) is far too high. To make sure the results of a photocatalytic test are acceptable filters are used to cut away the light below 420 nm. Glass is sufficient for this. The intensity of the IR-region (>700 nm) does also not match very well with sunlight, however many materials are incapable of absorbing light in this region. However, some scientists cut this part of the light as well by using a filter as well, this can be water for example. Finally there is the homogeneity of the lamp to consider, the light spots of many lamps are not homogeneous, meaning they have fluctuating hotspots where light intensity is higher. [120] The general output of the lamp is more often quite constant however. To be more certain of the ingoing flux most photocatalytic setups make sure that the entire light spot reaches the sample so that the output of the lamp can be used as the incident energy, if this is neglected then there could be a difference in photocatalytic response of samples simply because one sample happened to be in a hotspot whereas the other was not. [120]

The other part of the setup that is important to consider is the vessel containing the sample and electrolyte (Figure 2.2). First of all it is important that the light, of which the intensity was determined before, can pass into the vessel undisturbed. This is possible by using a flat quartz window. Also the material of the vessel is important, it should be stable in electrolytes and stable towards intense light beams. The shape of the vessel is important as well. A closed backside reflects light, allowing the light beam to pass through the solution twice. A window on the backside only allows light to pass once, being more certain of the path length at the cost of the absolute reaction turnover. One should consider that the sample might already absorb all the light

halfway through and then it can be ascribed a lower activity than it actually has, simply because only half the sample can perform the reaction.^[119, 120]

For the electrolyte there are several factors to consider: the amount of catalyst, the solvent and possible solutes in the system and finally convection. The amount of catalyst that will be put into the solution is important since too much risks only using a part of the sample because the light will not penetrate deep enough. On the other hand, having a low loading will mean that only a small part of the light is absorbed and that the amount of product evolved will be harder to determine. It is convenient to maintain a similar the loading in each case, because then comparing the results is far more facile.

Important is that the catalyst is stable in the electrolyte. Preferably the electrolyte is water-based, but if the catalyst is unstable in aqueous media organic electrolytes are a possibility. Most electrolytes contain solutes like sodium nitrate to improve the conductivity. Materials like TEA, TEOA or methanol are often added as hole scavengers/electron donors when a reduction reaction is being studied in detail. Compounds like vinyl chloride (VC) can be added as electron scavengers/acceptors when studying an oxidation in detail. Another compound that can act like an electron acceptor and which is present often is oxygen. This is why an electrolyte is often deoxygenated, especially if the reduction reaction is of interest. This can be done by bubbling an inert gas, like N₂, through the solution for some time.

During photocatalytic testing there is one more practical issue. A solid catalyst will settle down on the bottom of a vessel after some time. This means there should be constant convection in the vessel. A straightforward and generally used method of doing so is by simply using a magnetic stirrer (Figure 2.2). Another way that is sometimes used is by continuously bubbling through a gas like N₂. The latter case makes sure the amount of oxygen in the electrolyte is kept to a minimum, however convection by bubbling through a gas is less reproducible. Scientists have also considered if bubbles affect the light propagation in the electrolyte, but found that influence is insignificant.^[121]

Finally product detection is important. Preferably this is done at as much time points as practically possible. When the product is gaseous, like hydrogen or oxygen, which is the case for water splitting one can use gas chromatography (GC) (Figure 2.2) or by online electrochemical mass spectrometry (OLEMS). When the product remains dissolved, as would be the case with HCOO⁻, one needs other means to detect the product. One way is by drawing samples at time intervals and using high performance liquid chromatography (HPLC) to determine the dissolved products. Important in either case is to make sure that measurements are done at several points during the measurement to detect if there is any catalyst deactivation or activation during the process, same as for tests with other types of catalysis.

In this research a setup in Eindhoven has been used. A schematic representation provided by Anton Litke is given in Figure 2.3. A represents the light source, which is a 500 W Xe/Hg lamp. This light is filtered by water (C) and an UV cutoff filter (D). The beam splitter at F sends a small fraction of light to the photosensor (G). This

sensor gives feedback to the light source to stabilize the light output. The remainder of the light reaches the cooled and stirred reactor (I), which is connected to a GC (R & S).

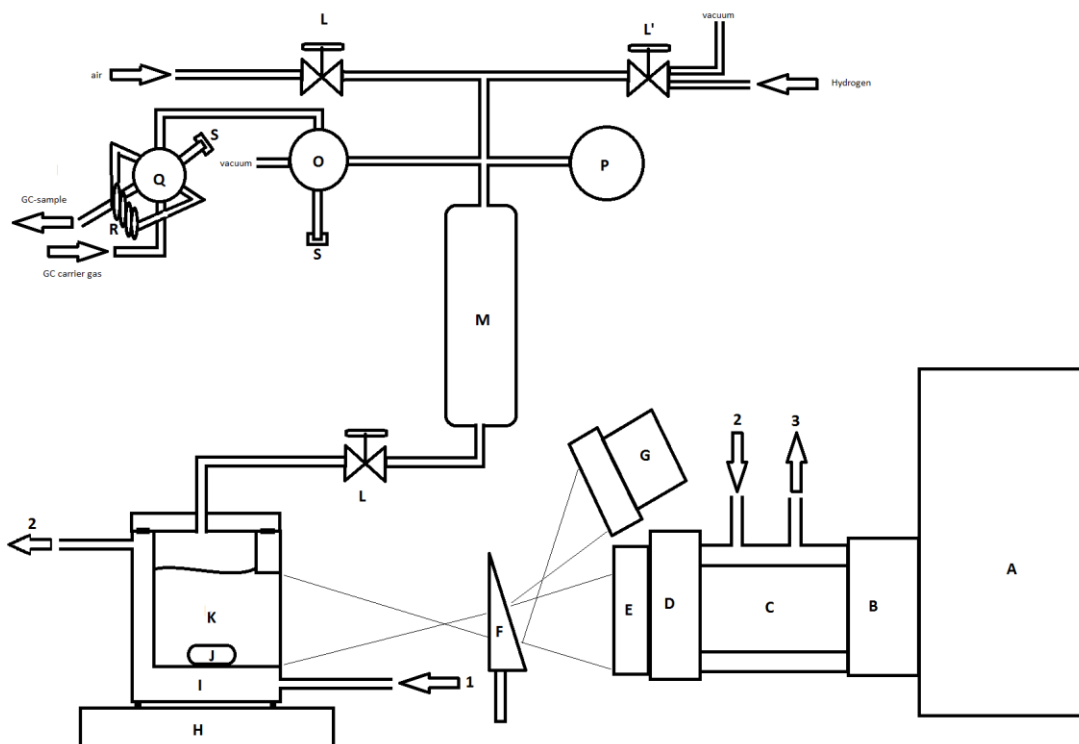


Figure 2.3: Schematic representation of the setup for testing the photocatalytic activity. The letters represent: (A) Light source(500 W, Xe/Hg lamp), (B) Collimated condenser, (C) IR-filter (water), (D) 420 nm high-pass filter, (E) convex lens, (F) Beam splitter, (G) Photosensor, (H) Stirring plate, (I) Reactor with cooling mantel, (J) Stirring magnet, (K) Liquid with sacrificial reagent and dispersed photocatalyst, (L)&(L') manual 2- and 3-way valves resp., (M) Headspace, (O) motorized 4-way valve, (P) Pressure gauge, (Q) motorized 6-way valve, (R) 1 mL loop of tubing and (S) end caps. The numbers represent cooling water: (1) from cooler/pump, (2) from reactor to IR-filter and (3) back to cooler/pump.

The entire system has a volume of 133.8 mL. GC is sampled every 30 minutes and 1 mL of the entire volume is being analyzed every time. To evaluate the total amount of hydrogen generated at a certain point the measured amount of hydrogen is multiplied by the gaseous volume, divided by the volume of the analyzed gas. So, say there is 60 mL of liquid present the measured amount of hydrogen is multiplied by 73.8 to give the real amount of hydrogen generated at that point.

The first measurements were performed in an aqueous solution of 0.7408 g/L NaH₂PO₄ · H₂O (Acros organics) and 0.6568 g/L Na₂HPO₄ (Merck) using Milli-Q filtered water. 50 mL of this solution was mixed with 5 mL TEA. Only Bat-9 is used as a photocatalyst if any was present and 9.7 mg was used if this was the case. For the other measurements just 50 mL Milli-Q filtered water was used mixed with 10 mL methanol. In these cases 20 mg of catalyst was used, except for Bat-11 where 19.9 mg was used.

2.2.8: Transient absorption spectroscopy

One of the techniques used in this research is transient absorption spectroscopy (TAS). This technique measures the light absorption spectrum of a sample in its excited state. It does so by using two laser pulses. The first excites the sample and the second probes the sample to obtain the spectrum, generally in the UV-Vis region (Figure 2.4). By changing the delay between the two pulses one can see the change in absorption over time in at very small time differences, down to attoseconds (10^{-18} s). The time resolution of the technique depends on the lasers.^[122-124]

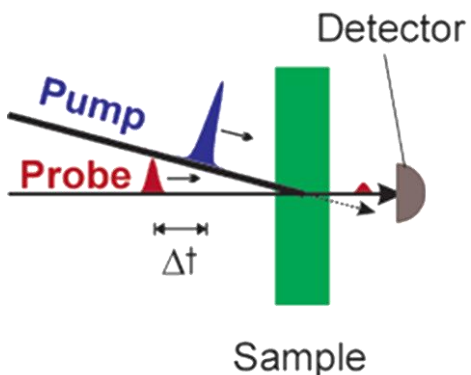


Figure 2.4: A schematic representation of the pump-probe measurement.

Both lasers are pulsed. Two considerations important here: the frequency of the pulses and the durations of the pulses. The frequency of the pulses determines the timescale one can look into. Assuming pulses of very short duration a laser with a frequency of 10 Hz, meaning 10 pulses per second, will allow measurements with a Δt up to 100 ms. Then the next pulse arrives and the next measurement starts. A slower laser, one with a frequency of 1 Hz will be able to measure Δt values up to 1000 ms. The frequency is mainly important for the pump laser, which is the laser that gives the exciting pulses. The probe laser, the one that gives the scanning pulses, just should be faster so that the absorption can be measured before the second pump pulse arrives.^[122]

The duration of the pulses determines the lower border of the time resolution that can be attained. If the pulse takes 100 ps ($ps = 10^{-12}$ s) then the resolution that can be attained is about 50 ps. This depends on the duration of both pulses. If the pump pulse takes long the excited electrons from the start might already have changed in energy before the pulse ends, in other words the duration of the pump pulse determines at what difference in time the measurement can start. The duration of the probe pulse is important because most detectors cannot distinguish between the beginning of the pulse and the end of the pulse because they are not fast enough. This means that if the probe pulse takes 100 ps, the signal that is put out by the detector is the sum of the absorption during the entire pulse. However, since most of the intensity in a pulse is often concentrated in the middle (the distribution can be

assumed to be Gaussian) the resolution can be assumed to be better, somewhere around half the duration of the pulse, so 50 ps in this case.^[122]

This technique is very interesting for studying photodriven reactions because it allows looking into the dynamics of the charge carriers and how they respond to light. TAS can be used to track the charge carriers in time, determining the states they settle into, seeing if there are trap states where charges will get stuck and observing the life times of each. One can track catalysts in situ and see how different pH or reactant concentration influences the depletion of charge carriers.^[122-124]

TAS measurements were performed with an EOS spectrophotometer. A schematic representation of this setup can be seen in Figure 2.5. The pump laser includes a Nd:YAG crystal which is used to generate a laser pulse with a wavelength of 1064 nm, an adjustable repetition rate between 1 Hz and 1 kHz, and a duration under 1.8 ns. For the measurements the repetition rate 1 kHz unless noted otherwise. The laser system of this pump has a harmonic generator which transforms this beam into separate beams of 532 nm, 355 nm and 266 nm from which one can be selected to act as the pump. The wavelength that has been used for the pump will be mentioned with each experiment given in the results. The wavelength of the pump beam is selected before it enters the setup depicted in Figure 2.5. Using the neutral density filter ND1 the power of the pump pulse can be regulated.

The probe pulse is generated by a LEUKOS super continuum light source. This laser generates a wide spectrum and with the visible detector in this setup allows for a spectral acquisition from 350 nm to 850 nm with a spectral resolution of 1.5 nm. The repetition rate of the laser is 2 kHz. The pulse duration of this laser is below 1.2 ns and as a result as a temporal resolution below 1 ns.

The probe pulse is split by the special neutral density filter or beam splitter called BS1. This filter lets part of the light pass through while the other part is reflected as shown in the schematic. The ratio of passing and reflected light can be adjusted. The reflected beam is redirected to the detector FO2 where the reference spectrum is determined. The passing light enters the sample and the transmitted light is then directed to detector FO1 where the transmitted spectrum is detected. The difference between FO1 and FO2 then gives the absorption spectrum.

During the measurement points will be probed several times. Thus depending on the measurement duration the signal-to-noise ratio may differ. The measurement time of all data will be given in the results section since it is different for each sample. Samples have been purged with N₂ for at least 7 minutes unless noted otherwise.

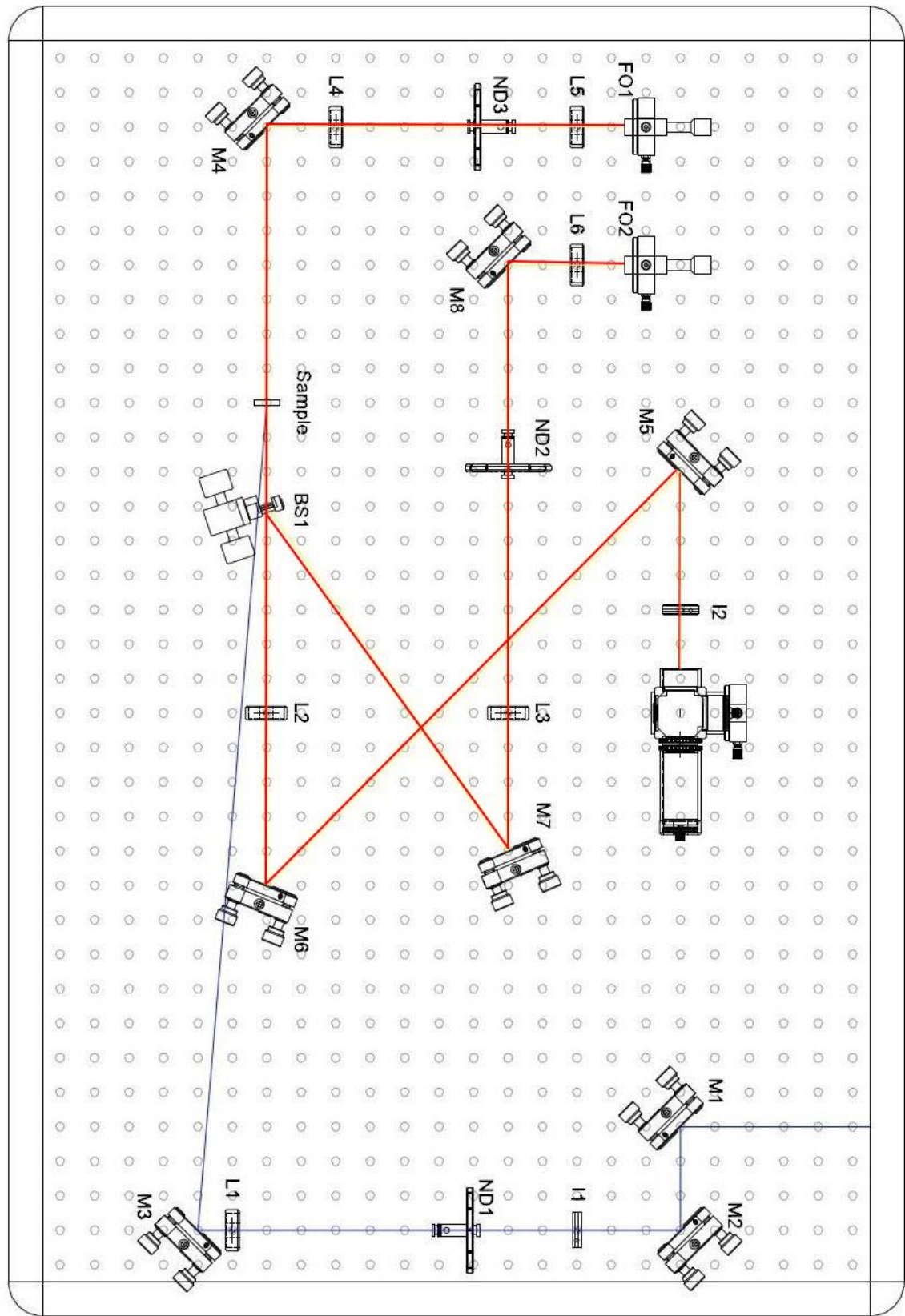


Figure 2.5: Schematic representation of the TAS-setup. The black line represents the path of the pump laser beam that enters in the lower right corner, the red line represents the probe laser beam path. The acronyms stand for the following: M = Mirror, ND = Neutral density filter, L = Lens, BS = Beamsplitter, FO = Fiber optics (detectors), I = Iris (diaphragm). This image is taken from the EOS manual.

3. Results: MOF Photoelectrodes

In this chapter the results obtained for the prepared MOF electrodes will be given. MOF immobilization on FTO is challenging, so first the structural characterization of several films will be discussed in Section 3.1. Once it is confirmed the immobilization has succeeded and that the materials are the expected MOF structures the electrodes will be studied using the photoelectrochemical setup. These results will be discussed in Section 3.2. Finally the observations will be summarized and explanations of the results will be touched upon in Section 3.3.

3.1. Structural characterization

As described in Chapter 2 the films have been synthesized in two general ways, either by the solvothermal route or by dropcasting. However, after the samples had been prepared, it was observed that the films obtained by the solvothermal route were very poorly attached to the FTO. In fact, the films could be removed by simply scratching them with a cotton tip. This lack of stability of the film resulted in characterization being impossible for samples prepared through this route. The other films, prepared by the solvothermal method, did show a good mechanical stability however. These films have been studied by XRD and SEM to check if the samples are crystalline and homogeneous, and by UV-Vis spectroscopy and IR spectroscopy to validate the chemical composition.

Four different MOFs that have been immobilized using the solvothermal route will be discussed in detail in this section. These are Zr(ATA)/HCl (Sur-16 and Sur-20), Cu(DABCO)(ATA)/DQ (Sur-9, Sur-17), Co(ATA)/DQ (Sur-18) and Ti(DHTA)/DQ (Sur-19 and Sur-21). Each MOF film will be discussed separately using their powder counterpart as a reference.

First the Zr(ATA)/HCl films will be discussed. In Figure 3.1 the XRD data is shown for Sur-16b as film and Bat-4 as powder. It can be observed that the first two diffraction peaks of this MOF in the film and powder are alike. The less intense diffraction peaks present in the powder are not observed for the film. It is likely these diffractions are too weak to be observed with this signal-to-noise ratio. Also observed is the first diffraction peak belonging to FTO at $32^\circ 2\theta$. This has been validated by comparing it to a slide of bare FTO. The fact that the X-ray beam can penetrate the sample enough to observe this FTO diffraction results from the obtained film being relatively thin, few μm at most. This is in agreement with the transparency of the film which is observed.

However, XRD does not show whether the obtained film is homogeneously distributed over the FTO. For this SEM topography is used. In Figure 3.2 SEM topographs are shown at different magnifications. During these measurements a homogeneous film of Zr(ATA) particles, of about 100 nm in diameter each, has been observed covering the FTO. As seen in image B at some areas small agglomerates of several, larger MOF particles of about 200-300 nm in diameter each have been observed.

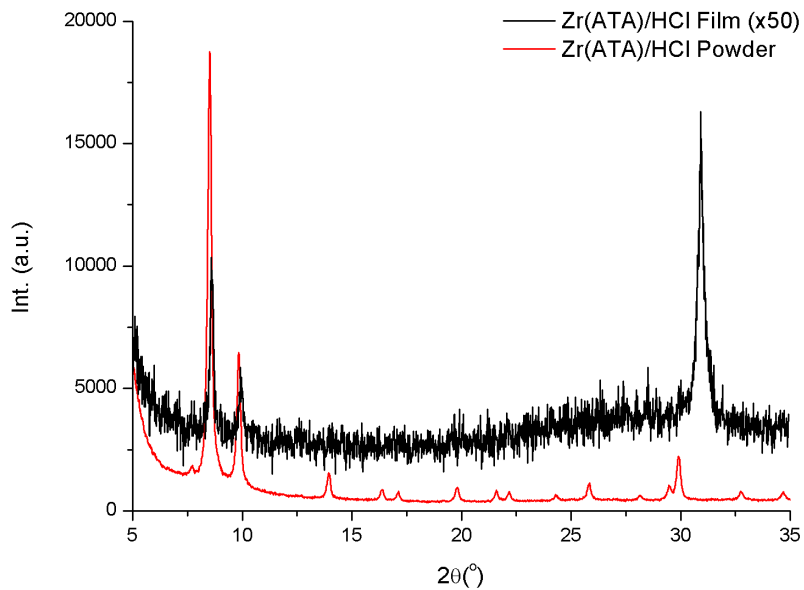


Figure 3.1: XRD data for Zr(ATA)/HCl, Sur-16b (Black) and the Zr(ATA)/HCl powder, Bat-4 (Red).

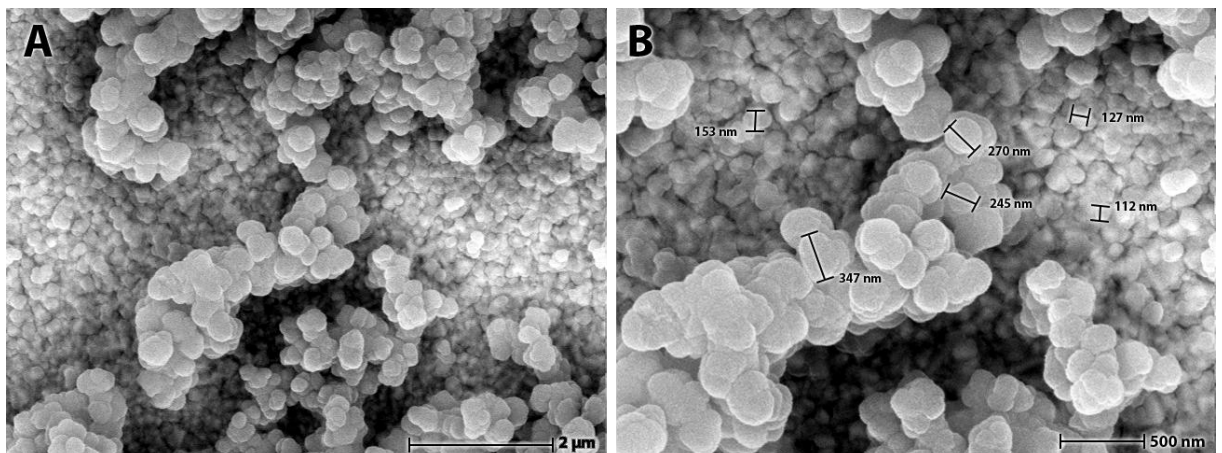


Figure 3.2: SEM topographs of Zr(ATA)/HCl, Sur-16b at different magnifications. Scale bars are indicated.

The chemical nature of the film was investigated as well. Using IR spectroscopy (Figure 3.3) and UV-Vis spectroscopy (Figure 3.4) it can be observed that chemically the film and the powder are similar materials. The IR spectra completely overlap, assignment of the peaks will be done in detail in Chapter 4. The UV-Vis spectra of the films Sur-16c and Sur-20 show absorption bands at 340 nm, 370 nm and weaker bands at 510 nm and 670 nm. For the powder Bat-4 only the bands at 340 nm and 370 nm are observed. However due to light scattering by powdery samples the other, weaker, bands could be lost in the noise.

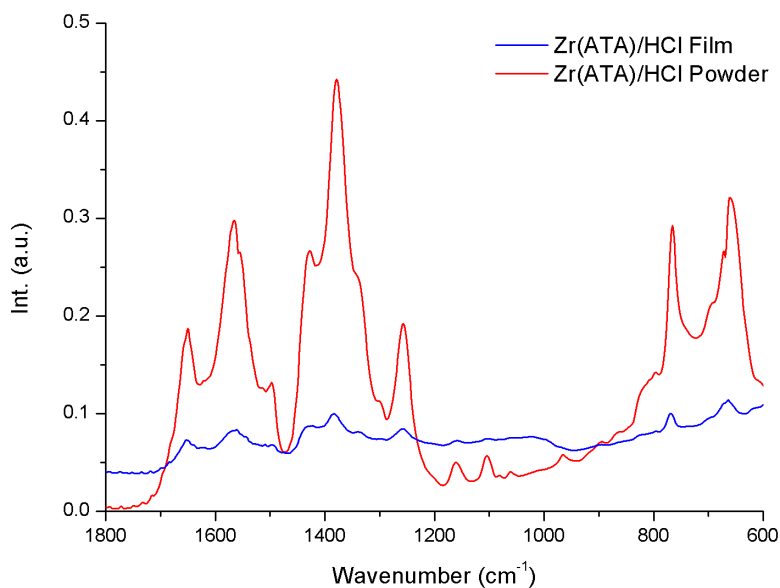


Figure 3.3: IR spectra of Zr(ATA)/HCl, Sur-20 (Blue) and the Zr(ATA)/HCl powder Bat-4 (Red).

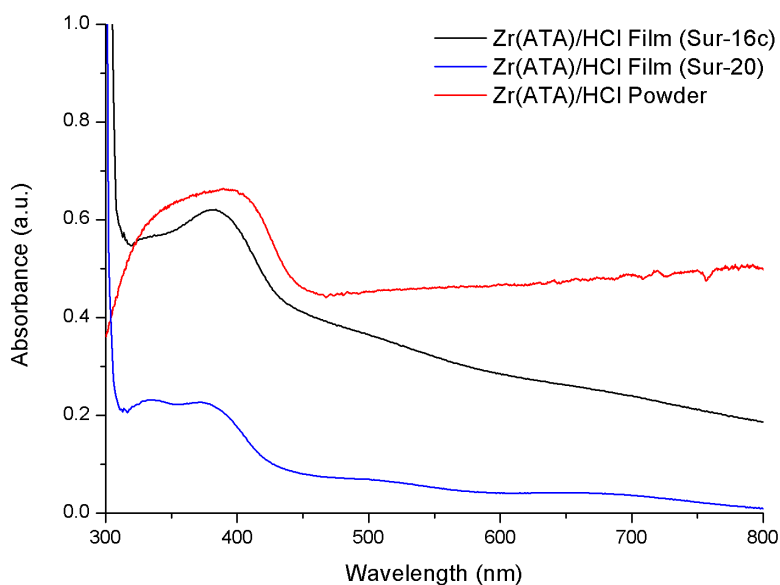


Figure 3.4: Transmission UV-Vis spectra of Zr(ATA)/HCl, Sur-16c (Black), Sur-20 (Blue) and the Reflectance UV-Vis spectrum of the Zr(ATA)/HCl powder Bat-4 (Red).

The Zr(ATA) set of films Sur-1 to Sur-7 yielded similar results. From this it can be concluded that the proto-MOF pretreatment does not improve, nor hamper the synthesis. However, it was found that the syntheses with HCl present as a promotor and with the highest concentration of precursors were best to form MOF films.

For the Cu(DABCO)(ATA)/DQ MOF films XRD, IR and UV-Vis have been used to characterize the films. With XRD it was observed that the Cu(DABCO)(ATA)/DQ film was not crystalline at all, as seen in Figure 3.5. With IR spectroscopy (Figure 3.6) it can be observed that there is no match between the film and powder.

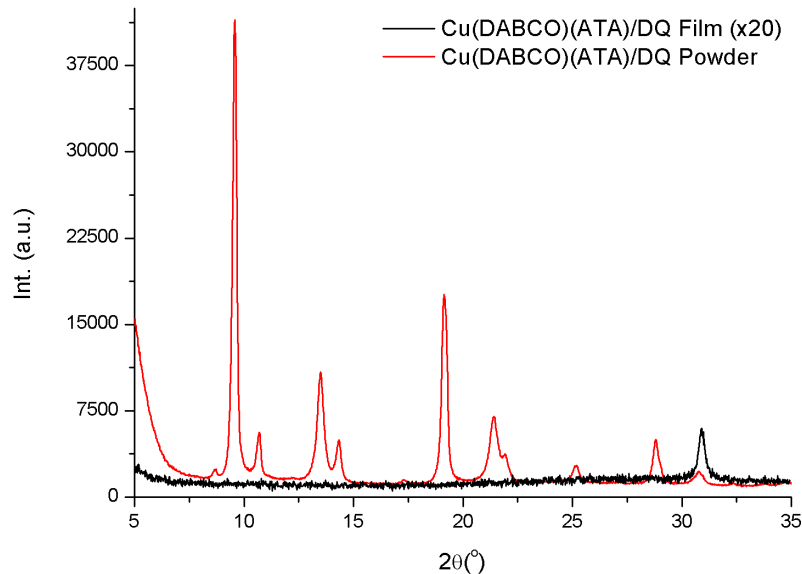


Figure 3.5: XRD data for Cu(DABCO)(ATA)/DQ, Sur-17 (Black) and the Cu(DABCO)(ATA)/DQ powder, Bat-11 (Red).

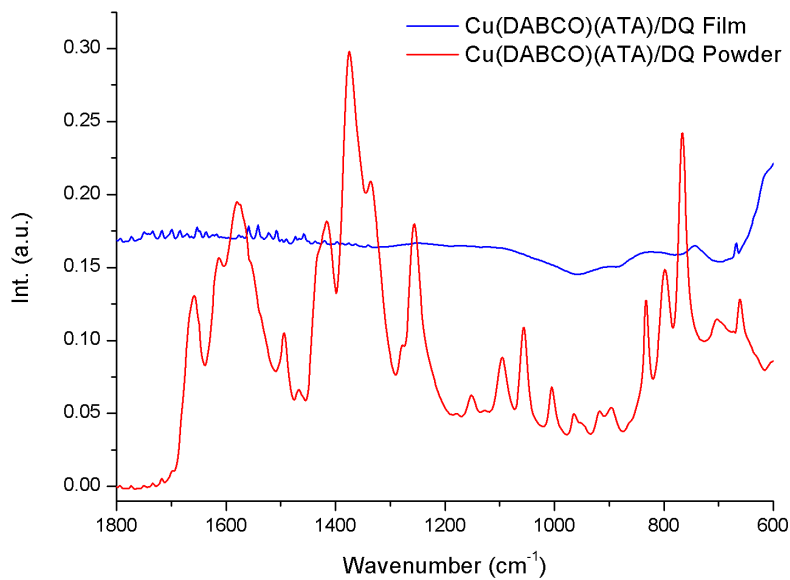


Figure 3.6: IR spectra for Cu(DABCO)(ATA)/DQ, Sur-9 (Blue) and the Cu(DABCO)(ATA)/DQ powder, Bat-11 (Red).

When comparing UV-Vis spectra for the film and powder an indication is seen that the light absorption is similar. For the film bands from 300 nm to about 900 nm are observed. For the powder a broad absorption between 300 nm and 800 nm is seen.

Again it can be expected that light scattering results in the loss of finer band structure for the powder.

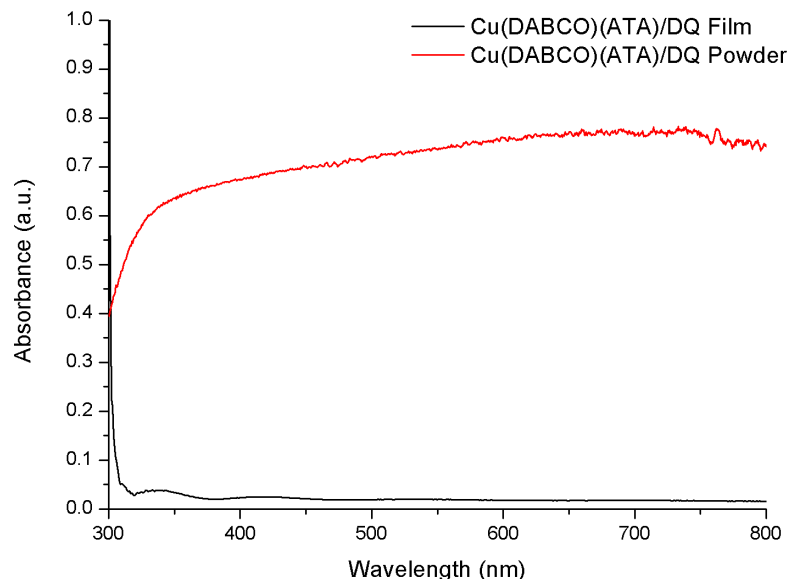


Figure 3.7: Transmission UV-Vis spectrum for Cu(DABCO)(ATA)/DQ, Sur-17 (Black) and the reflectance UV-Vis spectrum for the Cu(DABCO)(ATA)/DQ powder Bat-11 (Red).

So for the Cu(DABCO)(ATA)/DQ MOF the UV-Vis spectra give an indication that the MOF might have formed. However the lack of decent XRD and IR data, possibly due to the small thickness of the film, results in the characterization of this film to be inconclusive. Sur-8, Cu(DABCO)(ATA)/HCl, behaved similarly in terms of structure and chemistry.

For the Co(ATA)/DQ MOF (Sur-18) films XRD data showed that the hydrothermal synthesis can be quite sensitive. In Figure 3.8 the diffractograms of both Sur-18 samples (Sur-18_1 and Sur-18_2) are shown. These samples were synthesized simultaneously in the same vessel, yet a huge difference in crystallinity is observed. Possible explanations for this could be that one FTO slide might have had more nucleation points such as a small scratch or a dust particle on the surface. Such a nucleation point for the immobilization can yield a different crystallinity for the growing MOF sample.

When comparing to the Co(ATA)/DQ film to the powder it can be seen that the crystal structure of both films is the same as that of the powder. It can be observed as well that there is a strong preference for some diffraction peaks over others in the film, indicating the film has a preferential direction of growth.

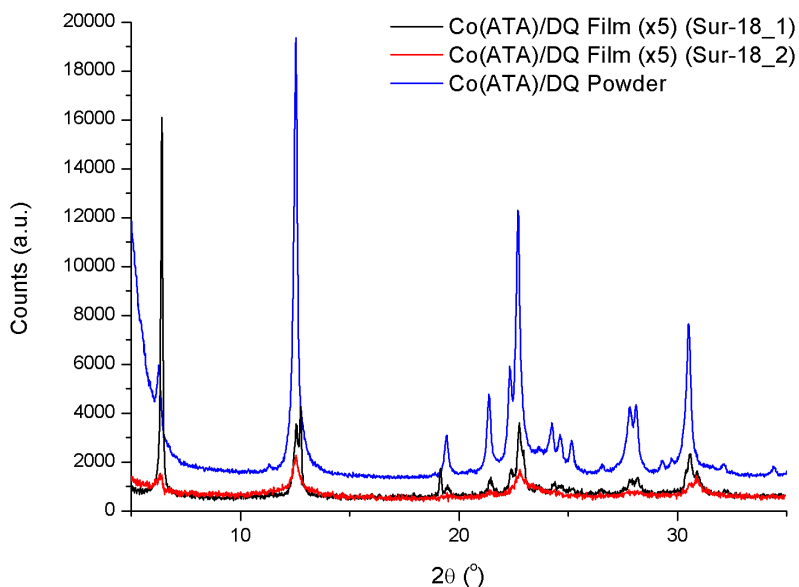


Figure 3.8: XRD data for Co(ATA)/DQ, Sur-18_1 (Black) and Sur-18_2 (Red) and the Co(ATA)/DQ powder, Bat-17 (Blue).

UV-Vis spectroscopy and IR spectroscopy have been performed on the crystalline film (Sur-18_1). In Figure 3.9 the IR spectra for the film and reference powder samples are compared. It is evident from these spectra that the chemical structure of these MOFs is similar. Same goes for the reflectance UV-Vis spectra of both shown in Figure 3.10. Transmission UV-Vis for these films did not yield useful spectra since the films were too dense and gave too high scattering backgrounds. The film was

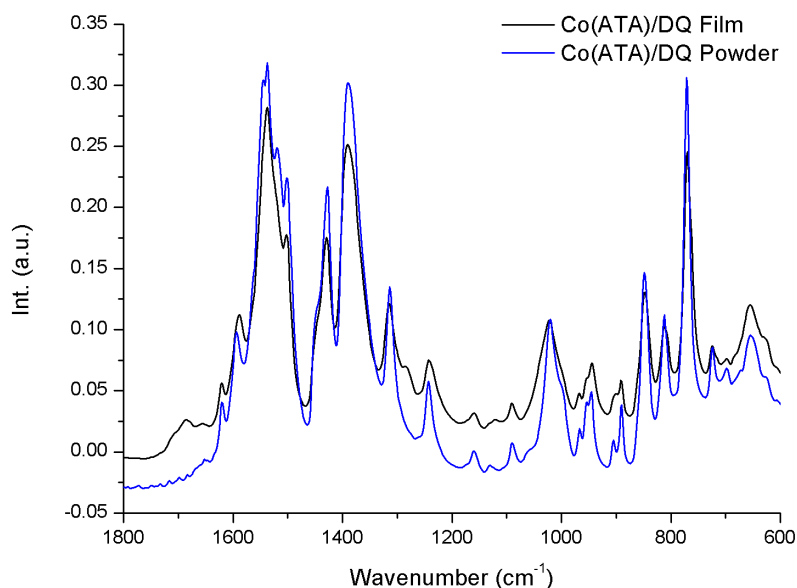


Figure 3.9: IR spectra for Co(ATA)/DQ, Sur-18_1 (Black) and the Co(ATA)/DQ powder, Bat-17 (Blue).

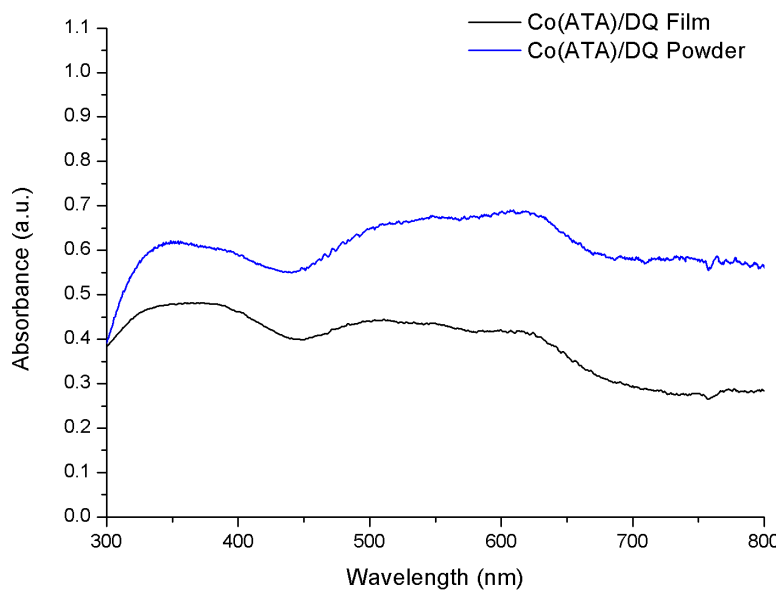


Figure 3.10: Reflectance UV-Vis spectra for Co(ATA)/DQ, Sur-18_1 (Black) and the Co(ATA)/DQ powder, Bat-17 (Blue).

dense enough for reflectance UV-Vis spectroscopy without getting too much interference of the FTO substrate however, so those spectra are used in this case. In this case as well it is evident that the chemical behavior is the same for both film and powder.

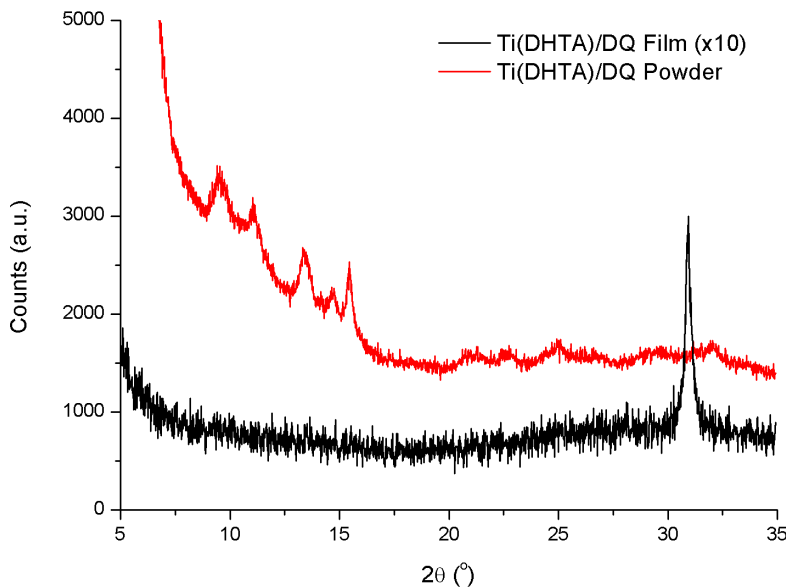


Figure 3.11: XRD data for Ti(DHTA)/DQ, Sur-19 (Black) and the Ti(DHTA)/DQ powder Bat-21 (Red).

Finally the Ti(DHTA)/DQ films Sur-19 and Sur-21 will be discussed. This MOF also formed dense films like the Co(ATA)/DQ. However, when comparing the XRD data

(Figure 3.11) to that of the reference powder, no diffraction peaks are observed for the film at all, as opposed to the Co(ATA)/DQ films. Only the diffraction peak for FTO can be observed. For the powder it is also observed that the crystallinity is low. So the observed lack of crystallinity of the film could be that the film is too thin to see these low diffractions or that the film is not crystalline.

With IR spectroscopy (Figure 3.12) it is observed that the spectra for both the film and the powder are the same, apart from the peak at 675 cm⁻¹. This is the region

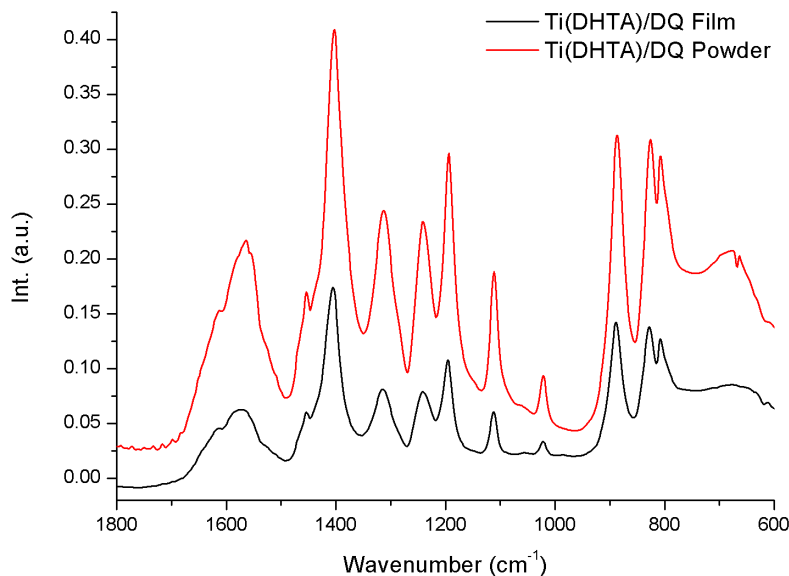


Figure 3.12: IR spectra for Ti(DHTA)/DQ, Sur-19 (Black) and the Ti(DHTA)/DQ powder Bat-21 (Red).

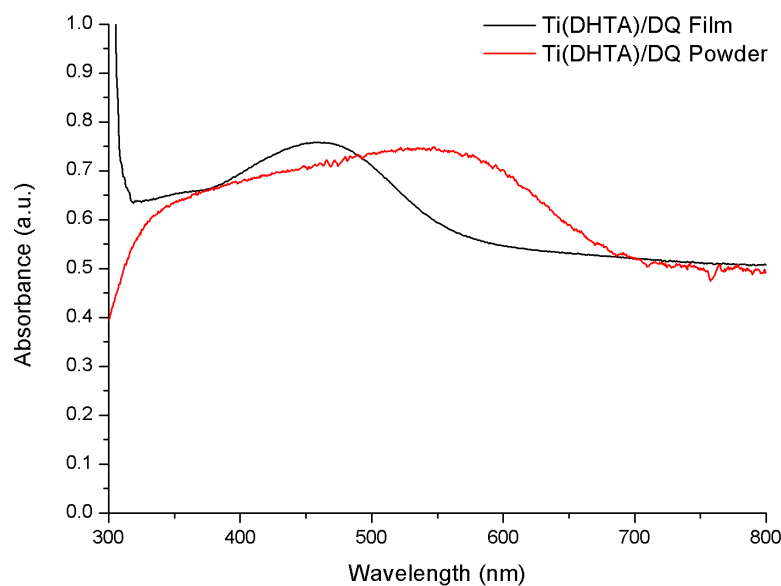


Figure 3.13: Transmission UV-Vis spectrum for Ti(DHTA)/DQ, Sur-19 (Black) and reflectance UV-Vis spectrum for the powder Ti(DHTA)/DQ Bat-21 (Red).

where the FTO substrate starts interfering with the IR measurement so that difference can be neglected. However, when comparing UV-Vis spectra, seen in Figure 3.13, we see that the absorption band of the powder extends up to 700 nm while the band for the film already stops at 600 nm. While in both cases the visible light absorption is more than sufficient to consider for photocatalytic purposes, it does show that there is a chemical difference in the MOF structure.

The SEM images of Sur-19, given in Figure 3.14, show that this MOF did not form a homogeneous film over the FTO. Instead, an inhomogeneous distribution of MOF particles is seen around which a lot of FTO is still bare. EDX measurements confirm that indeed at the bare positions there is no Ti edge present. The observed morphology for the particles is similar to that of the powder Ti(DHTA)/DQ, as will be evident from topographs shown in Chapter 4.

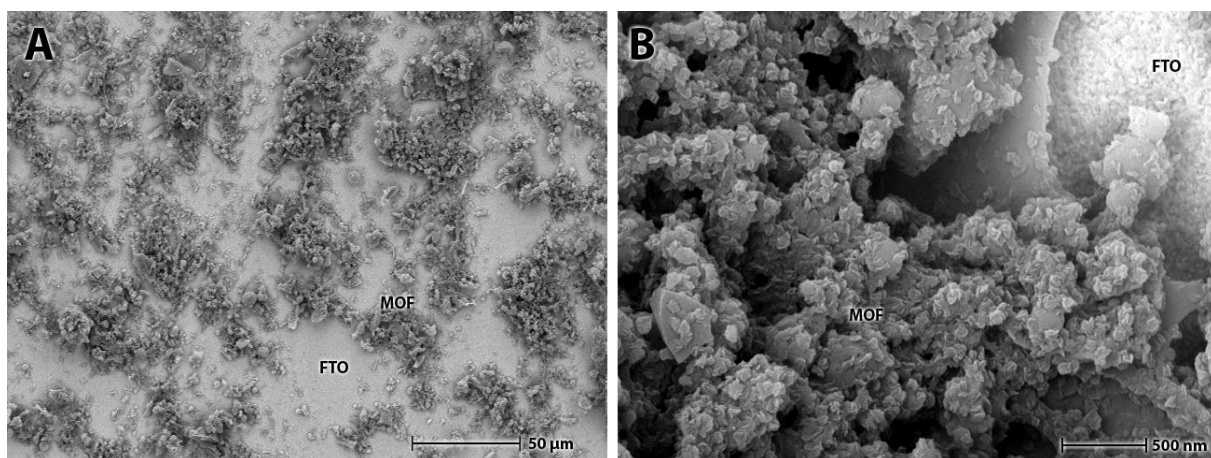


Figure 3.14: SEM topographs of Ti(DHTA)/DQ, Sur-19 at different magnifications. Scale bars are indicated.

For Sur-13, Ti(DHTA)/HCl, similar behavior in terms of structure and chemistry is found. The powder variety also showed that having HCl or DQ present as a promotor did not influence the synthesis for this MOF. This will be further illustrate in Section 4.1.

3.2. Photoelectrochemical characterization

For the films photoelectrochemical characterization can be used to explore the catalytic activity of the samples. All of the films discussed in Section 3.1 are discussed in this section as well. This is performed because for example a lower crystallinity is an indication for the presence of more defects in the structure. These defects can act as trap states for charge carriers but can also result free sites for catalysis on the metal nodes.

The first (photo)electrochemical tests were performed on the Zr(ATa) films Sur-1 to Sur-6. The electrolytes used for these were water-based buffered either with Na₂HPO₄ and NaH₂PO₄ (pH 6.8) or a solution with 0.2 M NaSO₄. Figure 3.15 shows

a CV which is representative of all tests performed on these six sets of samples for any of the two electrolytes. In this CV 4 cycles are performed of which the first three were in the dark and the last one under illumination. There are several observations. In the first cycle at 1.0 V a clear oxidation peak can be seen. This peak is irreversible as no corresponding reduction is observed when returning to lower potentials. Apart from that the profile of the sample is exactly the same as bare FTO (Figure A.1 in the Appendix) has in these circumstances. Finally no difference is seen when the sample is illuminated. To be sure the lack of light activity does not originate from the sample being destroyed in the first cycle a fresh film was also tried under light illumination and this yielded the same profile as well.

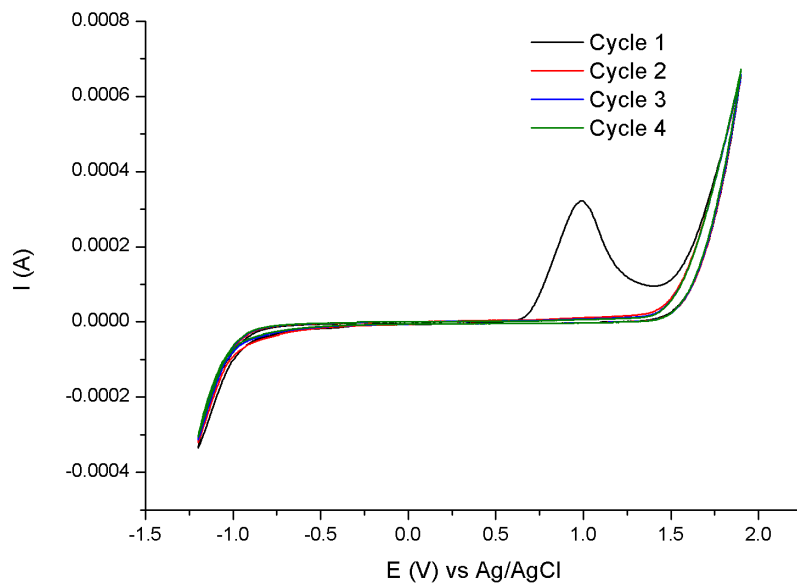


Figure 3.15: CV of Zr(ATa)/HCl, Sur-1a for 4 cycles, first 3 in the dark, last under illumination. The electrolyte used was water buffered with phosphates at pH 6.8. Potentials are given versus a Ag/AgCl counterelectrode.

From this measurement alone cannot be judged where this observed irreversible oxidation originates from. It is likely that the MOF structure is being oxidized, since the electrochemical response corresponds to bare FTO afterwards. This oxidation can be related to the presence of water however, so following electrochemical measurements are performed in an acetonitrile based electrolyte. Each cycle in the measurements performed in this electrolyte first go to negative potentials, before going to positive ones.

The Zr(ATa)/HCl film, Sur-16, was the first to be tested in this electrolyte. The CV data of this electrode is shown in Figure 3.16. In this measurement an irreversible reduction is seen in the first cycle on Zr(ATa). Then in the second and third cycle a small irreversible oxidation is observed. After the reduction event the film behaves similarly to FTO suggesting there is no catalytic activity of the MOF in terms of electrochemistry.

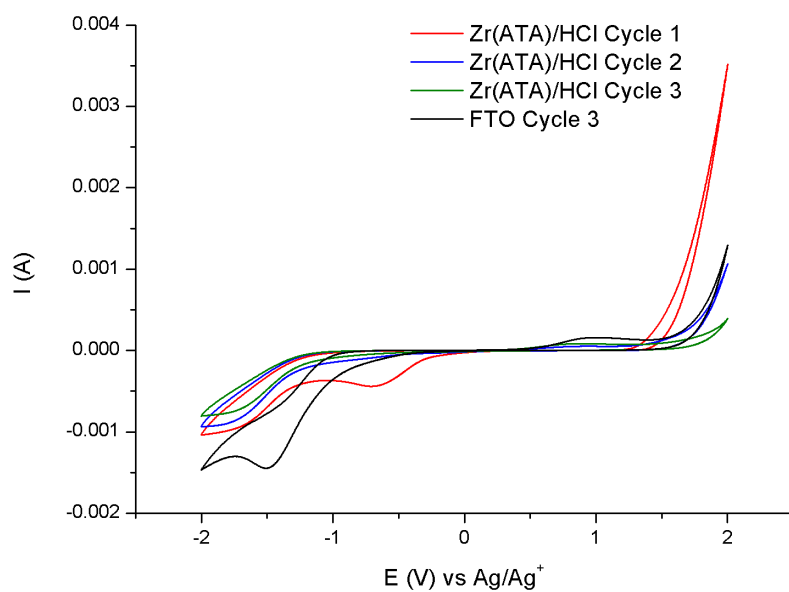


Figure 3.16: CV of Zr(ATA)/HCl, Sur-16, for 3 cycles in the dark. The third cycle of a measurement on bare FTO is seen as a reference (Black). This measurement is performed in an MeCN based electrolyte with a non-aqueous Ag/Ag⁺ reference electrode.

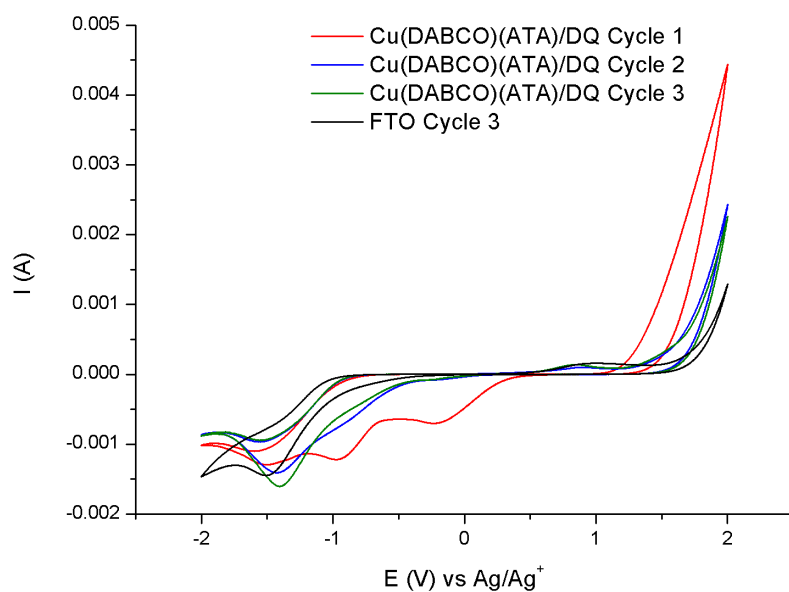


Figure 3.17: CV of Cu(DABCO)(ATA)/DQ, Sur-17, for 3 cycles in the dark. The third cycle of a measurement on bare FTO is given as a reference (Black). This measurement is performed in an MeCN based electrolyte with a non-aqueous Ag/Ag⁺ reference electrode.

The cyclic voltammogram of Cu(DABCO)(ATA)/DQ, Sur-17, is shown in Figure 3.17. For this film not one but two irreversible reductions are observed, after which the behavior corresponds to FTO. One possible explanation of the two observed reductions could be the reduction of Cu^{2+} to Cu^+ and then metallic Cu. A more detailed study is necessary however to confirm possible changes to the MOF structure however. It is certain the observed irreversible events are related to the MOF since the film was observed to have detached from the substrate.

The Co(ATA)/DQ film, Sur-18, showed no irreversible redox events in the CV, as seen in Figure 3.18. On the reduction part it performs similar to FTO but on the oxidation part it shows currents which are four times higher than FTO, meaning there is four times more conversion taking place. Also it starts this conversion at lower potentials suggesting there is less overpotential necessary for the reaction being observed there. In this work it could not be confirmed what reaction is taking place in this measurement. If this is for example water oxidation measurements like OLEMS are necessary to detect possible O_2 output.

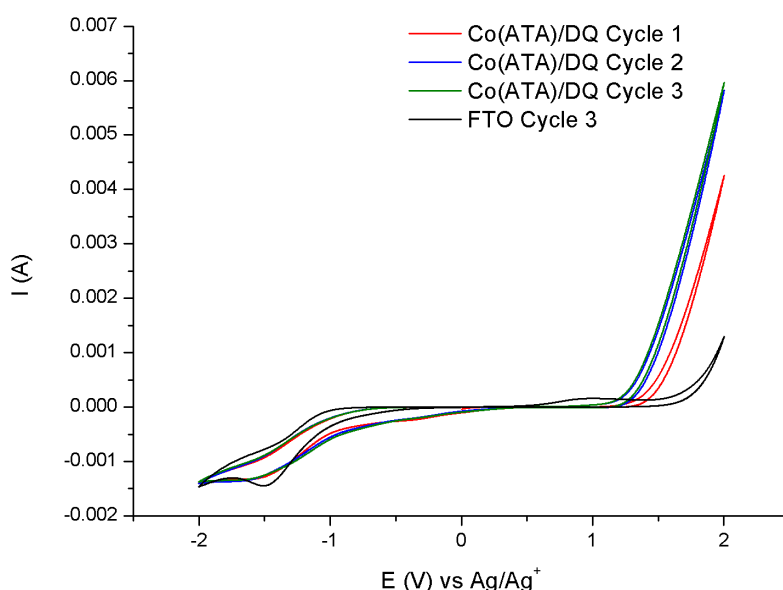


Figure 3.18: CV of Co(ATA)/DQ, Sur-18, for 3 cycles in the dark. The third cycle of a measurement on bare FTO is given as a reference (Black). This measurement is performed in an MeCN based electrolyte with a non-aqueous Ag/Ag⁺ reference electrode.

Finally the CV data for the Ti(DHTA)/DQ film, Sur-19, is shown in Figure 3.19. In the first cycle at negative potentials it behaved similar to bare FTO, when going to positive potentials again an irreversible oxidation is observed. After this the film behaved like bare FTO at positive potentials, but at negative potentials an irreversible reduction became observable. In this case it was very clear that the irreversible events were related to the MOF structure. This is because after the measurements it was observed that MOF was detached from the FTO.

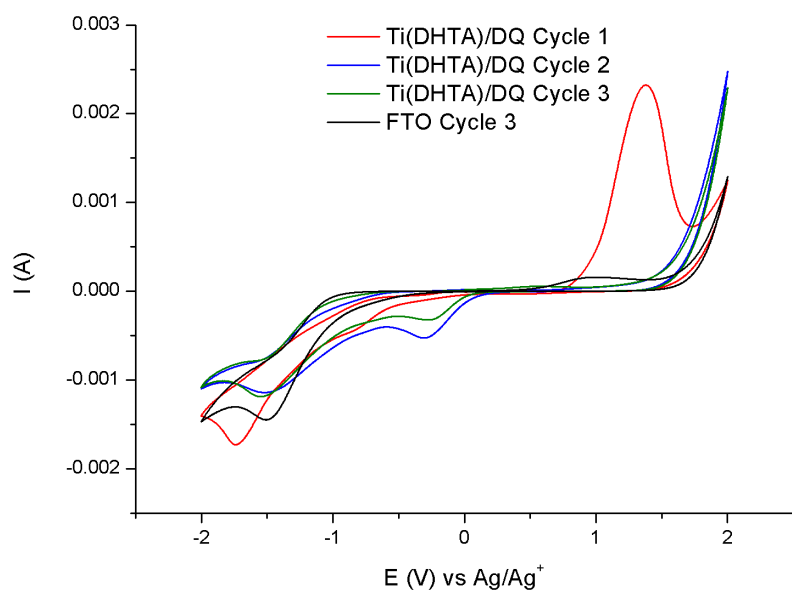


Figure 3.19: CV of Ti(DHTA)/DQ, Sur-19, for 3 cycles in the dark. The third cycle of a measurement on bare FTO is given as a reference (Black). This measurement is performed in an MeCN based electrolyte with a non-aqueous Ag/Ag⁺ reference electrode.

3.3. Summary and General discussion

In this chapter photoelectrodes of MOFs have been discussed. First the immobilization of the MOFs has been explored. The dropcasting method yielded dense films of the material but these had a very poor interaction with the substrate. However, even though these electrodes are mechanically so unstable there are studies where photoelectrochemistry was performed on such electrodes.^[65, 68] In this research we observed that electrodes prepared through the solvothermal route are mechanically far more stable and thus these were studied in more detail. From this study it is evident that films prepared through dropcasting are unsuitable for photoelectrochemical studies and that a synthesis routes like the solvothermal synthesis yields far better samples.

It has been found that the synthesis of films through the solvothermal route is far from trivial. It is very sensitive to certain factors. For example for the Co(ATA)/DQ MOFs it was found that two films, synthesized in one vessel, still possessed very different crystallinity. It was found that for the Zr(ATA) and Co(ATA) MOFs it was possible to synthesize the same structure as the reference powders. For Cu(DABCO)(ATA) and Ti(DHTA) this was not observed. In the case of Cu(DABCO)(ATA) it is unclear if this is a result of no film being formed or the film being too thin to be detected by the used characterization methods. For Ti(DHTA) UV-Vis proved that a chemically different structure was found.

When testing these films photoelectrochemically the most important observation is that the films showed no improved hydrogen evolution under illumination in the tested electrolytes. For all films a change in the oxidation region was observed compared to bare FTO, further studies are necessary to find what reaction is occurring here, a possibility would be the oxidation of water. Furthermore irreversible electrochemical events were observed to occur at most samples suggesting the MOF structure is being altered. In several cases, such as the Cu(DABCO)(ATA) and Ti(DHTA) films it is obvious since we see the film falling off the FTO. This gives indications that these irreversible events occur at the FTO-MOF interface.

Using photocatalytic MOF particles it can be tested whether this interface is the only bottleneck of these systems, or if there are more properties which have to be optimized. In Chapter 4 the sensitivity to several synthesis parameters will be explored. The MOFs will be tested in terms of photocatalysis and photophysics to confirm if the material itself is actually photoactive as is reported in literature and to understand the charge carrier dynamics.

4. Results: Photocatalytic MOFs

As explained in the previous chapter it was found that the MOFs being explored in this research do not perform well as photoelectrodes. In this chapter, the focus will be on photocatalytic properties of the same MOF structures. First in Section 4.1 the structural characterization of the different MOFs will be given were several synthesis parameters are compared. Then in Section 4.2 the results for photocatalytic tests will be given to confirm if they are indeed capable of producing hydrogen under illumination. Afterwards obtained information on the photoinduced processes by TAS will be discussed in Section 4.3 to study the charge dynamics inside these MOF structures and finally in Section 4.4 the observations will be summarized and discussed.

4.1: Structural characterization

In this section results for the different powder MOFs will be given in terms of XRD, IR, TGA and SEM. Not all samples which are described in Section 2.1.2 will be discussed here. The samples which will not be discussed either yielded no solid, as described in the methods section. MOF samples with the same structure, such as Bat-4 and Bat-24, yielded similar results unless noted otherwise. The MOFs will be described as families based on their metal node (Zr, Cu, Co or Ti).

Six types of samples have been prepared in the Zr-MOF family: Zr(ATA)/HCl (Bat-4, Bat-24) Zr(ATA)/DQ (Bat-5), Zr(DHTA)/HCl (Bat-8) Zr(DHTA)/DQ (Bat-9) and Zr(ATA)(DHTA)/HCl (Bat-14) Zr(ATA)(DHTA)/DQ (Bat-15).

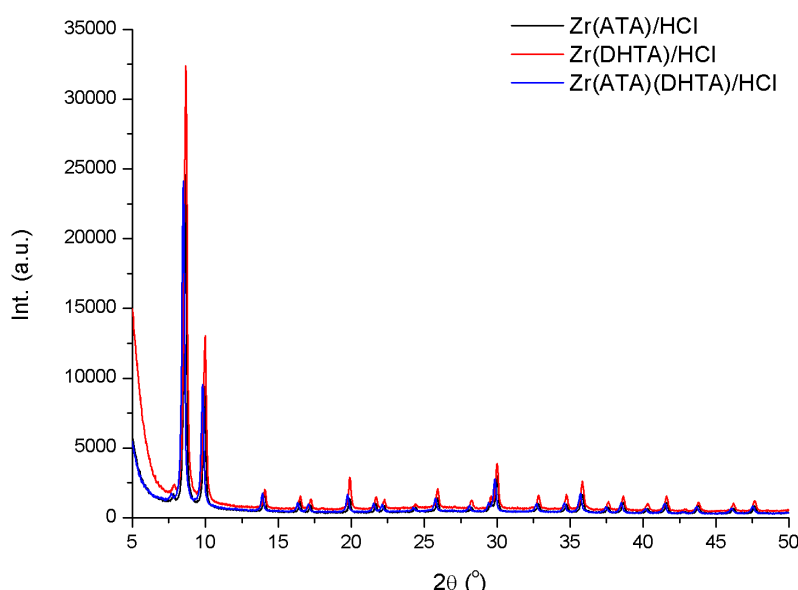


Figure 4.1: XRD data for Zr(ATA)/HCl, Bat-4 (Black), Zr(DHTA)/HCl, Bat-8 (Red) and Zr(ATA)(DHTA)/HCl, Bat-14 (Blue).

In Figure 4.1 the XRD data for Bat-4, 8 and 14 can be seen. These are all MOFs with different linkers but synthesized with the same promotor (HCl), it can be easily distinguished that the MOFs all exhibit the same crystal structure. In other words these Zr-MOFs are isoreticular. The diffractograms given in Figure 4.1 are before the activation by methanol. In Figure 4.2 Bat-4 is shown as an example that the activation procedure did not result in a collapse of the framework, nor did it collapse over time.

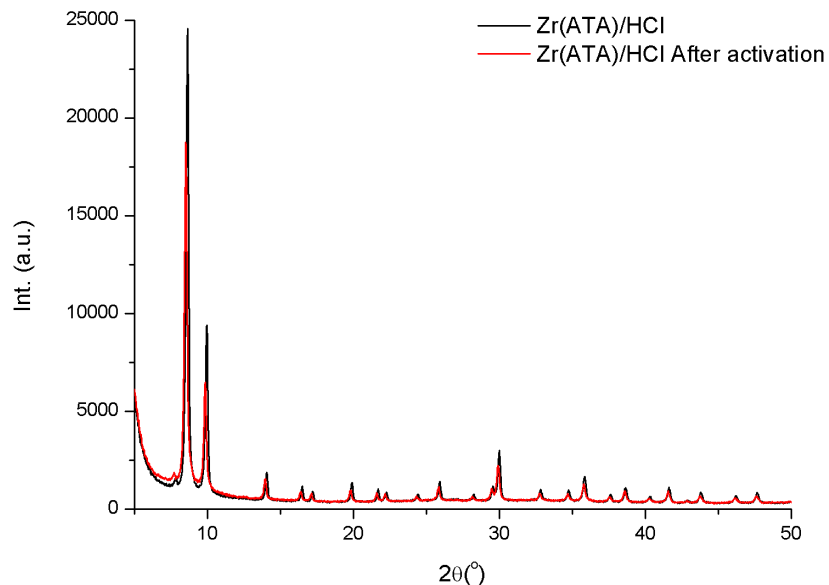


Figure 4.2: XRD data for Zr(ATA)/HCl, Bat-4 before (Black) and after (Red) activation.

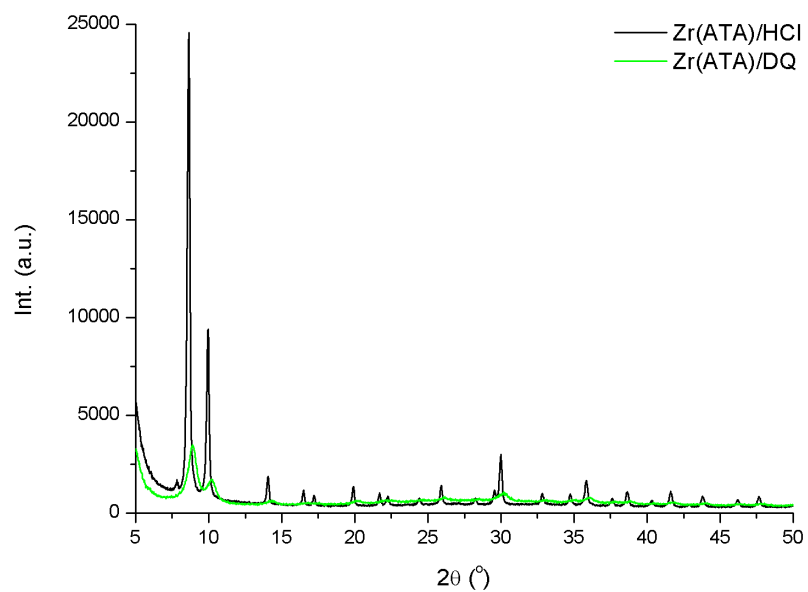


Figure 4.3: XRD data for Zr(ATA)/HCl, Bat-4 (Black) and Zr(ATA)/DQ, Bat-5 (Green).

The last relevant part that can be shown with XRD is the effect of the promotor used during the synthesis on the resulting MOF. This can be viewed in Figure 4.3. Here the Zr(ATA) MOFs Bat-4 and Bat-5 are compared, which are synthesized with HCl and DQ as promotors respectively. It is evident that for these Zr-MOFs the resulting product is much less crystalline if DQ is used as a promotor as compared to HCl. For both other Zr-MOFs similar behavior was seen when using DQ as a promotor instead of HCl.

IR spectroscopy is used to confirm the chemical character of the MOF structures. In Figure 4.4 the spectra of Bat-4, 8 and 14 are shown to compare the different linkers. It is clear that each MOF yields a different IR spectrum. Comparing Bat-4 and 8 (blue and red spectrum respectively) it is evident that the wavenumbers at which some vibrations occur have shifted. The peak at 1652 cm^{-1} is related to DMF molecules trapped in the framework, DMF is present since these spectra were obtained before activation. Bat-4 shows a peak at 1567 cm^{-1} whereas Bat-8 has a peak at 1590 cm^{-1} , these peaks relate to aromatic vibrations that have shifted since the aromatic rings have different substitution (NH_2 and OH respectively). The next peak is located at 1490 cm^{-1} and is related to aromatic C-H vibrations. The next peak for Bat-4 is 1427 cm^{-1} , for Bat-8 it is at 1454 cm^{-1} . These relate to NH_2 and OH vibrations respectively. The peak at 1397 cm^{-1} is again related to aromatic C-H vibrations. The shoulder at 1341 cm^{-1} relates to DMF. The peak at 1258 cm^{-1} for Bat-4 and the peak at 1234 cm^{-1} for Bat-8 are again related to NH_2 and OH respectively. Apart from the DMF peak at 1107 cm^{-1} all vibrations seen below 1200 cm^{-1} relate to the MOF structure and act as a fingerprint for the particular structure and can only be assigned to the interaction between the linker and metal node. The peaks at 869 cm^{-1} , 807 cm^{-1} and 789 cm^{-1} for Bat-8 and 766 cm^{-1} for Bat-4 are linker specific and depend on the substitution.

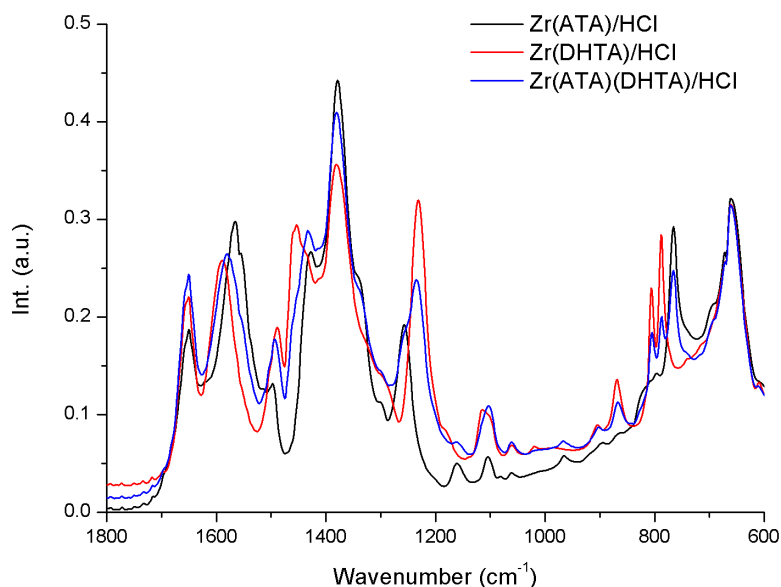


Figure 4.4: IR spectra of Zr(ATA)/HCl, Bat-4 (Black), Zr(DHTA)/HCl, Bat-8 (Red) and Zr(ATA)(DHTA)/HCl, Bat-14 (Blue).

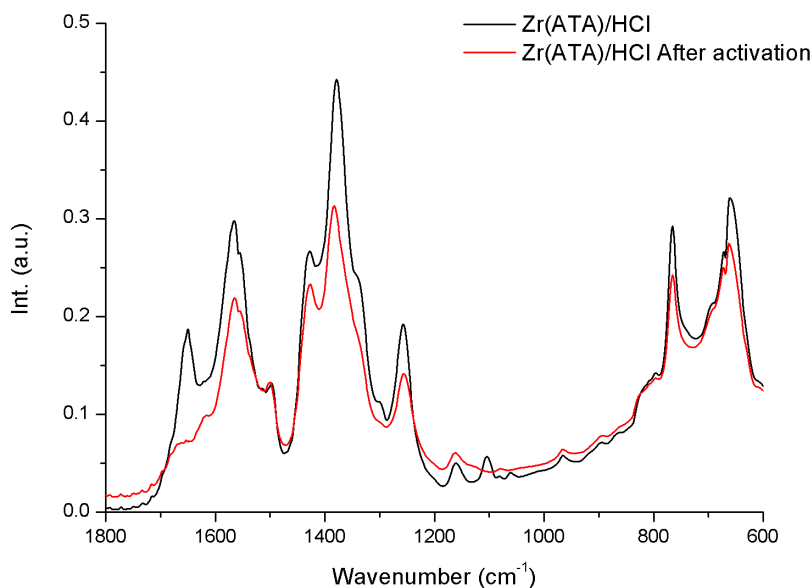


Figure 4.5: IR spectra of Zr(ATA)/HCl, Bat-4 before (Black) and after (Red) activation.

Bat-14 can be observed as being a single framework where both linkers are mixed and not a mixture of the UiO-66-NH₂ and UiO-66-(OH)₂ MOFs. This is evident from the fact that the fingerprint area is a sum of the two spectra, since both substitutions are present to interact with the Zr node, but being a mean at 1582 cm⁻¹ which relates to aromatic vibrations being influenced by their substitutions. If it was a mixture of the two MOFs the entire spectrum should have been a simple sum of both the Bat-4 and Bat-8 spectra and then there would have been a peak at 1567 cm⁻¹ with a shoulder at 1590 cm⁻¹. Finally Figure 4.5 shows that after activation of the UiO-66-NH₂ MOF the vibrations for DMF are depleted, showing that most DMF has indeed been removed from the framework.

The following data for the Zr-MOF family is TGA. The first profiles are shown in Figure 4.6. The first weight loss peak at 50 °C is considered an artifact in these measurements, since it is still present after the samples are dried at 100 °C for several hours. The origin of this artifact is not yet clear. Then at 175 °C - 250 °C there is weight loss belonging to residual DMF being removed from the pores. The weight loss after that relates to the degradation of the organic linkers. It can be seen that all three profiles are different. Bat-4 and Bat-14 both show weight loss at 425 °C which relates to the degradation of ATA. The degradation of DHTA can be seen for Bat-8 to be at 375 °C and for Bat-14 to be at 300 °C. In Figure 4.7 the TGA profiles for Bat-4 are shown before and after activation. From this can be observed that the weight loss before 300 °C disappears after the activation, meaning that the most of the residual DMF has been removed. The peak at 425 °C has not changed after activation, meaning that the framework did not destabilize.

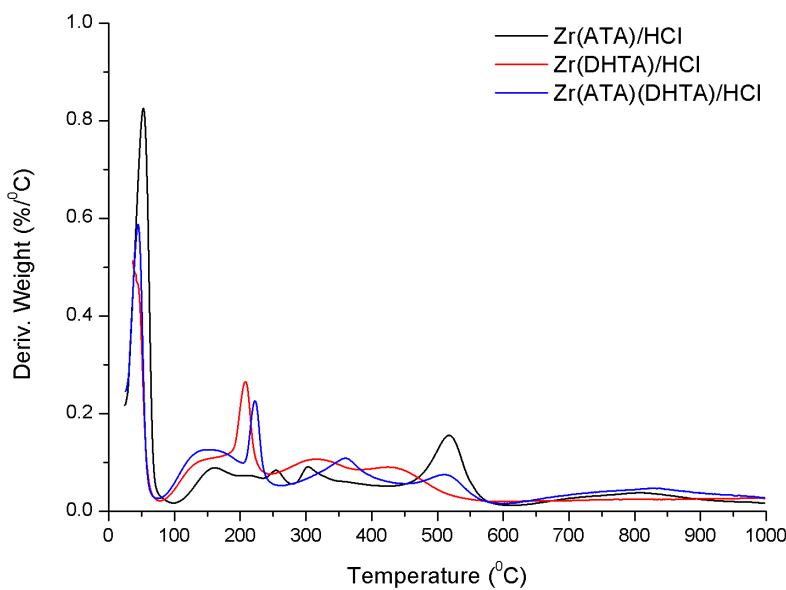


Figure 4.6: TGA profiles of Zr(ATA)/HCl, Bat-4 (Black), Zr(DHTA)/HCl, Bat-8 (Red) and Zr(ATA)(DHTA)/HCl, Bat-14 (Blue) before activation.

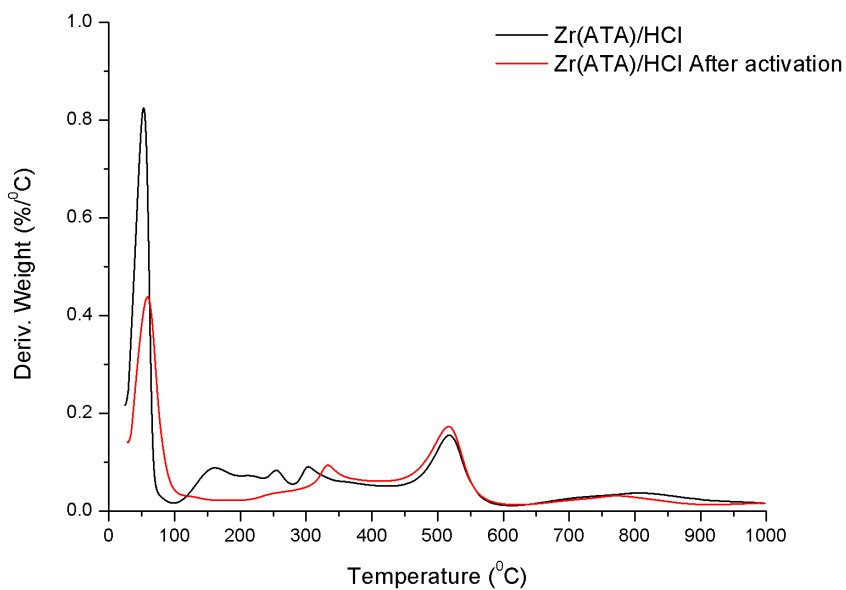


Figure 4.7: TGA profiles of Zr(ATA)/HCl, Bat-4 before (Black) and after activation (Red).

Finally SEM images have been acquired. These are given in Figure 4.8. The MOFs with different linkers (Bat-4 (NH_2), Bat-8 ($(\text{OH})_2$) and Bat-14 ($\text{NH}_2/(\text{OH})_2$) and MOFs with different promotors (Bat-4 (HCl) and Bat-5 (DQ)) are compared. Especially when comparing images A, E and G it is evident that similar particles are formed, even though the linkers are different. The only clear difference can be judged from B, F and H where it is clear that the particles of Bat-4 are about 200-300 nm in diameter,

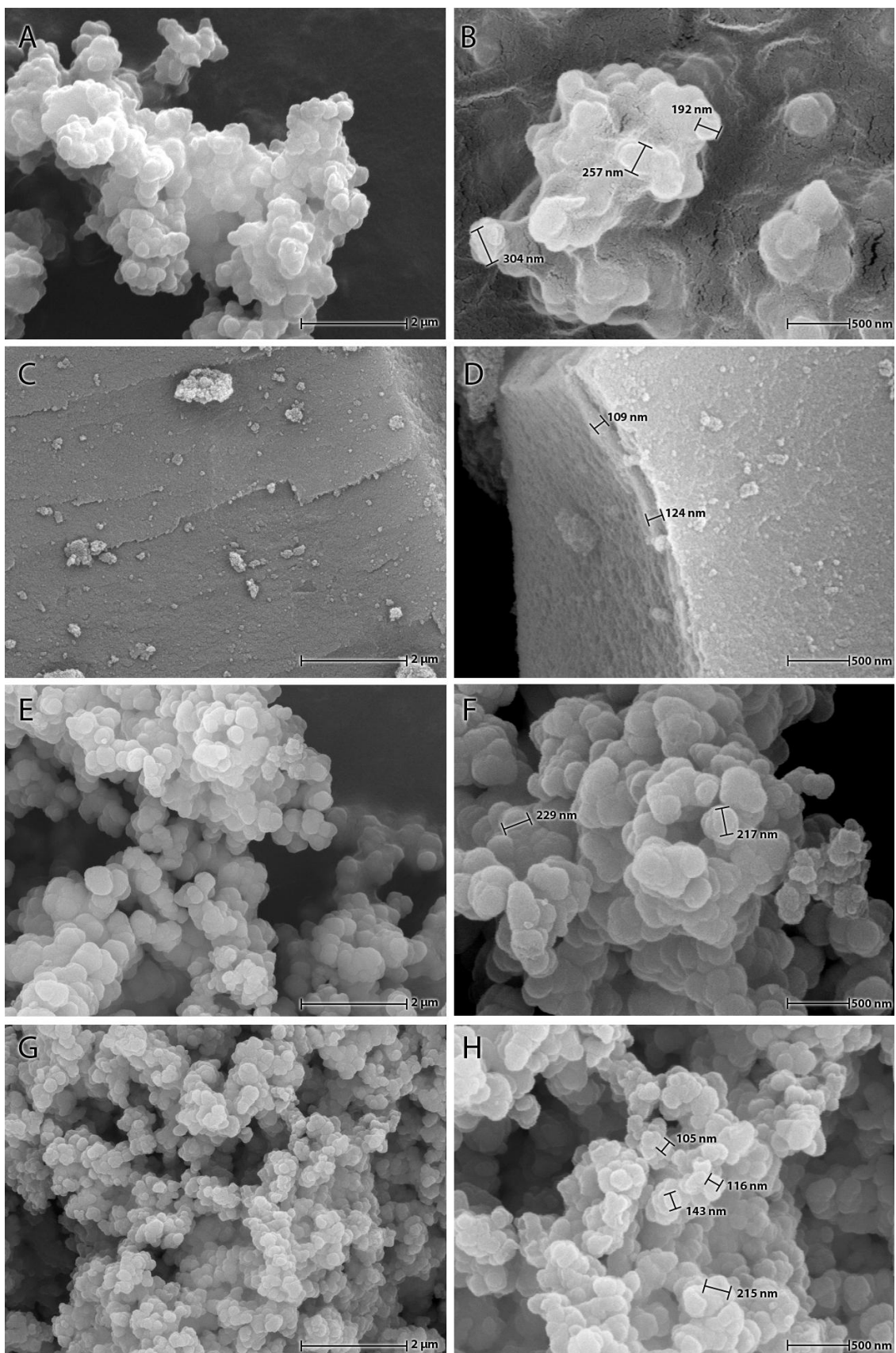


Figure 4.8: SEM topographs of the different Zr-MOFs, A & B for Zr(ATA)/HCl, Bat-4, C & D for Zr(ATA)/DQ, Bat-5, E & F for Zr(DHTA)/HCl, Bat-8 and G & H for Zr(ATA)(DHTA)/HCl, Bat-14. The images in the left column all have the same scale, as do all the images in the right column. Scale bars are indicated.

whereas Bat-8 and Bat-14 are 200-250 nm and 100-200 nm in diameter respectively. Bat-4 and Bat-5 are also compared. It is instantly clear that the topographies of these samples are very different. Bat-5 formed large particles of a few microns as opposed to the particles of Bat-4. This is related to the lack of crystallinity observed for Bat-5 by XRD.

All the results discussed for the MOFs with Zr based nodes indicate that the linkers used in this work do not affect the structure safe for particle size but do exhibit other functional groups on their organic parts. Also evident is that for the Zr-MOF family the synthesis with HCl as promotor is much more successful than the synthesis promoted by DQ. It is expected that this promotor slows down the synthesis, allowing the framework to form with less defects.

The next family of MOFs that will be discussed is those with Cu nodes. Six different syntheses have been performed. Syntheses for Cu(ATA) have been attempted with HCl as promotor (Bat-6) or DQ as promotor (Bat-7). Both yielded no solid. Since MOFs with Cu nodes form structurally different frameworks than those with Zr nodes the need of a pillar was expected. This is why the other syntheses include DABCO as a pillar linker. The other MOF syntheses that have been attempted are of Cu(DABCO)(ATA)/HCl (Bat-10) yielding no product and Cu(DABCO)(ATA)/DQ (Bat-11 and Bat-16) which did yield a solid. The syntheses of Cu(DABCO)(DHTA)/HCl (Bat-12a) and Cu(DABCO)(DHTA)/DQ (Bat-13) yielded no solid product.

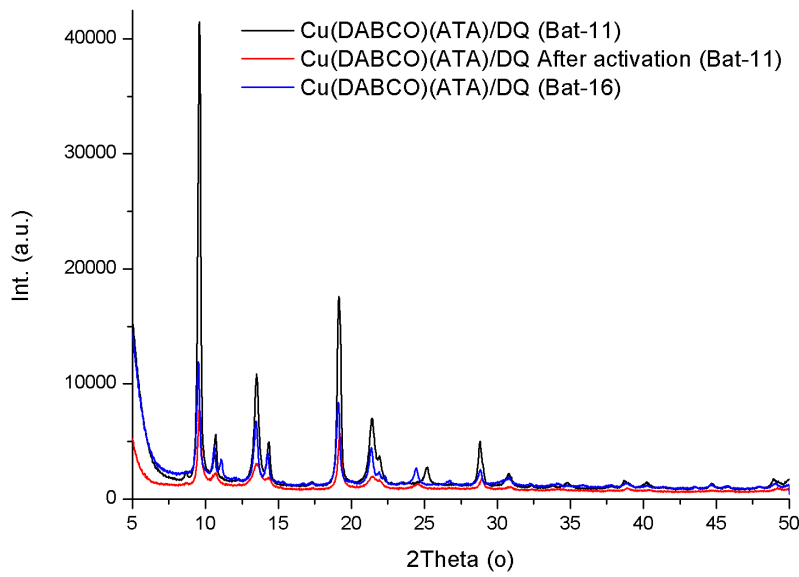


Figure 4.9: XRD data for Cu(DABCO)(ATA)/DQ MOFs, Bat-11 before (Black) and after (Red) activation and Bat-16 (Blue).

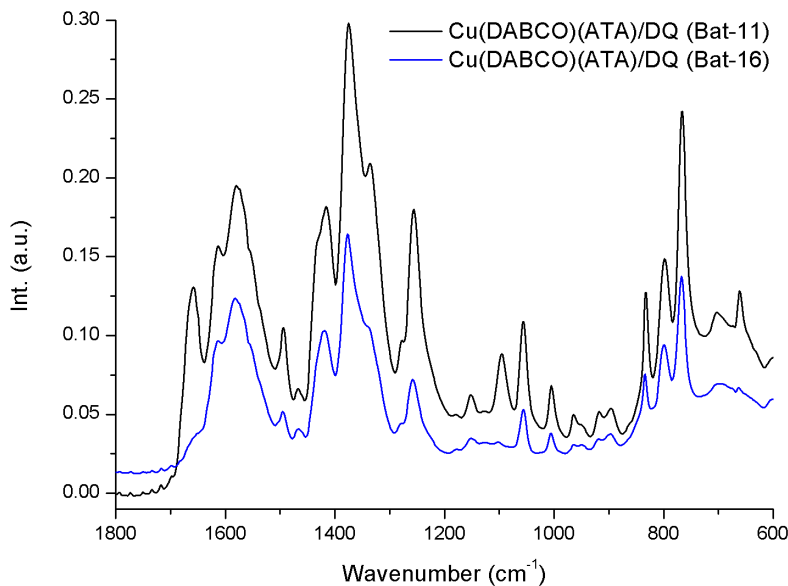


Figure 4.10: IR spectra of Cu(DABCO)(ATA)/DQ MOFs, Bat-11 before activation (Black) and Bat-16 (Blue).

In Figure 4.9 the XRD data for Bat-11 and Bat-16 is shown. For Bat-11 the diffractograms before and after activation are given and it is evident that there is loss of crystallinity in this case but the framework is still the same. Bat-16 has not been activated by suspending it in methanol because it was washed with ethanol and methanol after the filtration, as opposed to Bat-11 being washed with DMF and methanol. Figure 4.10 gives the IR spectra of Bat-11 before activation and Bat-16 proving that there is no residual DMF in Bat-16, since none of the peaks related to DMF (1652 cm^{-1} , 1341 cm^{-1} and 1107 cm^{-1}) are observed. The other vibrations relate to aromatic C-H (1615 cm^{-1} , 1581 cm^{-1} , 1494 cm^{-1} and 1375 cm^{-1}), DABCO (1467 cm^{-1} , 1336 cm^{-1} , 1153 cm^{-1} , and $1057\text{-}833 \text{ cm}^{-1}$), NH₂ (1417 cm^{-1} and 1256 cm^{-1}) and the Cu-MOF fingerprint ($800\text{-}600 \text{ cm}^{-1}$). Since in Bat-16 DMF is absent but the MOF is still crystalline it means that the loss of crystallinity observed for Bat-11 is not related to the absence of DMF but to the activation protocol.

Figure 4.11 gives the TGA profile for Bat-11. The initial weight loss is considered an artifact, the loss at $140 \text{ }^\circ\text{C}$ is related to residual DMF since Bat-11 was not yet activated at that time. Then above $200 \text{ }^\circ\text{C}$ the framework becomes unstable. Finally SEM topographs are given in Figure 4.12. A sheet-like structure can be observed in these. This can be explained by the expected structure of the MOF. This structure places the ATA linkers on the paddle wheel copper nodes forming sheets. These sheets are then linked together by the DABCO pillar which coordinates on the remaining free sites of the copper nodes. This structure is presented in Figure 1.12.

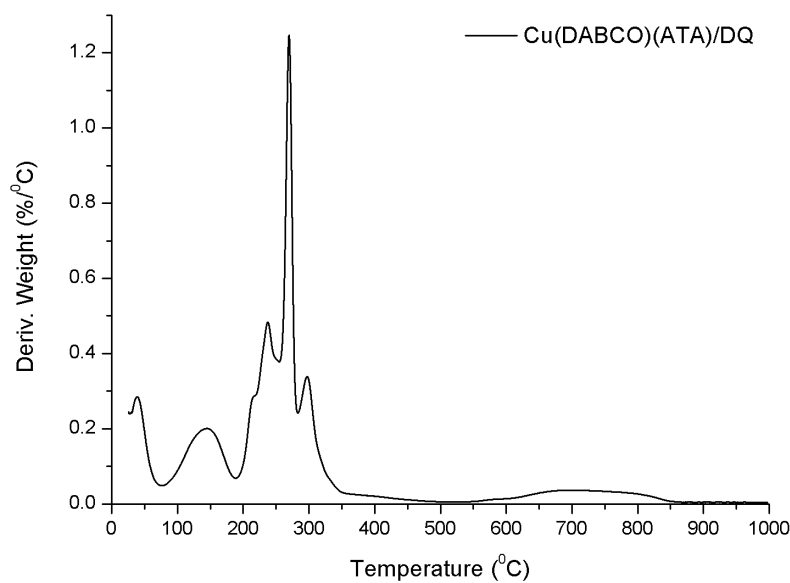


Figure 4.11: TGA profile of Cu(DABCO)(ATA)/DQ, Bat-11.
The weight loss at 50 °C is considered an artefact.

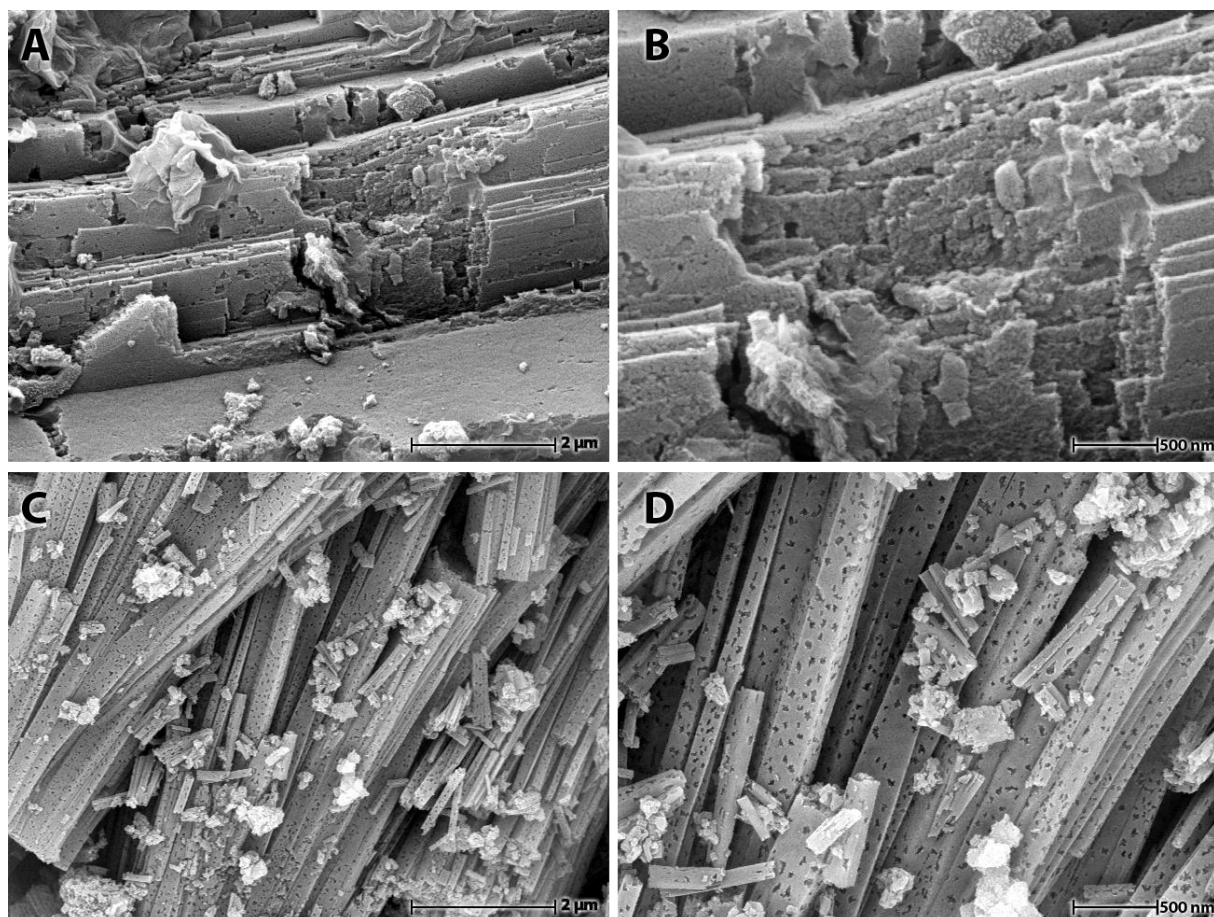


Figure 4.12: SEM topographs of the Cu(DABCO)(ATA)/DQ MOFs, Bat-11 (A and B) and Bat-16 (C and D). Scale bars are indicated in the images.

Since Co has a charge of +2 like the Cu in the studied Co based MOFs it was expected to behave similarly to the Cu MOFs. This is why the syntheses of Co(ATA)/DQ (Bat-17) and Co(DABCO)(ATA) (Bat-18) have been performed. Both yielded a solid product and both will be discussed.

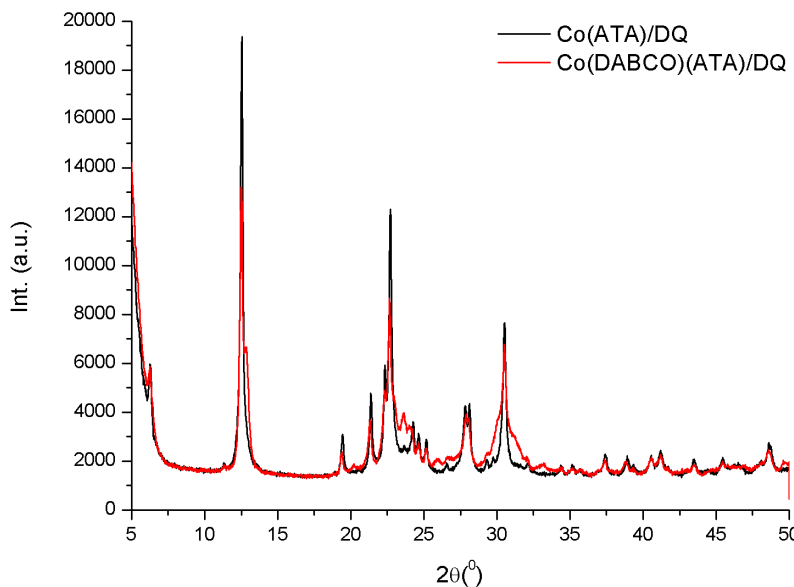


Figure 4.13: XRD data for Co(ATA)/DQ, Bat-17 (Black) and Co(DABCO)(ATA)/DQ, Bat-18 (Red).

In Figure 4.13 the XRD patterns for both Co MOFs are given. In this figure it is evident that the general structure of both samples is similar. However for the sample with DABCO the diffractogram show broader peaks, meaning the structure is less homogeneous. Following this IR has been used to check if DABCO was actually present in the framework of Bat-18. The IR spectra can be seen in Figure 4.14. It is evident that the spectra for both samples are the same and that no separate DABCO peaks are observed in Bat-18. In short, aromatic vibrations are found at 1620 cm^{-1} , 1594 cm^{-1} , 1545 cm^{-1} , 1538 cm^{-1} , 1520 cm^{-1} , 1502 cm^{-1} and 1389 cm^{-1} . Vibrations related to the NH_2 functionality are seen at 1430 cm^{-1} , 1314 cm^{-1} and 1243 cm^{-1} . The peaks below 1159 cm^{-1} are mostly related fingerprint vibrations of the framework. These results indicate that DABCO is not necessary for the framework to form and that adding it to the synthesis only interferes with the formation of the MOF.

IR also confirms the lack of residual DMF, meaning there are no peaks around 1650 cm^{-1} and 1100 cm^{-1} . TGA confirms there is almost no DMF left in the samples, which can be seen in Figure 4.15. Only a small weight loss around $150\text{ }^{\circ}\text{C}$ shows there is a tiny amount of solvent left. Then the framework clearly destabilizes at $400\text{ }^{\circ}\text{C}$. SEM topographs can be found in Figure 4.16 for Bat-17 and Bat-18. It can be seen that this material forms sheet-like particles of several microns long in two dimensions while remaining very thin, few to about a hundred nanometers, in the third dimension.

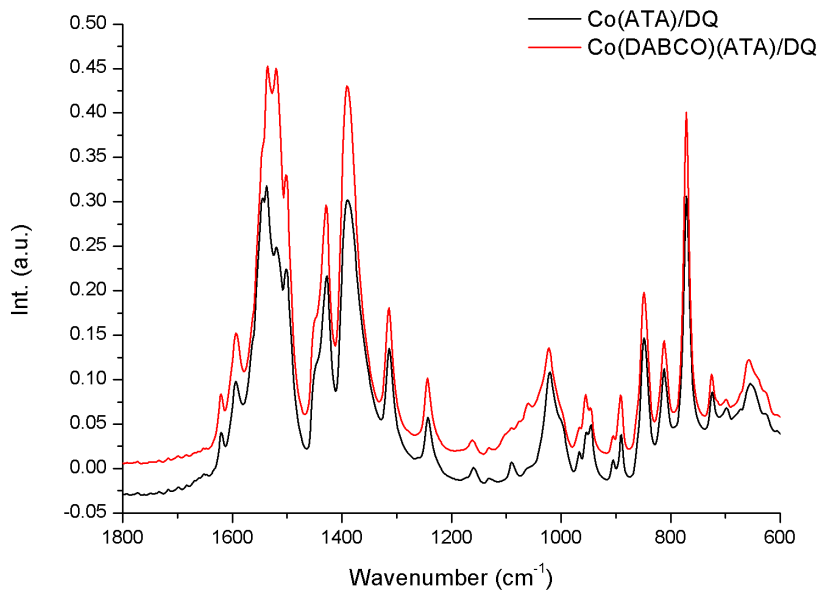


Figure 4.14: IR spectra of Co(ATA)/DQ, Bat-17 (Black) and Co(DABCO)(ATA)/DQ, Bat-18 (Red).

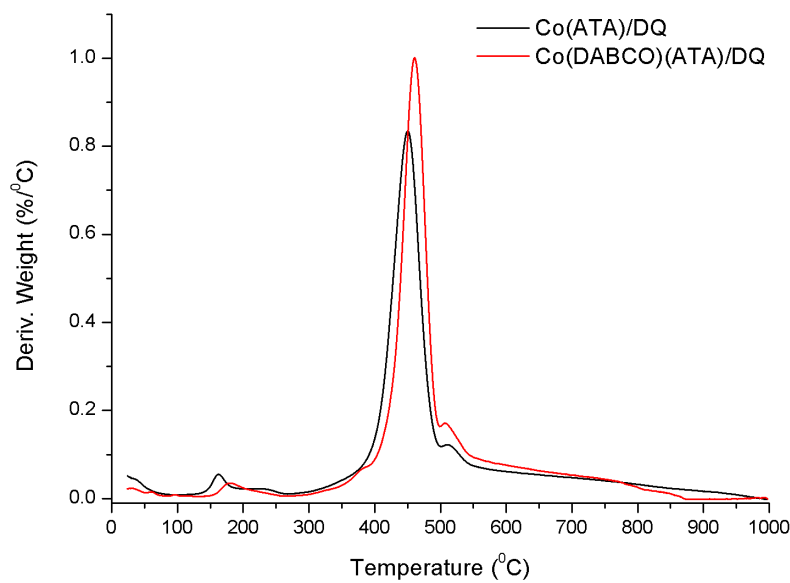


Figure 4.15: TGA profiles for both Co(ATA)/DQ, Bat-17 (Black) and Co(DABCO)(ATA)/DQ, Bat-18 (Red).

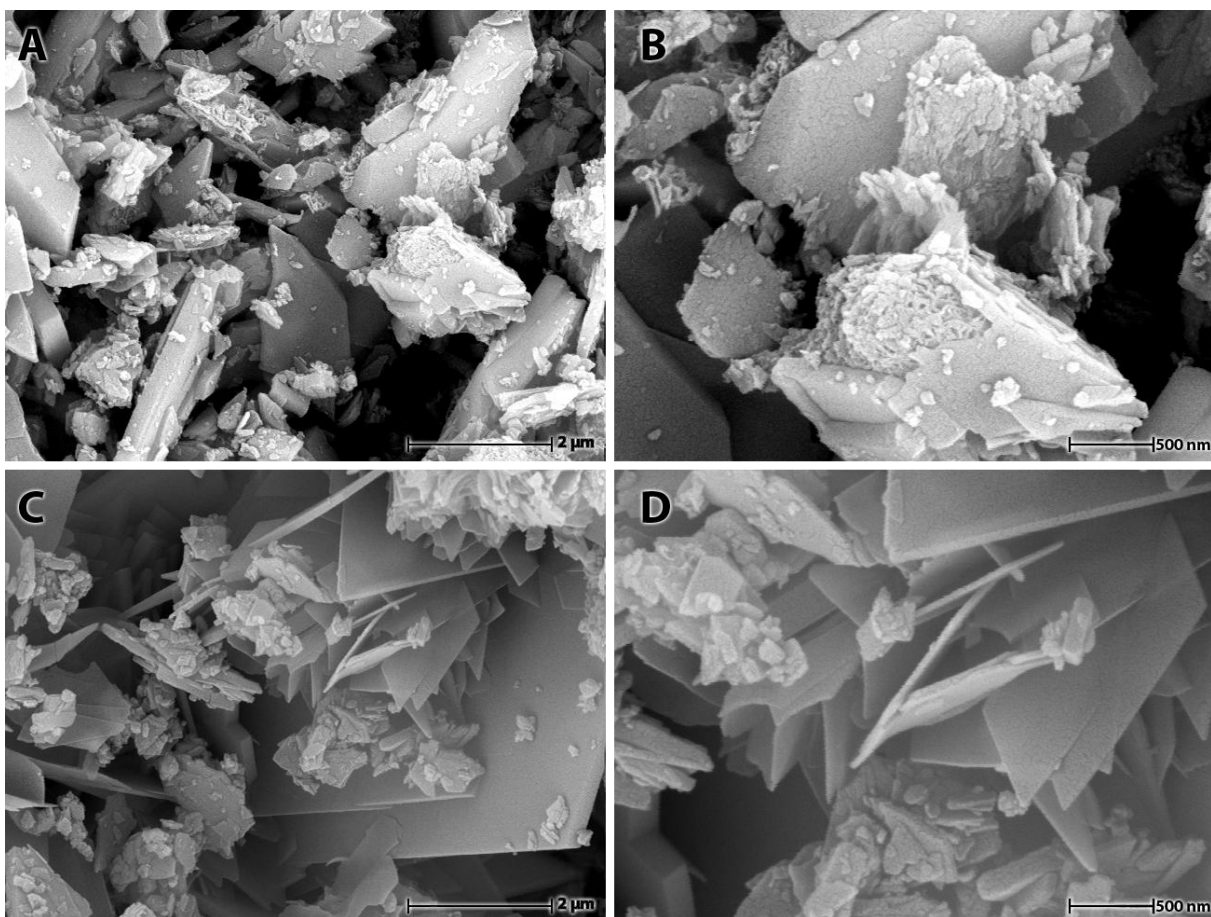


Figure 4.16: SEM topographs of Co(ATA)/DQ, Bat-17 (A and B) and Co(DABCO)(ATA)/DQ, Bat-18 (C and D). Scale bars are indicated.

The last family of MOFs to be discussed is based on Ti nodes. These MOFs have been synthesized with ATA or DHTA. The following MOFs have been prepared with ATA as linker: Ti(ATA)/DQ (Bat-19), Ti(ATA)/HCl (Bat-20) and Ti(ATA)/MeOH (Bat-26 and Bat-27) where Bat-27 has been synthesized for 72 hours instead of 24 hours. The MOFs with DHTA are as follows: Ti(DHTA)/DQ (Bat-21 and Bat-25), Ti(DHTA)/HCl (Bat-22), Ti(DHTA)/AcOOH (Bat-23) and Ti(DHTA)/MeOH (Bat-28 and Bat-29) where Bat-29 has been synthesized for 72 hours instead of 24 hours.

XRD has been performed on all samples. In Figure 4.17 the diffractograms of MIL-125(Ti)-NH₂ can be seen. It is evident that the samples promoted by DQ or HCl during the synthesis yielded product with no evident crystallinity. The syntheses promoted by methanol yielded quite crystalline products however. Comparing Bat-26 and Bat-27-F it can be seen that the length of the synthesis has no significant influence at least after 24 hours. It does seem however that the crystalline particles are rather small, meaning that the filtrate had to be dried to obtain the crystalline product. This is evident by the fact that Bat-27 is much less crystalline than Bat-27-F.

In Figure 4.18 the diffractograms for MIL-125(Ti)-(OH)₂ are given. Here it can be seen that promotion by acetic acid yields no crystalline product. Promotion by HCl and DQ can yield somewhat crystalline products but as Bat-25 shows it is not always the

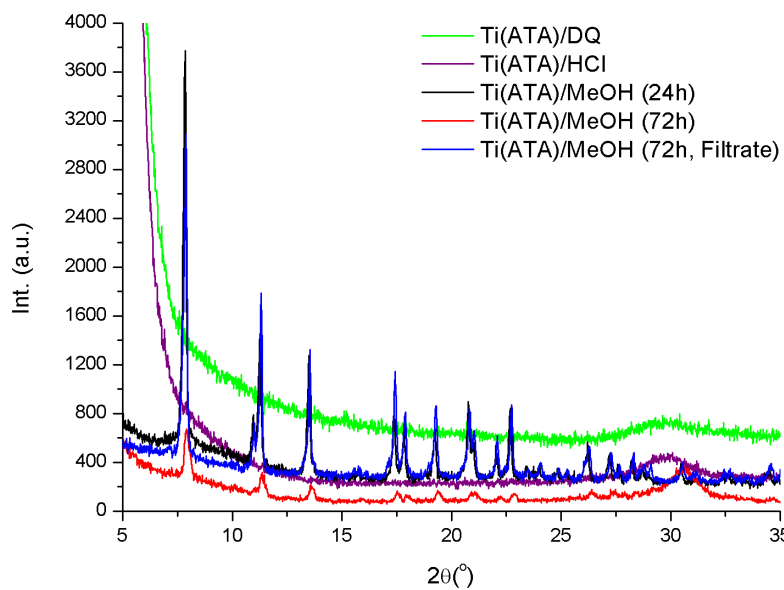


Figure 4.17: XRD data of Ti(ATA)/DQ (Bat-19, Green), Ti(ATA)/HCl (Bat-20, Purple) and Ti(ATA)/MeOH synthesized for 24 hours (Bat-26, Black) and 72 hours (Bat-27, Red) and the dried filtrate of the latter (Bat-27-F, Blue).

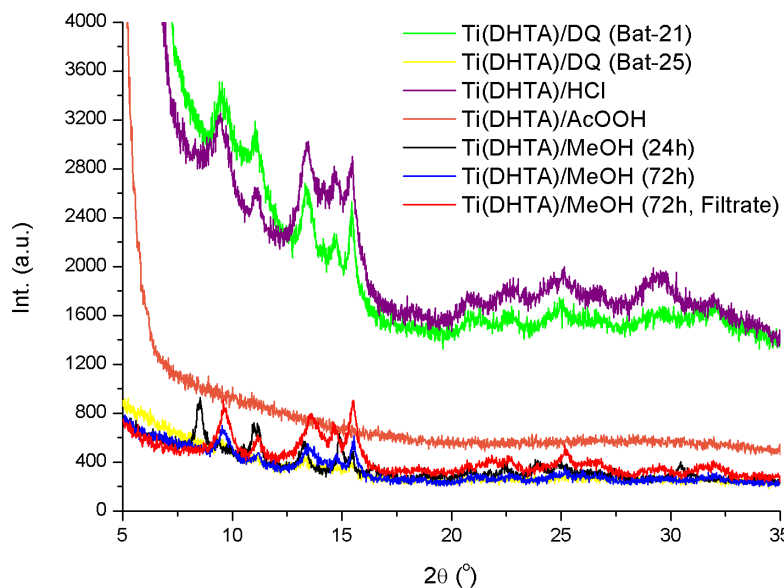


Figure 4.18: XRD data of Ti(DHTA)/DQ (Bat-21, Green and Bat-25, Yellow), Ti(DHTA)/HCl (Bat-22, Purple), Ti(DHTA)/AcOOH (Bat-23, Orange) and Ti(DHTA)/MeOH synthesized for 24 hours (Bat-28, Black) and for 72 hours (Bat-29, Blue) and the dried filtrate of the latter (Bat-29-F, Red).

case for DQ promotion. Promotion by methanol improves the crystallinity of the solids somewhat and it seems maintaining the synthesis for 72 hours does improve the quality a bit as opposed to the synthesis of 24 hours. Here as well it seems the

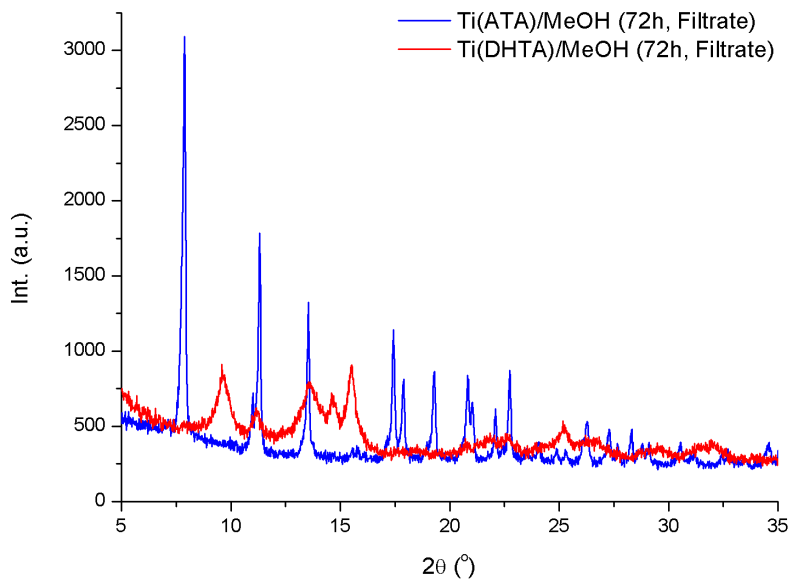


Figure 4.19: XRD data of the dried filtrates of Ti(ATA)/MeOH (Bat-27-F, Blue) and Ti(DHTA)/MeOH (Bat-29-F, Red) synthesized for 72 hours.

filtrate contained the better particles. Finally in Figure 4.19 the two MOFs are compared to see if they are isoreticular. From the image it is clear the MOFs are structurally different.

In Figure 4.20 the IR spectra for the filtrates are compared. These patterns compare to those of Zr(ATA) and Zr(DHTA) MOFs. Most important are the NH_2 peaks at 1423 cm^{-1} and 1256 cm^{-1} and the peak at 768 cm^{-1} related to MOFs with ATA as linker and

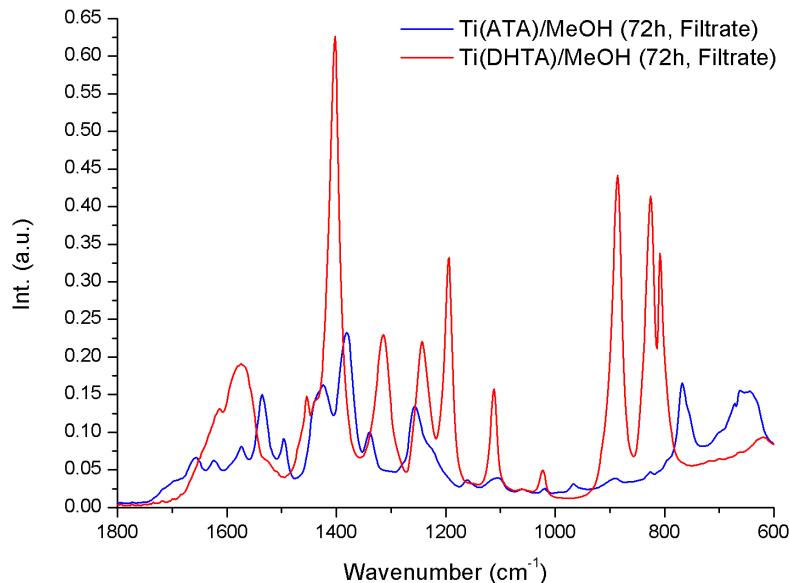


Figure 4.20: IR spectra of the Ti-MOFs Ti(ATA)/MeOH, Bat-27-F (Blue) and Ti(DHTA)/MeOH, Bat-29-F (Red).

the OH peaks at 1454 cm^{-1} and 1242 cm^{-1} and the peaks at 887 cm^{-1} , 826 cm^{-1} and 808 cm^{-1} characteristic for these MOFs with the DHTA linker. Several DMF peaks can also be seen since these materials had not been washed or activated yet.

In the TGA profiles, in Figure 4.21, this presence of DMF can be seen as well. This is why several MOFs have a weight loss peak at $100\text{-}150\text{ }^{\circ}\text{C}$, the MOFs that have been washed before do not show this peak (Bat-22, Bat-29). The next obvious observation is that the TGA profiles of Ti(ATA) and Ti(DHTA) are clearly different, which makes sense since the stability of the organic linker is different. The last observation that can be made is that Ti(DHTA) promoted by MeOH is thermally a bit more stable, about $30\text{ }^{\circ}\text{C}$, than this MOF promoted by HCl.

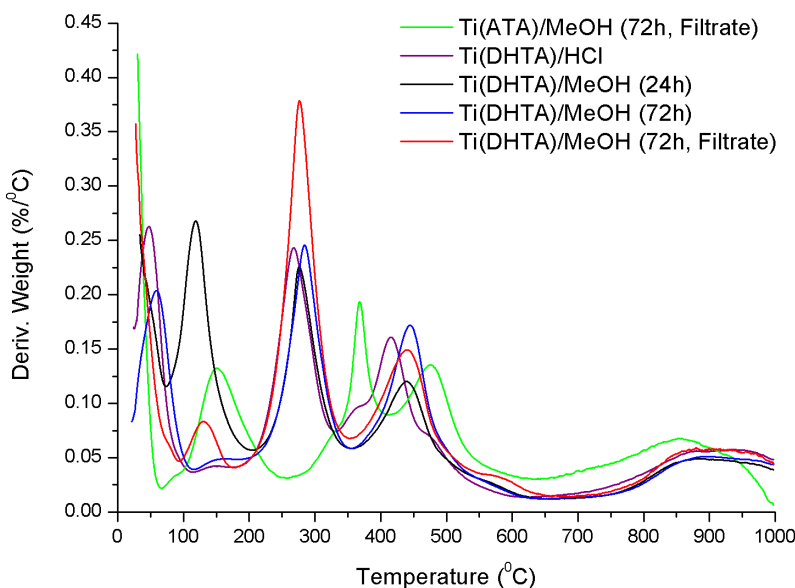


Figure 4.21: TGA profiles for the Ti-MOFs Ti(ATA)/MeOH, Bat-27-F (Green), Ti(DHTA)/HCl, Bat-22 (Purple), Ti(DHTA)/MeOH, Bat-28 (Black), Ti(DHTA)/MeOH, Bat-29 (Blue) and Ti(DHTA)/MeOH, Bat-29-F (Red).

Finally the morphology has been checked of the Ti-MOFs. In Figure 4.22 the first six images A to F show Ti(ATA) MOFs. Ti(ATA)/HCl and Ti(ATA)/DQ alike yielded morphologies as shown in A and B yielding large micron sized particles which are clearly amorphous. When Ti(ATA) was promoted by MeOH however cylindrical particles of about 250 nm are formed. Also evident is that when comparing the samples synthesized for 24 hours and 72 hours is that the particles formed at longer synthesis times look like they are bigger and the size distribution is smaller. Finally Ti(DHTA) MOFs formed morphologies as shown in G and H. This morphology was found for any of the three tested promoters and is similar to the morphology found when this MOF is immobilized.

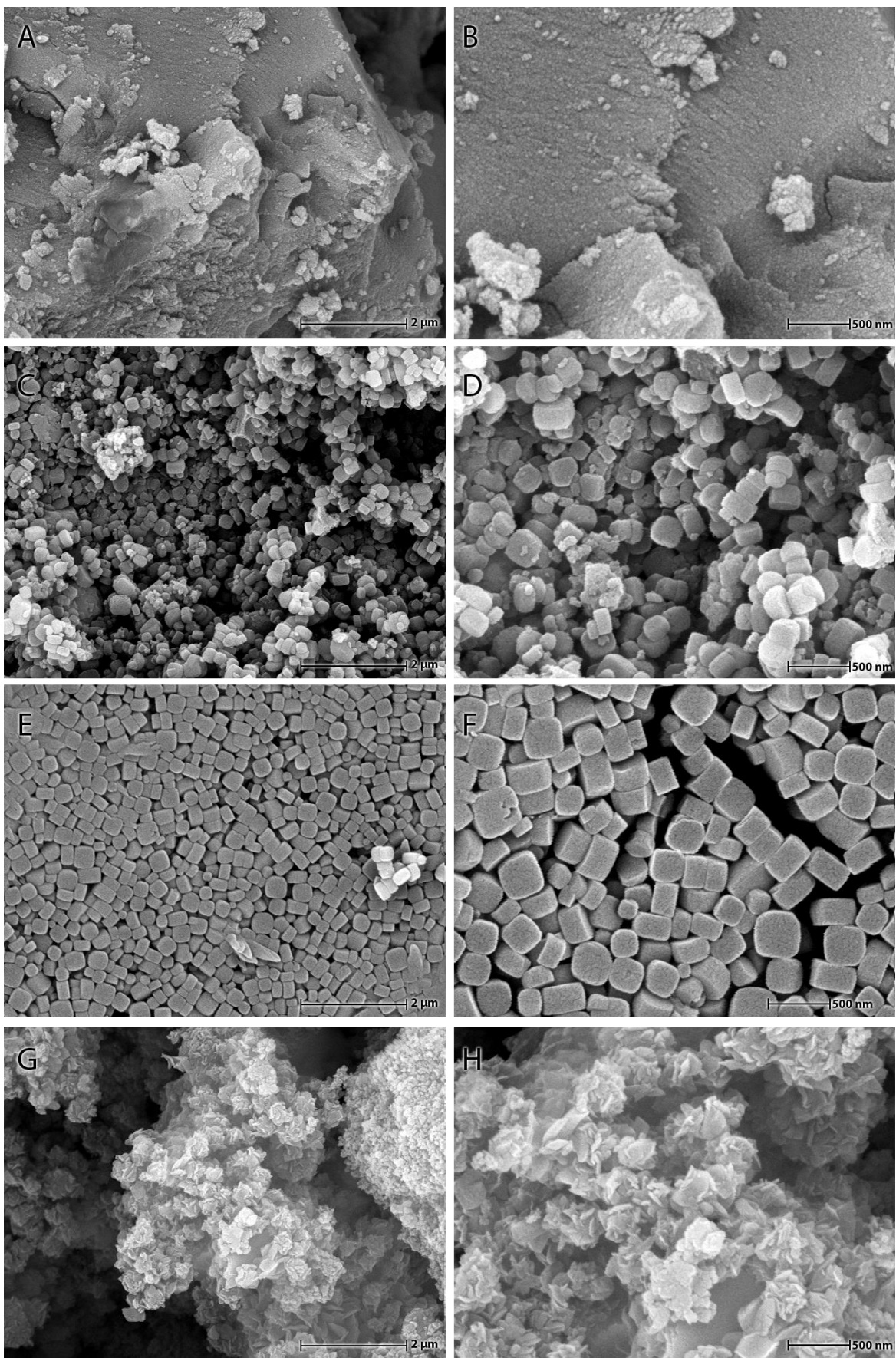


Figure 4.22: SEM topographs of the different Ti-MOFs, A & B for Ti(ATa)/HCl, Bat-20, C & D for Ti(ATa)/MeOH (24h), Bat-26, E & F for Ti(ATa)/MeOH (72h, Filtrate), Bat-27-F and G & H for Ti(DHTa)/MeOH (24h), Bat-28.

4.2: Photocatalytic tests

To check if the MOFs are indeed photocatalytically active several tests have been performed in Eindhoven on the Zr(ATA)/HCl MOF, Bat-4, the Zr(ATA)/DQ MOF, Bat-5, The Zr(DHTA)/HCl and Zr(DHTA)/DQ MOFs, Bat-8 and Bat-9 and finally the Cu(DABCO)(ATA) MOF, Bat-11.

In Figure 4.23 the hydrogen evolution over time for several mixtures are depicted. The Zr(ATA)/DQ MOF, Bat-9 in a phosphate buffer with TEA shows a steady hydrogen evolution. At a first glance this indicates the MOF is indeed active, however a blank test with just a TEA containing phosphate buffer showed similar hydrogen evolution. Blank tests with just the phosphate buffer or an empty vessel show a very low steady hydrogen signal which is ascribed to a small leak in the system. This is plausible since there is a hydrogen line attached to the system which is used for calibration.

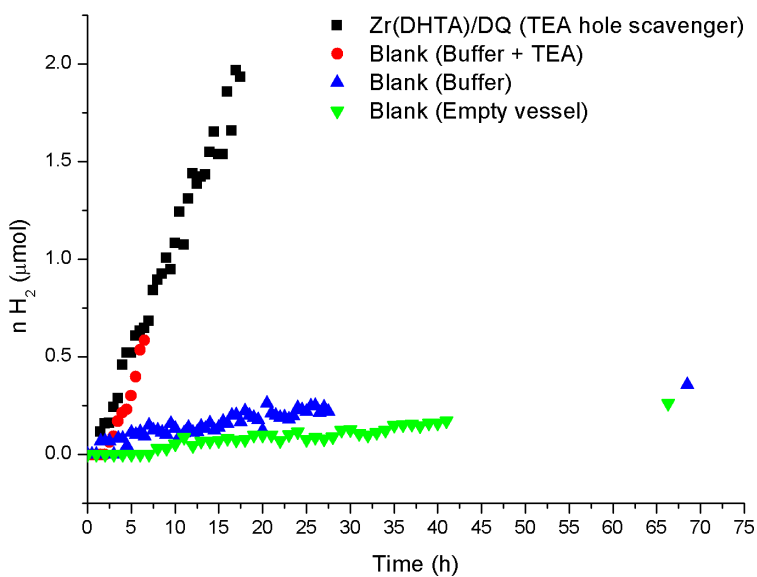


Figure 4.23: Hydrogen evolution over time for several mixtures. Shown are Zr(ATA)/DQ (Bat-9) with TEA in a phosphate buffer (Black), TEA in a phosphate buffer (Red), the phosphate buffer (Blue) and of the empty vessel (Green).

Since the system with the buffer containing TEA is not entirely stable, observing hydrogen evolution without any added MOF, tests have been performed where TEA is replaced by methanol. Figure 4.24 shows the hydrogen evolution of this mixture with the Zr(ATA)/DQ MOF, Bat-9 present. As can be seen in the plot there is no hydrogen production by the MOF. All the other MOFs mentioned earlier in this section that have been tested showed no hydrogen production either.

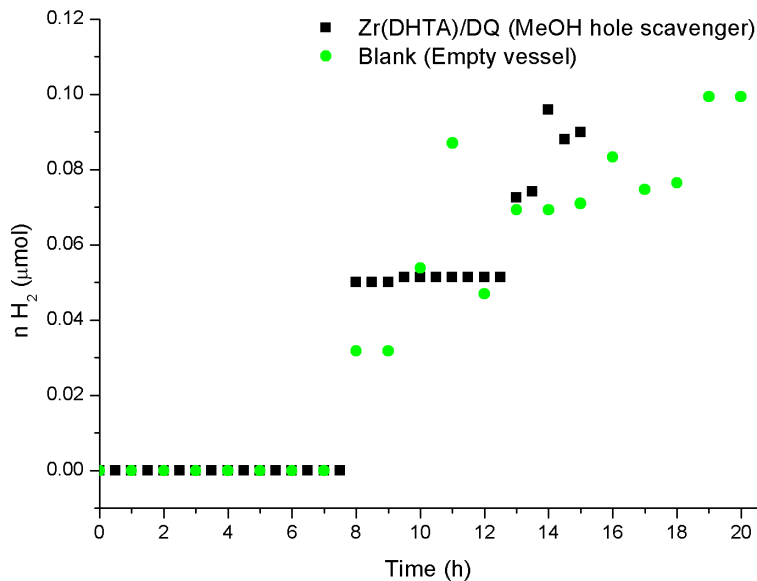


Figure 4.24: Hydrogen evolution over time for Zr(ATa)/DQ (Bat-9) in a mixture of water en methanol (Black) and the empty vessel (Green).

These results indicate that there is no hydrogen production using these MOFs as catalysts, agreeing with the lack of activity observed for the photoelectrodes. This means that there is at least one bottleneck related to the charge carriers. In the next section the tests to find this bottleneck will be discussed.

4.3: Photophysical characterization

The photocatalytic and photoelectrochemical tests indicate the obtained MOFs are not catalytically active as opposed to previous reports. To find the reason the photoinduced processes were studied in more detail. In this section first tests will be given showing if the MOFs absorb light from the visible region of the spectrum. For this results from UV-Vis spectroscopy in the visible region will be discussed. Transient absorption spectroscopy results will be used to illustrate the charge carrier dynamics after light absorption. Of each MOF representatives will be discussed and the MOFs will be discussed per family (Zr, Cu, Co or Ti), first for UV-Vis, then for TAS.

For the Zr-based MOFs, the MOFs that will be discussed are Zr(ATa)/HCl (Bat-4, Bat-24), Zr(ATa)/DQ (Bat-5), Zr(DHTA)/HCl (Bat-8), Zr(DHTA)/DQ (Bat-9), Zr(ATa)(DHTA)/HCl (Bat-14) and Zr(ATa)(DHTA)/DQ (Bat-15). In Figure 4.25 the UV-Vis data for these MOFs can be seen. Two clear trends are evident from these spectra. First of all is that the DHTA linker broadens the absorption band more into the visible region, this is evident from Bat-8 and 9 absorbing up to higher wavelengths than the other MOFs. The other trend that is evident is that the MOFs

synthesized while being promoted by DQ absorb in a wider region than those promoted by HCl.

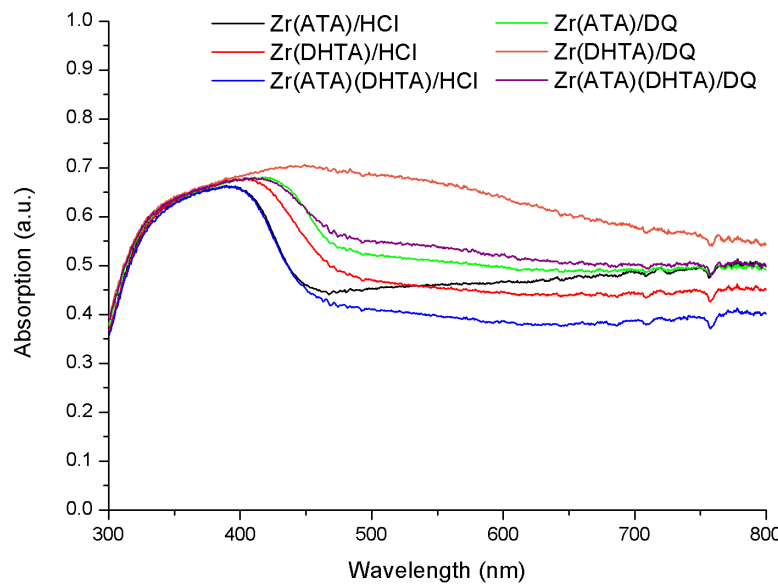


Figure 4.25: UV-Vis data of the UiO-66 MOFs. The MOFs shown are Zr(ATA)/HCl, Bat-4 (Black), Zr(ATA)/DQ, Bat-5 (Green), Zr(DHTA)/HCl, Bat-8 (Red), Zr(DHTA)/DQ, Bat-9 (Orange), Zr(ATA)(DHTA)/HCl, Bat-14 (Blue) and Zr(ATA)(DHTA)/DQ, Bat-15 (Purple). All data is from the MOFs after activation.

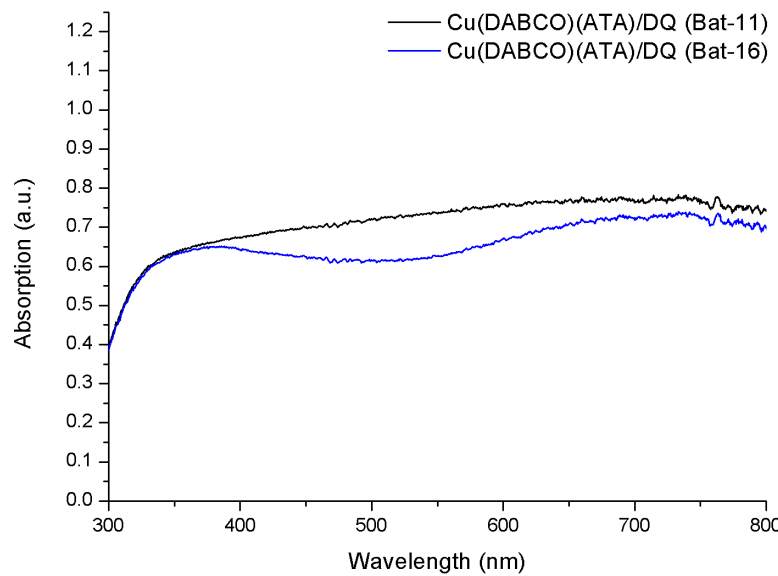


Figure 4.26: UV-Vis data of the Cu(DABCO)(ATA)/DQ MOFs. The MOFs shown are Bat-11 (Black) and Bat-16 (Blue). The data for Bat-11 is after activation.

The UV-Vis data for the Cu-MOFs and Co-MOFs is shown in Figure 4.26 and Figure 4.27 respectively. The band at 300-450 nm related to the ATA linker is again seen with the same intensity as for the UiO-66 MOFs. However the absorption at higher wavelengths seems to be higher than for the Zr-MOFs, which is also evident

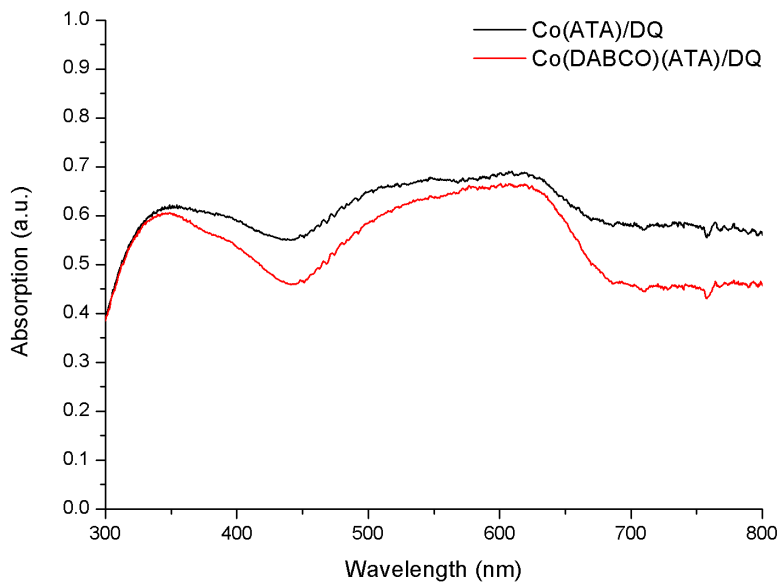


Figure 4.27: UV-Vis data of the Co-MOFs. The MOFs shown are Co(ATA)/DQ (Bat-17, Black) and Co(DABCO)(ATA)/DQ (Bat-18, Red).

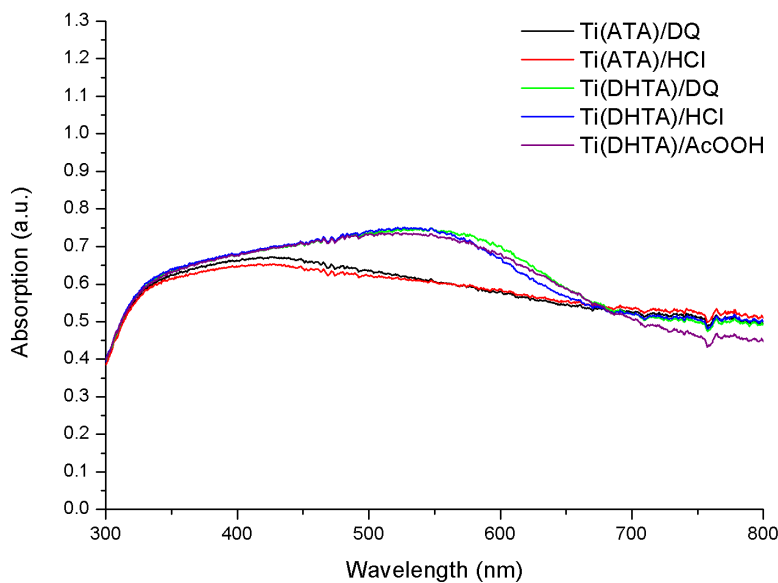


Figure 4.28: UV-Vis data of the Ti-MOFs. The MOFs shown are Ti(ATA)/DQ and Ti(ATA)/HCl (Bat-19 and Bat-20, Black and Red respectively) and Ti(DHTA)/DQ, Ti(DHTA)/HCl and Ti(DHTA)/AcOOH (Bat-21, Bat-22, and Bat-23, Green, Blue and Purple respectively).

from the dark green color the Cu-MOFs exhibit and the blue-purple color of the Co-MOFs. The absorption profile is different for both Cu-MOFs even though these were similarly synthesized. The difference is that Bat-11 had to be activated, whereas Bat-16 did not. As was explained in Section 4.1 this activation resulted in a loss of crystallinity. The Co-MOFs also show two clear absorption bands at 510 nm and 620 nm. It also seems that regardless of the presence of DABCO during the synthesis the UV-Vis absorption profile is similar.

In Figure 4.28 the UV-Vis absorption data for the Ti-MOFs is shown. Again there is the band at 300-450 nm related to the linkers. Then for the Ti(DHTA) MOFs there is a clear second band at 540 nm which is absent in the Ti(ATA) MOFs. This difference in absorption profile agrees with the fact the MOFs with DHTA as linker are red, whereas the ones with ATA as linker are yellow. For the MOFs promoted by methanol no UV-Vis absorption spectra have been obtained yet.

TAS is used to investigate the dynamics of electrons excited after the absorptions observed in the UV-Vis measurements. Since in all cases the linkers absorb at 300-450 nm the excitation wavelength of 355 nm was opted. No loss of light absorption was observed during the tests, suggesting there is no photodegradation. Signals resulting from light contamination at 532 nm and 710 nm have been omitted for clarity.

For the Zr-MOF family Figure 4.29 gives the data for Bat-8, Figure 4.30 shows the data for Bat-9 and Figure 4.31 and Figure 4.32 give the data for Bat-14 at shorter and longer timescales respectively. Figure 4.29A shows that Bat-8 has two transient bands, at 554 nm and 465 nm. Also observed is a bleaching effect at 608 nm. When analyzing the kinetic curves at these wavelengths, seen in Figure 4.29B we find fits with one exponential component in the decay. This component tells us that the lifetime of the transient state that is observed is about 4.4-4.7 ns. Since the bleach is restored in a similar timescale, visible in Figure 4.29B, the loss of the transient state can be explained by the recovery of the ground state.

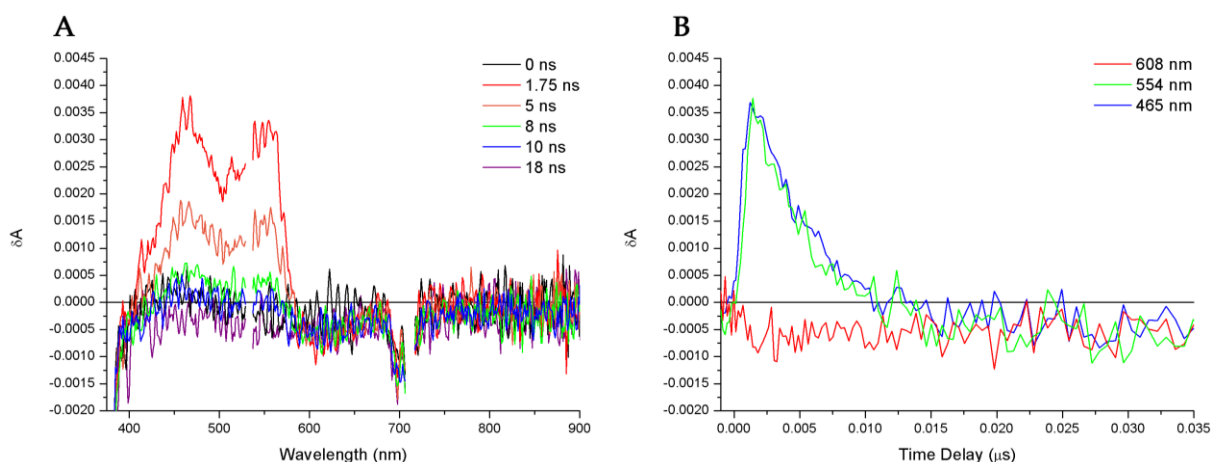


Figure 4.29: A) Transient absorption spectra for Zr(DHTA)/HCl, Bat-8. B) Transient absorption decay traces probed at 608 nm, 554 nm and 465 nm. The pump laser beam power was 0.972 mW and the measurement was performed for 22min45s.

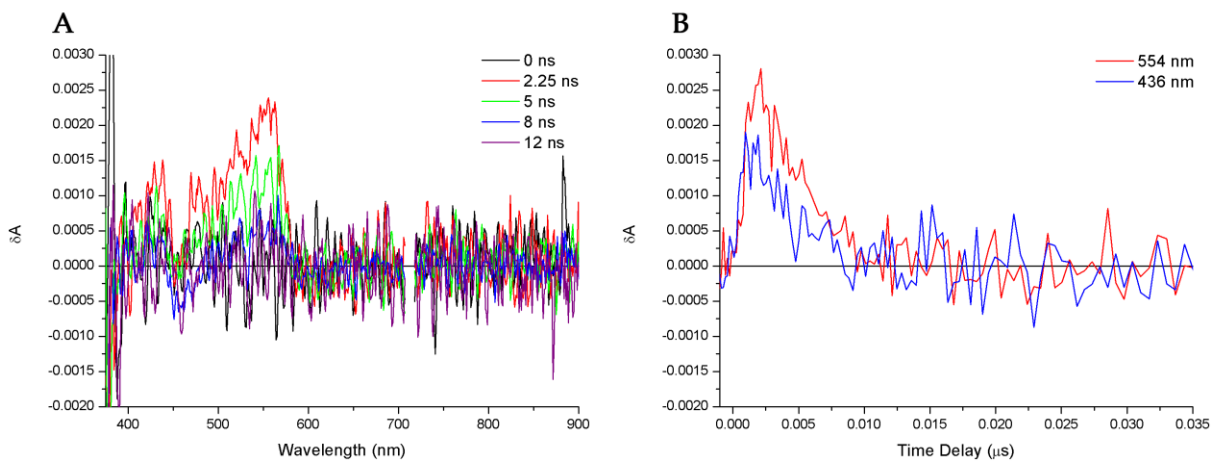


Figure 4.30: A) Transient absorption spectra for Zr(DHTA)/DQ, Bat-9. B) Transient absorption decay traces probed at 554 nm and 436 nm. TAS data for. The pump laser beam power was 1.017 mW and the measurement was performed for 16min47s.

Compared to Bat-8, promoted by HCl, Bat-9 (Figure 4.30A), promoted by demiwasser, shows a much less clear transient at 554 nm. It can be expected that the transient at 465 nm would also be present as well but due to the noise it cannot be observed. At 436 nm an indication for this transient is observed and analyzed. No bleach was observed in this data. Again exponential fits for the kinetics show there is one exponential component in the decay, which has a lifetime of about 3.8-4.0 ns. This indicates the MOF promoted by demiwasser has a shorter lived transient, but do note the large error in this measurement due to the noise, making this inconclusive.

TAS data for Bat-14, exhibiting both the ATA and DHTA linker is shown in Figure 4.31 and Figure 4.32. The spectra observed in Figure 4.31A show that there are clear transients at 465 nm and 554 nm related to the DHTA linker. The bleach at 608 nm is not observed since there seems to be a general shift in baseline for these measurements in which this bleach signal is lost. Decay traces at other wavelengths,

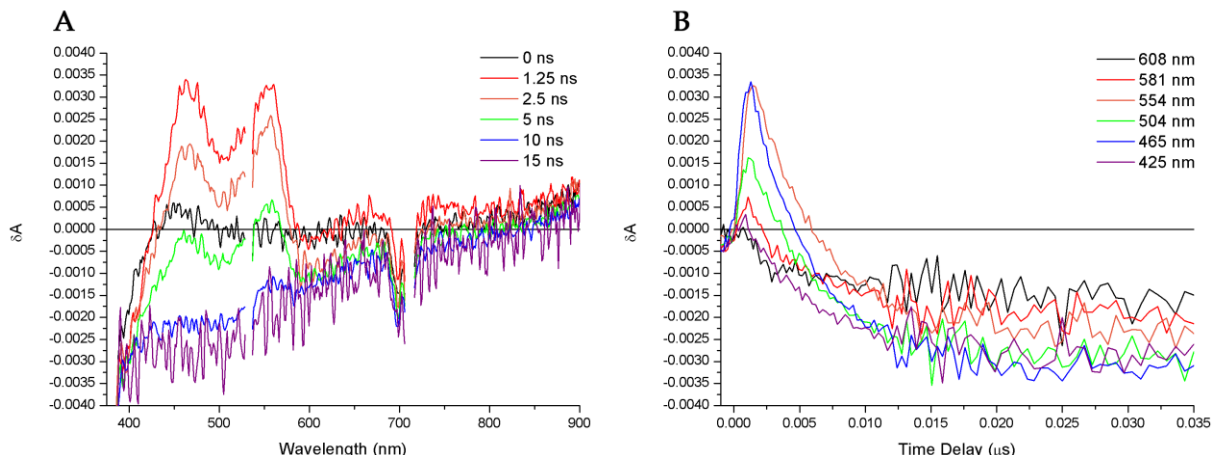


Figure 4.31: A) Transient absorption spectra for Zr(ATA)(DHTA)/HCl, Bat-14. B) Transient absorption decay traces probed at 608 nm, 581 nm, 554 nm, 465 nm and 425 nm. The pump laser beam power was 1.745 mW and the measurement was performed for 30min56s.

425 nm (bleach for ATA MOFs) and 504 nm and 580 nm (transients for ATA MOFs) have also been analyzed. However no clear lifetimes relatable to the ATA linker have been observed. This could be explained by the observed tendency for the ATA transients to have a lower extinction coefficient than the DHTA transients at this pump wavelength at shorter time delays. At longer time delays however, this ATA signal should be observed if it is present. This will be evident from data presented later in this section. Fitting the kinetics shows two exponential components in the decay, one of which tells us that the observed transients exhibit a lifetime of about 4.9-5.0 ns. This indicates that the mixed MOF has lifetimes slightly larger than the Zr-MOFs with just DHTA, again the error is too large to say for sure.

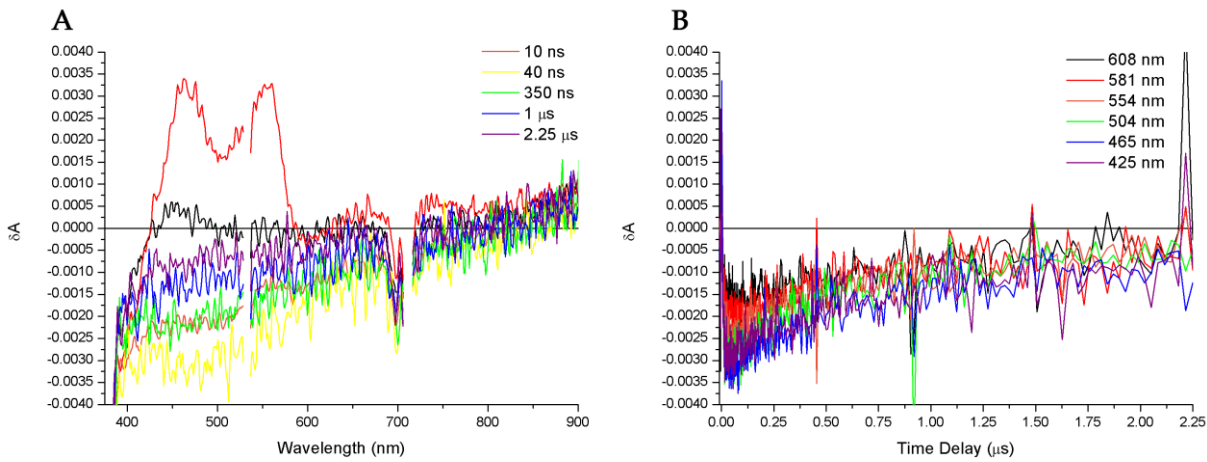


Figure 4.32: A) Transient absorption spectra for Zr(ATA)(DHTA)/DQ, Bat-14. **B)** Transient absorption decay traces probed at 608 nm, 581 nm, 554 nm, 504 nm, 465 nm and 425 nm. The pump laser beam power was 1.745 mW and the measurement was performed for 30min56s. This is the same data as given in Figure 4.31 only now at longer timescales.

On top of that there is the general shift in signal which is observed over a longer timescale. Figure 4.32 shows this in more detail. From this data is cannot be concluded if this shift in baseline is an artifact related to this particular measurement or if this is a large bleach related to this MOF. This negative δA is related to the second exponential component observed in for these fits. About 772-813 ns is the lifetime found for the restoration of this negative signal. Finally no data is shown for the Zr(ATA) MOFs because no data could be obtained with signal-to-noise ratios sufficient for exponential fitting.

In Figure 4.33 the data for the Cu(ATA)(DABCO) Bat-16 is shown. Bat-11 yielded similar data (Figure A.2 in the Appendix). A clear transient is observed at 581 nm. Also evident from Figure 4.33A is that after some time (see the 75 ns (blue) and 200 ns (purple) curves) there is a second transient at 504 nm which is longer lived but lost in the signal of 581 nm at shorter lifetimes. There is also bleaching visible at 425 nm. The kinetics are analyzed at 504 nm and 581 nm. At 504 nm a fit is found including two exponential components in the decay. One with a short lifetime, about 17.2 ns,

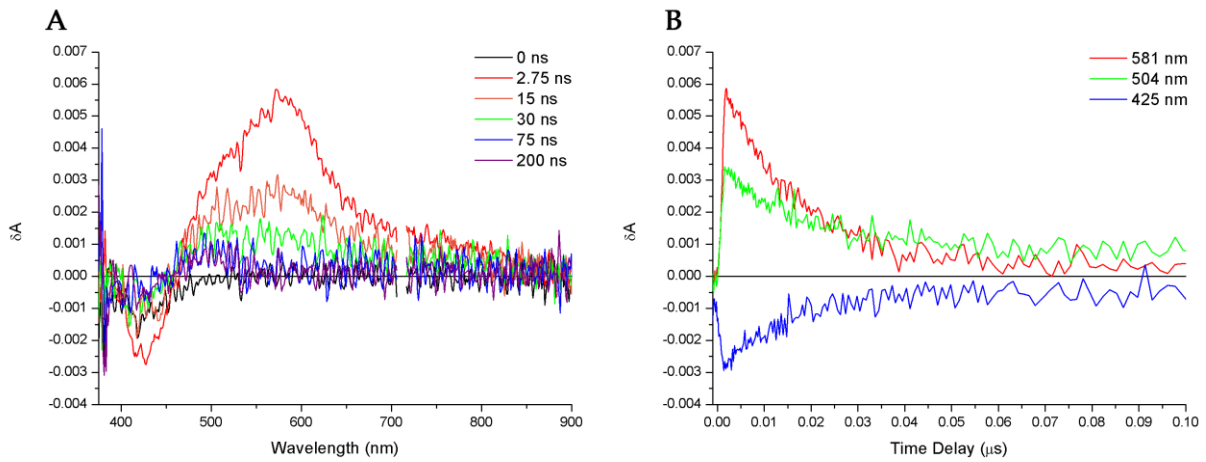


Figure 4.33: A) Transient absorption spectra for Cu(DABCO)(ATA)/DQ, Bat-16. B) Transient absorption decay traces probed at 581 nm, 504 nm and 425 nm. The pump laser beam power was 0.978 mW and the measurement was performed for 30min44s.

and one longer lived for about 661.1 ns. The fit at 581 nm however only shows one exponential component which relates to a lifetime of about 18.5 ns. The bleach seems to restore upon the shorter decays but the remainder can be observed for at least 10 μs even though the second component of the 504 nm signal is depleted much faster than that. It is not evident whether this is due to an artifact keeping the baseline low at 425 nm, or that there is an unobserved long-lived state preventing the ground state from completely being regenerated on these timescales.

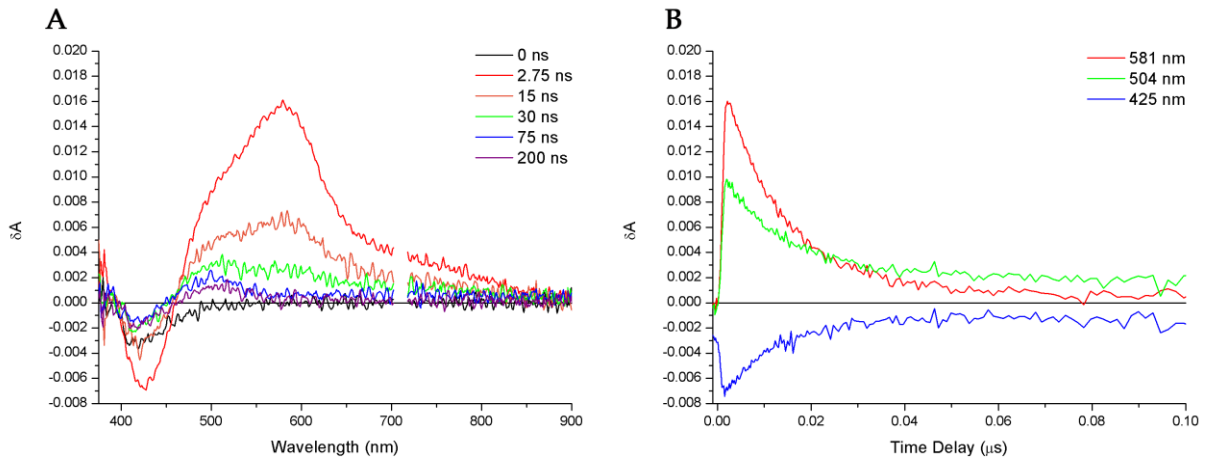


Figure 4.34: A) Transient absorption spectra for Co(ATA)/DQ, Bat-17. B) Transient absorption decay traces probed at 581 nm, 504 nm and 425 nm. The pump laser beam power was 0.992 mW and the measurement was performed for 24min08s.

This sample was also tested without N₂ purging (Figure A.3 in the Appendix), this had significant effects on the lifetime for this sample. The lifetime of the 581 nm component was similar at 18.1 ns, but the lifetimes of the 504 nm components were

16.0 ns and 329.2 ns when oxygen is present. This indicates that oxygen interferes with the charge carrier dynamics resulting in this lower lifetime.

Figure 4.34 gives the TAS data for Co(ATA), Bat-17. The data (Figure A.4 in the Appendix) of Bat-18 (Co(ATA)(DABCO)) is very similar to this dataset in terms of spectral shape and lifetimes. Like with Cu(ATA)(DABCO) two different transient signals are seen at 504 nm and 581 nm with a bleaching effect at 425 nm. Again at 581 nm only one exponential component is found in the decay, the lifetime of this component is about 14.4 ns. For 504 nm there are two components as well. One lives only shortly for about 12.6 ns while the other component has a lifetime of 252.4 ns. Since here the ATA linker is present as well it is expected this behavior relates to the linker.

This sample also has been tested without N₂ purging (Figure A.5 in the Appendix). This again had a significant effect on the lifetimes. In this case for 581 nm a lifetime of 14.6 ns is found, which is similar to the sample which is purged. For 504 nm lifetimes of 14.3 ns and 325.7 ns are found. As with the Cu(ATA)(DABCO) MOFs the transient at 581 nm seems unaffected by the presence of oxygen but the transient at 504 nm is affected. In this case the lifetime of the transient increases. It is noteworthy that the lifetime of the long living state is similar for both samples with oxygen present. The reason for these observations is not yet understood.

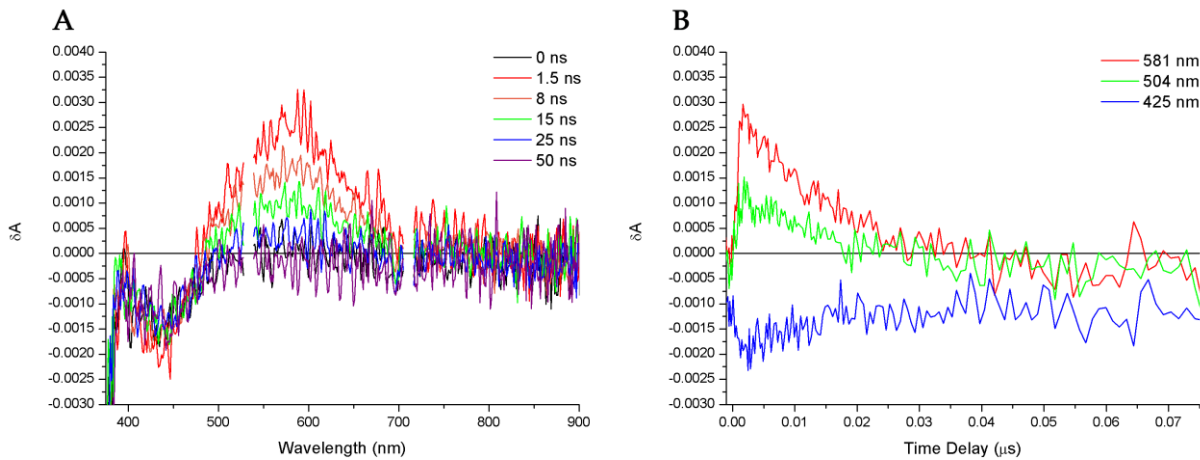


Figure 4.35: A) Transient absorption spectra for Ti(ATA)/MeOH, Bat-26. B) Transient absorption decay traces probed at 581 nm, 504 nm and 425 nm. The pump laser beam power was 0.980 mW and the measurement was performed for 22min24s.

The last MOFs studied are the MIL-125(Ti) MOFs. In Figure 4.35 the TAS data for Bat-26, MIL-125(Ti)-NH₂, is shown. As with the other ATA MOFs a clear transient is found at 581 nm with a bleach at 425 nm. In this case the longer lived transient at 504 nm is not observed. The reason for this can be the absence of this transient or the fact the signal-to-noise ratio is too low for this state to be seen in this measurement. At both 504 nm and 581 nm the kinetics have been fitted with exponentials. For 504 nm a lifetime of 14.7 ns is found, for 581 nm a lifetime of 15.0 ns is found. The negative transient at 425 nm remains at a negative δA the entire time, even before the effects

of the pump pulse are observed. It cannot be said for sure whether this originates from a long-lived bleach, a stimulated emission or that it is an artifact.

Figure 4.36 shows the TAS data for Bat-28, MIL-125(Ti)-(OH)₂. As was the case for UiO-66-(OH)₂ two transients peaks are observed at 465 nm and 554 nm. Fitting the kinetics of both yield lifetimes of 4.6 ns and 4.8 ns respectively. The negative transient at 608 nm follows this trend. This data suggests that the ground state of this MOF is regenerated almost completely after 20 ns, as can be observed from the decay traces in Figure 4.36B.

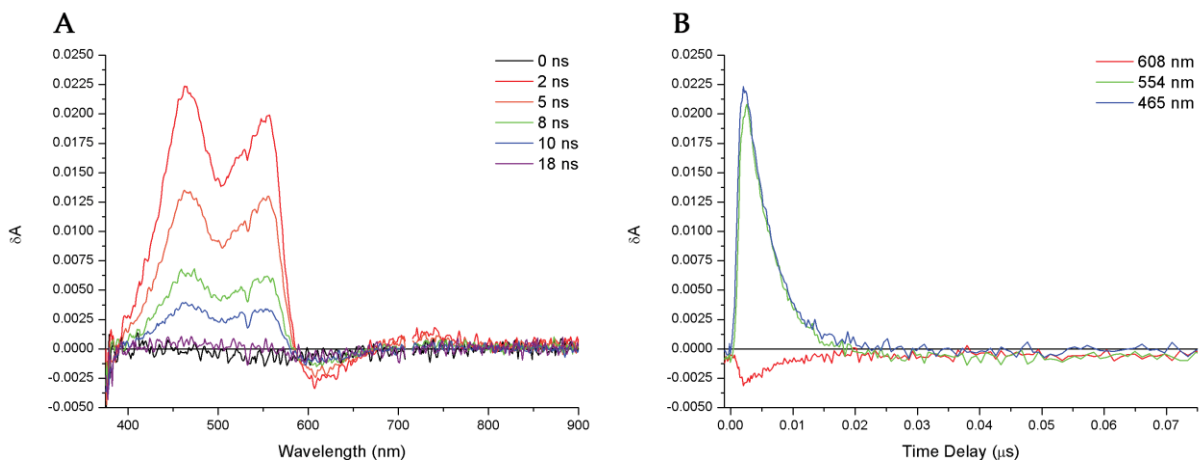


Figure 4.36: A) Transient absorption spectra for Ti(DHTA)/MeOH, Bat-28. B) Transient absorption decay traces probed at 608 nm, 554 nm and 465 nm TAS data for. The pump laser beam power was 0.925 mW and the measurement was performed for 22min22s.

4.4: Summary and General discussion

From the various characterization techniques the following properties of the MOFs have been observed. When the right synthesis procedures have been found, where the promotor is observed to be a critical factor, the MOFs being formed are very crystalline and also can be kept in solvents or air for a long time, in some cases for at least a year, without losing this crystallinity, which was observed with XRD.

However, when testing these samples for photocatalytic hydrogen production, it was observed that there is a lack of activity as opposed to reports in literature.^[55] Through discussions with a research group of Delft University, especially with Maxim Nasalevich^[67], we learned they too found that these MOFs are not as active as claimed.

UV-Vis and TAS were used to obtain more in-depth knowledge of the charge carrier dynamics to explain this lack of activity. With UV-Vis it was observed that the MOFs do indeed absorb light from the visible region of the light spectrum. With TAS it was found that there are transients related to the organic linkers, but that these states only live very shortly. These lifetimes are summarized in Table 4.1. Lifetimes of only 4-5 ns have been found for MOFs with the DHTA linker. Lifetimes of about 15 ns have

been found for MOFs with the ATA linker, where the Cu(DABCO)(ATA)/DQ, Co(ATA)/DQ and Co(DABCO)(ATA)/DQ MOFs show another, longer lived state. This state has lifetimes of few hundred nanoseconds. This transient could be potentially interesting for catalyzing redox reactions, further studies will be performed to improve the catalytic activity towards proton reduction.

Table 4.1: Collection of lifetimes per MOF. The short lifetime is given in the middle row. The longer lifetime is given in the last row if it was observed.

MOF	Lifetime 1 (ns)	Lifetime 2 (ns)
Zr(DHTA)	3.82-4.71	
Ti(DHTA)	4.546-4.755	
Zr(ATA)(DHTA)	4.92-4.98	771.6-812.9
Cu(ATA)(DABCO)	14.68-18.46	507.1-661.1
Co(ATA)	12.56-14.41	252.4
Co(ATA)(DABCO)	12.59-14.81	254.3
Ti(ATA)	14.74-14.97	

These results explain the observed lack of activity towards hydrogen evolution. The time scale on which this reaction generally takes place is microseconds. In other words, the recombination processes are one to three orders of magnitude faster than the desired reduction. This means steps should be taken to improve the lifetime of the charge carriers if MOFs are desired as photoactive species in a system. In Chapter 6 several ways to improve these lifetimes will be proposed.

5. Conclusions

In this research it was found that immobilizing MOFs on a conductive substrate as FTO is not straightforward. Dropcasting is not a suitable method since this yields mechanically unstable films. A hydrothermal synthesis route can yield homogeneous films for Zr(ATA). For Co(ATA) it was found that the MOF can be deposited and is mechanically stable, but it remains unclear if this film is homogeneously distributed over the FTO, since SEM data has yet to be obtained. The other two MOFs, Cu(DABCO)(ATA) and Ti(DHTA), could be immobilized but it could not be proven that the MOF structure was the same as that in the powder counterparts because these films were too thin or amorphous to obtain conclusive XRD data. Also for Ti(DHTA) it was found the distribution over FTO was inhomogeneous.

When testing these films electrochemically it has been observed that most of the immobilized MOFs get either irreversibly reduced or oxidized. For Zr(ATA) it depended on the electrolyte whether an oxidation or reduction took place. In the cases of Cu(DABCO)(ATA) and Ti(DHTA) it was observed that after running CV the films were destabilized and fell off the FTO substrate. Finally the Co(ATA) MOF films was observed to be more active in an oxidation reaction than FTO, but it has yet to be proven what reaction is taking place.

For photocatalytic MOF particles the synthesis procedure was found that the length of the synthesis does not influence the product for synthesis times between 24 and 72 hours. The sensitivity to temperature also is low since syntheses at 110 °C and 120 °C yielded the same products. The promotor does greatly influence the products however and the following optimal combinations have been found for the tried MOFs and promotors: Zr-MOFs with HCl, Co-MOFs and Cu-MOFs with demiwater and Ti-MOFs with methanol.

Some of these MOFs have been studied for photocatalytic hydrogen production afterwards. The tested MOFs, Zr(ATA)/HCl, Zr(ATA)/DQ, Zr(DHTA)/HCl, Zr(DHTA)/DQ and Cu(DABCO)(ATA)/DQ all showed no photocatalytic activity. Discussions with Maxim Nasalevich (Delft University) confirmed that indeed many MOFs are not as photocatalytically active as claimed in literature.

Finally the MOFs have been studied in terms of photophysical properties. It has been found that the MOFs do indeed absorb light, in the UV as well as in the visible part of the spectrum. It has also been found that this light absorption is indeed mainly related to the linker, although for most cases (Cu-, Co-, and Ti-MOFs) there were more absorption bands present depending on the metal. Transient absorption spectroscopy results showed that there are transients present in each case and that they are related to the linker, agreeing with the UV-Vis spectroscopy data. From the TAS data could also be read that the formed transients are very short-lived. 10-20 ns for MOFs with DHTA as a linker. The MOFs with ATA as a linker showed two decays, one of 10-20 ns and one of 200-600 ns. Since proton reduction occurs on a μ s timescale these decays are too fast and thus is the lack of photocatalytic activity explained.

6. Outlook

In this work MOFs have been explored in detail for photocatalytic hydrogen reduction. It has been found that standalone the tested materials are most likely not suitable. More tests are necessary to study the photocatalytic activity towards hydrogen production from water. CO₂ reduction tests should also be performed to exclude the possibility the MOFs are only photocatalytically active towards CO₂ reduction. However with the observed short-lived transients it is unlikely CO₂ reduction will take place. Also the observed oxidations occurring on the MOFs are interesting for future studies. A possibility is that the oxidation of water is taking place. *In situ* studies like online electrochemical mass spectroscopy (OLEMS) can be performed to observe oxygen if it is being evolved.

With transient absorption spectroscopy it has been found that one of the bottlenecks in the observed lack of photocatalytic activity is a fast recombination of charge carriers. However, these results are not yet sufficient to get a complete picture of the charge dynamics in MOFs. Future work should include other time-resolved techniques such as time-resolved electron paramagnetic resonance spectroscopy (tr-EPR) or time-resolved X-ray absorption spectroscopy (tr-XAS) to study charge dynamics at the metal nodes. Studies using static EPR already show there is a transition from M⁴⁺ to M³⁺ and back for Zr- and Ti-MOFs. [56, 63] Time-resolved techniques can be used to more closely relate the found activity of these MOFs to the charge dynamics.

Knowing the charge dynamics in more detail points out whether the extraction of excited electrons from the linkers should be improved, for example by using mediators or charge extractors. On the other hand if the metal nodes do get reduced but do not catalyze reduction reactions afterwards, improvement is necessary on that part. One possibility is that the nodes have all their possible catalytic sites blocked by linkers, so introducing defects might open up paths toward catalytic activity.

Once the properties of MOFs in photocatalytic applications are fully understood another aspect that should be explored in detail is the immobilization of the MOFs on conductive substrates and possible improving the interface between those two materials. One possibility is by combining the MOFs with semiconductors or catalysts. These materials could for example improve the charge separation in the MOFs, thus improve the lifetime of the charges and give rise to possible photocatalytic activity. It also allows for designing MOF systems focusing on fewer aspects. Meaning for example finding MOFs which are not necessarily photocatalytically active but have a very high light response. Some state-of-the-art examples of these kinds of hybrid systems have already been mentioned in Section 1.2.2.

The author is of opinion that MOFs are a very interesting class of materials and expects that they will be found in applications such as gas separation and storage in the near future. Another application were MOFs are expected to be found is photocatalysis. However much work is still required to understand the bottlenecks the materials show up to now. This knowledge can then be applied to improve the properties of the materials and to implement them in photocatalytic systems. The

materials are versatile, relatively easy to produce and are mechanically and chemically quite robust. This means they can easily be combined with other materials without requiring special reaction conditions to work, making them great candidates for economically viable solutions to replace fossil fuels.

References

- [1]: (2014), www.eia.gov, visited at 28-03-2015/11:00, "U.S. Energy Information Administration"
- [2]: Allen, M. R., Barros, V. R., Broome, J., Cramer, W., Christ, R., Church, J. A., Clarke, L., Dahe, Q., Dasgupta, P., Dubash, N. K., Edenhofer, O., Elgizouli, I., Field, C. B., Forster, P., Friedlingstein, P., Fuglestvedt, J., Gomez-Echeverri, L., Hallegatte, S., Hegerl, G., Howden, M., Jiang, K., Cisneros, B. J., Kattsov, V., Lee, H., Mach, K. J., Marotzke, J., Mastrandrea, M. D., Minx, L. M. J., Mulugetta, Y., O'Brien, K., Oppenheimer, M., Pachauri, R. K., Pereira, J. J., Pichs-Madruga, R., Plattner, G.-K., Pörtner, H.-O., Power, S. B., Preston, B., Ravindranath, N. H., Reisinger, A., Riahi, K., Rusticucci, M., Scholes, R., Seyboth, K., Sokona, Y., Stavins, R., Stocker, T. F., Tsakert, P., Vuuren, D. van & Ypersele, J.-P. van, IPCC Fifth Assess. Synth. Rep., November (2014), "Climate Change 2014 Synthesis Report, Longer report"
- [3]: Kumar, B., Llorente, M., Froehlich, J., Dang, T., Sathrum, A. & Kubiak, C. P., Annu. Rev. Phys. Chem., **63** (2012), 541–569, "Photochemical and photoelectrochemical reduction of CO₂"
- [4]: Qiao, J., Liu, Y., Hong, F. & Zhang, J., Chemical Society reviews, **43** (2014), 631–675, "A review of catalysts for the electroreduction of carbon dioxide to produce low-carbon fuels."
- [5]: Fresno, F., Portela, R., Suárez, S. & Coronado, J. M., J. Mater. Chem. A, **2** (2014), 2863–2888, "Photocatalytic materials: recent achievements and near future trends"
- [6]: Horiuchi, Y., Toyao, T., Takeuchi, M., Matsuoka, M. & Anpo, M., Phys. Chem. Chem. Phys., **15** (2013), 13243–13253, "Recent advances in visible-light-responsive photocatalysts for hydrogen production and solar energy conversion--from semiconducting TiO₂ to MOF/PCP photocatalysts"
- [7]: Walter, M. G., Warren, E. L., McKone, J. R., Boettcher, S. W., Mi, Q., Santori, E. a & Lewis, N. S., Chem. Rev., **110** (2010), 6446–6473, "Solar Water Splitting Cells"
- [8]: Benson, E. E., Kubiak, C. P., Sathrum, A. J. & Smieja, J. M., Chem. Soc. Rev., **38** (2009), 89–99, "Electrocatalytic and homogeneous approaches to conversion of CO₂ to liquid fuels"
- [9]: Kudo, A. & Miseki, Y., Chem. Soc. Rev., **38** (2009), 253–278, "Heterogeneous photocatalyst materials for water splitting"

- [10]: Linsebigler, A. L., Lu, G. & Yates, J. T., *Chem. Rev.*, **95** (1995), 735–758, "Photocatalysis on TiO₂ Surfaces: Principles, Mechanisms, and Selected Results"
- [11]: Banerjee, S., Pillai, S. C., Falaras, P., O'Shea, K. E., Byrne, J. A. & Dionysiou, D. D., *J. Phys. Chem. C*, **5** (2014), 2543–2554, "New Insights into the Mechanism of Visible Light Photocatalysis"
- [12]: Djurišić, A. B., Leung, Y. H. & Ching Ng, A. M., *Mater. Horizons*, **1** (2014), 400–410, "Strategies for improving the efficiency of semiconductor metal oxide photocatalysis"
- [13]: Liu, B., Zhao, X., Terashima, C., Fujishima, A. & Nakata, K., *Phys. Chem. Chem. Phys.*, **16** (2014), 8751–8760, "Thermodynamic and kinetic analysis of heterogeneous photocatalysis for semiconductor systems"
- [14]: Fujishima, A. & Honda, K., *Nature*, **238** (1972), 37–38, "Electrochemical photolysis of water at a semiconductor electrode"
- [15]: Maeda, K., Lu, D. & Domen, K., *ACS Catal.*, **3** (2013), 1026–1033, "Solar-driven Z-scheme water splitting using modified BaZrO₃-BaTaO₂N solid solutions as photocatalysts"
- [16]: Lu, X., Xie, S., Yang, H., Tong, Y. & Ji, H., *Chem. Soc. Rev.*, **43** (2014), 7581–7593, "Photoelectrochemical hydrogen production from biomass derivatives and water"
- [17]: Nozik, A. J. & Memming, R., *J. Phys. Chem.*, **100** (1996), 13061–13078, "Physical Chemistry of Semiconductor–Liquid Interfaces"
- [18]: Delacourt, C., Ridgway, P. L., Kerr, J. B. & Newman, J., *J. Electrochem. Soc.*, **155** (2008), B42–B49, "Design of an Electrochemical Cell Making Syngas (CO + H₂) from CO₂ and H₂O Reduction at Room Temperature"
- [19]: Rajeshwar, K., *Encycl. Electrochem.*, **6** (2001), 3–53, "Fundamentals of semiconductor electrochemistry and photoelectrochemistry"
- [20]: Abdi, F. F., Han, L., Smets, A. H. M., Zeman, M., Dam, B. & van de Krol, R., *Nat. Commun.*, **4** (2013), 2195, "Efficient solar water splitting by enhanced charge separation in a bismuth vanadate-silicon tandem photoelectrode."
- [21]: Zhu, Q.-L. & Xu, Q., *Chem. Soc. Rev.*, **43** (2014), 5648–5512, "Metal-organic framework composites"
- [22]: Furukawa, S., Reboul, J., Diring, S., Sumida, K. & Kitagawa, S., *Chem. Soc. Rev.*, **43** (2014), 5700–5734, "Structuring of metal-organic frameworks at the mesoscopic/macrosopic scale."

- [23]: Cook, T. R., Zheng, Y. R. & Stang, P. J., *Chem. Rev.*, **113** (2013), 734–777, "Metal-organic frameworks and self-assembled supramolecular coordination complexes: Comparing and contrasting the design, synthesis, and functionality of metal-organic materials"
- [24]: Korotcenkov, G., *Handbook of Gas Sensor Materials, Chapter 11* (2014), 181–184, "Metal-Organic Frameworks"
- [25]: Kosal, M. E., Chou, J.-H., Wilson, S. R. & Suslick, K. S., *Nature Mater.*, **1** (2002), 118–121, "A functional zeolite analogue assembled from metalloporphyrins"
- [26]: Eddaoudi, M., Kim, J., Rosi, N., Vodak, D., Wachter, J., O'Keeffe, M. & Yaghi, O. M., *Science*, **295** (2002), 469–472, "Systematic design of pore size and functionality in isoreticular MOFs and their application in methane storage"
- [27]: Rana, M. K., Koh, H. S., Zuberi, H. & Siegel, D. J., *J. Phys. Chem. C*, **118** (2014), 2929–2942, "Methane storage in metal-substituted metal-organic frameworks: Thermodynamics, usable capacity, and the impact of enhanced binding sites"
- [28]: Ramaswamy, P., Wong, N. E. & Shimizu, G. K. H., *Chem. Soc. Rev.*, **43** (2014), 5913–5932, "MOFs as proton conductors - challenges and opportunities"
- [29]: Qiu, S., Xue, M. & Zhu, G., *Chem. Soc. Rev.*, **43** (2014), 6116–6140, "Metal-organic framework membranes: from synthesis to separation application"
- [30]: Zhang, T. & Lin, W., (Springer-Verlag, 2013), doi:10.1007/430_2013_131, "Metal-Organic Frameworks for Photocatalysis"
- [31]: Zhang, T. & Lin, W., *Chem. Soc. Rev.*, **43** (2014), 5982–5993, "Metal-organic frameworks for artificial photosynthesis and photocatalysis"
- [32]: Wang, J. L., Wang, C. & Lin, W., *ACS Catal.*, **2** (2012), 2630–2640, "Metal-organic frameworks for light harvesting and photocatalysis"
- [33]: Nasalevich, M. a., van der Veen, M., Kapteijn, F. & Gascon, J., *CrystEngComm*, **16** (2014), 4919–4926, "Metal-organic frameworks as heterogeneous photocatalysts: advantages and challenges"
- [34]: Nasalevich, M. a, Goesten, M. G., Savenije, T. J., Kapteijn, F. & Gascon, J., *Chem. Commun.*, **49** (2013), 10575–10577, "Enhancing optical absorption of metal-organic frameworks for improved visible light photocatalysis"
- [35]: Gao, S., Liu, W., Shang, N., Feng, C., Wu, Q. & Wang, Z., *RSC Adv.*, **4** (2014), 61736–61742, "Integration of a plasmonic semiconductor with a metal-organic framework: a case of Ag/AgCl@ZIF- 8 with enhanced visible light photocatalytic activity"

- [36]: Liu, Q., Low, Z.-X., Li, L., Razmjou, A., Wang, K., Yao, J. & Wang, H., *J. Mater. Chem. A*, **1** (2013), 11563–11569, "ZIF-8/Zn₂GeO₄ nanorods with an enhanced CO₂ adsorption property in an aqueous medium for photocatalytic synthesis of liquid fuel"
- [37]: Zhan, W., Kuang, Q., Zhou, J., Kong, X., Xie, Z. & Zheng, L., *J. Am. Chem. Soc.*, **135** (2012), 1926–1933, "Semiconductor@Metal–Organic Framework Core–Shell Heterostructures: A Case of ZnO@ZIF-8 Nanorods with Selective Photoelectrochemical Response"
- [38]: Bordiga, S., Regli, L., Bonino, F., Groppe, E., Lamberti, C., Xiao, B., Wheatley, P. S., Morris, R. E. & Zecchina, A., *Phys. Chem. Chem. Phys.*, **9** (2007), 2676–2685, "Adsorption properties of HKUST-1 toward hydrogen and other small molecules monitored by IR"
- [39]: Cavka, J. H., Jakobsen, S., Olsbye, U., Guillou, N., Lamberti, C., Bordiga, S. & Lillerud, K. P., *J. Am. Chem. Soc.*, **130** (2008), 13850–13851, "A New Zirconium Inorganic Building Brick Forming Metal Organic Frameworks with Exceptional Stability"
- [40]: Dan-Hardi, M., Serre, C., Frot, T., Rozes, L., Maurin, G., Sanchez, C., Férey, G. & Maurín, G., *J. Am. Chem. Soc.*, **131** (2009), 10857–10859, "A new photoactive highly porous titanium (IV) dicarboxylate"
- [41]: Mao, J., Yang, L., Yu, P., Wei, X. & Mao, L., *Electrochim. Commun.*, **19** (2012), 29–31, "Electrocatalytic four-electron reduction of oxygen with copper (II)-based metal-organic frameworks"
- [42]: Senthil Kumar, R., Senthil Kumar, S. & Anbu Kulandainathan, M., *Electrochim. Commun.*, **25** (2012), 70–73, "Highly selective electrochemical reduction of carbon dioxide using Cu based metal organic framework as an electrocatalyst"
- [43]: Fu, Y., Sun, D., Qin, M., Huang, R. & Li, Z., *RSC Adv.*, **2** (2012), 3309–3314, "Cu(II)-and Co(II)-containing metal-organic frameworks (MOFs) as catalysts for cyclohexene oxidation with oxygen under solvent-free conditions"
- [44]: Joaristi, A. M., Juan-alcan, J., Serra-crespo, P., Kapteijn, F. & Gascon, J., *Cryst. Growth Des.*, **12** (2012), 3489–3498, "Electrochemical Synthesis of Some Archetypical Zn²⁺, Cu²⁺, and Al³⁺ Metal Organic Frameworks"
- [45]: Lee, D. Y., Shin, C. Y., Yoon, S. J., Lee, H. Y., Lee, W., Shrestha, N. K., Lee, J. K. & Han, S.-H., *Sci. Rep.*, **4** (2014), 3930, "Enhanced photovoltaic performance of Cu-based metal-organic frameworks sensitized solar cell by addition of carbon nanotubes"
- [46]: Chavan, S., Vitillo, J. G., Uddin, M. J., Bonino, F., Lamberti, C., Groppe, E., Lillerud, K. P. & Bordiga, S., *Chem. Mater.*, **22** (2010), 4602–4611,

"Functionalization of UiO-66 metal-organic framework and highly cross-linked polystyrene with Cr(CO)3: In situ formation, stability, and photoreactivity"

- [47]: Biswas, S. & Van Der Voort, P., *Eur. J. Inorg. Chem.*, **2013** (2013), 2154–2160, "A general strategy for the synthesis of functionalised UiO-66 frameworks: Characterisation, stability and CO₂ adsorption properties"
- [48]: Garibay, S. J. & Cohen, S. M., *Chem. Commun.*, **46** (2010), 7700–7702, "Isoreticular synthesis and modification of frameworks with the UiO-66 topology"
- [49]: Kandiah, M., Nilsen, M. H., Usseglio, S., Jakobsen, S., Olsbye, U., Tilset, M., Larabi, C., Quadrelli, E. A., Bonino, F. & Lillerud, K. P., *Chem. Mater.*, **22** (2010), 6632–6640, "Synthesis and stability of tagged UiO-66 Zr-MOFs"
- [50]: Katz, M. J., Brown, Z. J., Colón, Y. J., Siu, P. W., Scheidt, K. a, Snurr, R. Q., Hupp, J. T. & Farha, O. K., *Chem. Commun.*, **49** (2013), 9449–51, "A facile synthesis of UiO-66, UiO-67 and their derivatives."
- [51]: Kim, S. N., Lee, Y. R., Hong, S. H., Jang, M. S. & Ahn, W. S., *Catal. Today*, (2014), doi:10.1016/j.cattod.2014.05.041, "Pilot-scale synthesis of a zirconium-benzenedicarboxylate UiO-66 for CO₂ adsorption and catalysis"
- [52]: Schaate, A., Roy, P., Godt, A., Lippke, J., Waltz, F., Wiebcke, M. & Behrens, P., *Chem. Eur. J.*, **17** (2011), 6643–6651, "Modulated synthesis of Zr-based metal-organic frameworks: From nano to single crystals"
- [53]: Shearer, G. C., Chavan, S., Ethiraj, J., Vitillo, J. G., Svelle, S., Olsbye, U., Lamberti, C., Bordiga, S. & Lillerud, K. P., *Chem. Mater.*, **26** (2014), 4068–4071, "Tuned to Perfection: Ironing Out the Defects in Metal-Organic Framework UiO-66"
- [54]: Schoenecker, P. M., Belancik, G. A., Grabicka, B. E. & Walton, K. S., *AIChE*, **59** (2013), 1255–1262, "Kinetics Study and Crystallization Process Design for Scale-Up of UiO-66-NH₂ Synthesis"
- [55]: Silva, C. G., Luz, I., Llabrés I Xamena, F. X., Corma, A. & García, H., *Chem. Eur. J.*, **16** (2010), 11133–11138, "Water stable Zr-Benzene dicarboxylate metal-organic frameworks as photocatalysts for hydrogen generation"
- [56]: Sun, D., Fu, Y., Liu, W., Ye, L., Wang, D., Yang, L., Fu, X. & Li, Z., *Chem. Eur. J.*, **19** (2013), 14279–14285, "Studies on photocatalytic CO₂ reduction over NH 2- uiO-66(Zr) and its derivatives: Towards a better understanding of photocatalysis on metal-organic frameworks"
- [57]: Shen, L., Luo, M., Liu, Y., Liang, R., Jing, F. & Wu, L., *Applied Catal. B, Environ.*, **166-167** (2015), 445–453, "Noble-metal-free MoS₂ co-catalyst decorated UiO-66 / CdS hybrids for efficient photocatalytic H₂ production"

- [58]: Wang, C., Kathryn, E. & Lin, W., J. Am. Chem. Soc., **134** (2012), 7211–7214, "Pt Nanoparticles@Photoactive Metal–Organic Frameworks: Efficient Hydrogen Evolution via Synergistic Photoexcitation and Electron Injection"
- [59]: Wang, C., Xie, Z., Dekrafft, K. E. & Lin, W., J. Am. Chem. Soc., **133** (2011), 13445–13454, "Doping metal-organic frameworks for water oxidation, carbon dioxide reduction, and organic photocatalysis"
- [60]: Laurier, K. G. M., Vermoortele, F., Ameloot, R., Vos, D. E. De, Hofkens, J. & Roe, M. B. J., J. Am. Chem. Soc., **135** (2013), 14488–14491, "Iron(III)-Based Metal – Organic Frameworks As Visible Light Photocatalysts"
- [61]: Ai, L., Zhang, C., Li, L. & Jiang, J., Appl. Catal. B Environ., **148-149** (2014), 191–200, "Iron terephthalate metal-organic framework: Revealing the effective activation of hydrogen peroxide for the degradation of organic dye under visible light irradiation"
- [62]: Abedi, S. & Morsali, A., New J. Chem., (2014), doi:10.1039/C4NJ01536C, "Assisted synthesized Ti-containing MOF photocatalyst under blue LED irradiation"
- [63]: De Miguel, M., Ragon, F., Devic, T., Serre, C., Horcajada, P. & García, H., ChemPhysChem, **13** (2012), 3651–3654, "Evidence of photoinduced charge separation in the metal-organic framework MIL-125(Ti)-NH₂"
- [64]: Fu, Y., Sun, D., Chen, Y., Huang, R., Ding, Z., Fu, X. & Li, Z., Angew. Chem. Int. Ed., **51** (2012), 3364–3367, "An amine-functionalized titanium metal-organic framework photocatalyst with visible-light-induced activity for CO₂ reduction"
- [65]: Gao, J., Miao, J., Li, P.-Z., Teng, W. Y., Yang, L., Zhao, Y., Liu, B. & Zhang, Q., Chem. Commun., **50** (2014), 3786–3788, "A p-type Ti(iv)-based metal-organic framework with visible-light photo-response"
- [66]: Sun, D., Liu, W., Fu, Y., Fang, Z., Sun, F., Fu, X., Zhang, Y. & Li, Z., Chem. Eur. J., **20** (2014), 4780–4788, "Noble metals can have different effects on photocatalysis over metal-organic frameworks (MOFs): a case study on M/NH₂-MIL-125(Ti) (M=Pt and Au)"
- [67]: Nasalevich, M. A., Becker, R., Ramos-Fernandez, E. V., Castellanos, S., Veber, S. L., Fedin, M. V., Kapteijn, F., Reek, J. N. H., Vlugt, J. I. van der & Gascon, J., Energy Environ. Sci., **8** (2014), 364–375, "Co@NH₂-MIL-125(Ti): cobaloxime-derived metal- organic framework-based composite for light- driven H₂ production"
- [68]: Hou, C., Xu, Q., Wang, Y. & Hu, X., RSC Adv., **3** (2013), 19820–19823, "Synthesis of Pt@NH₂-MIL-125(Ti) as a photocathode material for photoelectrochemical hydrogen production"

- [69]: Wang, S., Yao, W., Lin, J., Ding, Z. & Wang, X., *Angew. Chem. Int. Ed.*, **53** (2014), 1034–1038, "Cobalt imidazolate metal-organic frameworks photosplit CO₂ under mild reaction conditions"
- [70]: Ahrenholtz, S. R., Epley, C. C. & Morris, A. J., *J. Am. Chem. Soc.*, **136** (2014), 2464–2472, "Solvothermal preparation of an electrocatalytic metalloporphyrin MOF thin film and its redox hopping charge-transfer mechanism"
- [71]: Zhu, Y.-M., Zeng, C.-H., Chu, T.-S., Wang, H.-M., Yang, Y.-Y., Tong, Y.-X., Su, C.-Y. & Wong, W.-T., *J. Mater. Chem. A*, **1** (2013), 11312–11319, "A novel highly luminescent LnMOF film: a convenient sensor for Hg²⁺ detecting"
- [72]: Zhou, T., Du, Y., Borgna, A., Hong, J., Wang, Y., Han, J., Zhang, W. & Xu, R., *Energy Environ. Sci.*, **6** (2013), 3229–3234, "Post-synthesis modification of a metal-organic framework to construct a bifunctional photocatalyst for hydrogen production"
- [73]: Zhang, X., Ballem, M. A., Hu, Z. J., Bergman, P. & Uvdal, K., *Angew. Chem. Int. Ed.*, **50** (2011), 5729–5733, "Nanoscale light-harvesting metal-organic frameworks"
- [74]: Zhang, C. Y., Ma, W. X., Wang, M. Y., Yang, X. J. & Xu, X. Y., *Spectrochim. Acta A*, **118** (2014), 657–662, "Structure, photoluminescent properties and photocatalytic activities of a new Cd(II) metal-organic framework"
- [75]: Fateeva, A., Chater, P. a., Ireland, C. P., Tahir, A. a., Khimyak, Y. Z., Wiper, P. V., Darwent, J. R. & Rosseinsky, M. J., *Angew. Chem. Int. Ed.*, **51** (2012), 7440–7444, "A water-stable porphyrin-based metal-organic framework active for visible-light photocatalysis"
- [76]: Choi, S., Watanabe, T., Bae, T. H., Sholl, D. S. & Jones, C. W., *J. Phys. Chem. Lett.*, **3** (2012), 1136–1141, "Modification of the Mg/DOBDC MOF with amines to enhance CO₂ adsorption from ultradilute gases"
- [77]: Sarkisov, L., Martin, R. L., Haranczyk, M. & Smit, B., *J. Am. Chem. Soc.*, **136** (2014), 2228–2231, "On the flexibility of metal-organic frameworks"
- [78]: Wang, C., Liu, D., Xie, Z. & Lin, W., *Inorg. Chem.*, **53** (2014), 1331–1338, "Functional metal-organic frameworks via ligand doping: Influences of ligand charge and steric demand"
- [79]: Farha, O. K. & Hupp, J. T., *Acc. Chem. Res.*, **43** (2010), 1166–1175, "Rational Design, Synthesis, Purification, and Activation of Metal-Organic Framework Materials"
- [80]: Kong, X., Scott, E., Ding, W., Mason, J. a, Long, J. R. & Reimer, J. a, *J. Am. Chem. Soc.*, **134** (2012), 14341–14344, "CO₂ Dynamics in a Metal – Organic Framework with Open Metal Sites"

- [81]: Drisdell, W. S., Poloni, R., McDonald, T. M., Long, J. R., Smit, B., Neaton, J. B., Prendergast, D. & Kortright, J. B., *J. Am. Chem. Soc.*, **135** (2013), 18183–18190, "Probing Adsorption Interactions in Metal – Organic Frameworks using X-ray spectroscopy"
- [82]: Cui, Y., Yue, Y., Qian, G. & Chen, B., *Chem. Rev.*, **112** (2012), 1126–1162, "Luminescent Functional Metal-Organic Frameworks"
- [83]: Kent, C. a., Liu, D., Ma, L., Papanikolas, J. M., Meyer, T. J. & Lin, W., *J. Am. Chem. Soc.*, **133** (2011), 12940–12943, "Light harvesting in microscale metal-organic frameworks by energy migration and interfacial electron transfer quenching"
- [84]: Halls, J. E., Jiang, D., Burrows, A. D., Kulandainathan, M. A. & Marken, F., *Electrochemistry*, **12** (2014), 187–210, "Electrochemistry within metal-organic frameworks"
- [85]: Lee, D. Y., Shinde, D. V., Yoon, S. J., Cho, K. N., Lee, W., Shrestha, N. K. & Han, S., *J. Phys. Chem. C*, **118** (2013), 16328–16334, "Cu-Based Metal–Organic Frameworks for Photovoltaic Application"
- [86]: Yang, L. M., Fang, G. Y., Ma, J., Ganz, E. & Han, S. S., *Cryst. Growth Des.*, **14** (2014), 2532–2541, "Band gap engineering of paradigm MOF-5"
- [87]: Lee, C. Y., Farha, O. K., Hong, B. J., Sarjeant, A. a., Nguyen, S. T. & Hupp, J. T., *J. Am. Chem. Soc.*, **133** (2011), 15858–15861, "Light-harvesting metal-organic frameworks (MOFs): Efficient strut-to-strut energy transfer in bodipy and porphyrin-based MOFs"
- [88]: Gascon, J., Hernández-Alonso, M. D., Almeida, A. R., van Klink, G. P. M., Kapteijn, F. & Mul, G., *ChemSusChem*, **1** (2008), 981–983, "Isoreticular MOFs as efficient photocatalysts with tunable band gap: an operando FTIR study of the photoinduced oxidation of propylene"
- [89]: Liu, Y., Zhang, W., Li, S., Cui, C., Wu, J., Chen, H. & Huo, F., *Chem. Mater.*, **26** (2014), 1119–1125, "Designable Yolk–Shell Nanoparticle@MOF Petalous Heterostructures"
- [90]: Aijaz, A. & Xu, Q., *J. Phys. Chem. Lett.*, **5** (2014), 1400–1411, "Catalysis with metal nanoparticles immobilized within the pores of metal-organic frameworks"
- [91]: Li, R., Hu, J., Deng, M., Wang, H., Wang, X., Hu, Y., Jiang, H. L., Jiang, J., Zhang, Q., Xie, Y. & Xiong, Y., *Adv. Mater.*, **26** (2014), 4783–4788, "Integration of an inorganic semiconductor with a metal-organic framework: A platform for enhanced gaseous photocatalytic reactions"

- [92]: Ke, F., Qiu, L.-G., Yuan, Y.-P., Jiang, X. & Zhu, J.-F., *J. Mater. Chem.*, **22** (2012), 9497–9500, "Fe₃O₄@MOF core–shell magnetic microspheres with a designable metal–organic framework shell"
- [93]: Zhang, C.-F., Qiu, L.-G., Ke, F., Zhu, Y.-J., Yuan, Y.-P., Xu, G.-S. & Jiang, X., *J. Mater. Chem. A*, **1** (2013), 14329–14334, "A novel magnetic recyclable photocatalyst based on a core–shell metal–organic framework Fe₃O₄@MIL-100(Fe) for the decolorization of methylene blue dye"
- [94]: Wee, L. H., Janssens, N., Sree, S. P., Wiktor, C., Gobechiya, E., Fischer, R. A., Kirschhock, C. E. A. & Martens, J. A., *Nanoscale*, **6** (2014), 2056–2060, "Local transformation of ZIF-8 powders and coatings into ZnO nanorods for photocatalytic application"
- [95]: Hou, C., Peng, J., Xu, Q., Ji, Z. & Hu, X., *RSC Adv.*, **2** (2012), 12696–12698, "Elaborate Fabrication of MOF-5 Thin Films on Glassy Carbon Electrode (GCE) for Photoelectrochemical Sensors"
- [96]: Falcaro, P., Ricco, R., Doherty, C. M., Liang, K., Hill, A. J. & Styles, M. J., *Chem. Soc. Rev.*, **43** (2014), 5513–5560, "MOF positioning technology and device fabrication"
- [97]: Gascon, J., Aguado, S. & Kapteijn, F., *Micro. Meso. Mater.*, **113** (2008), 132–138, "Manufacture of dense coatings of Cu₃(BTC)₂ (HKUST-1) on α-alumina"
- [98]: Wade, C. R., Li, M. & Dincă, M., *Angew. Chem. Int. Ed.*, **52** (2013), 13377–13381, "Facile deposition of multicolored electrochromic metal–organic framework thin films"
- [99]: Talin, A. A., Centrone, A., Ford, A. C., Foster, M. E., Stavila, V., Haney, P., Kinney, R. A., Szalai, V., El Gabaly, F., Yoon, H. P., Léonard, F. & Allendorf, M. D., *Science*, **343** (2014), 66–69, "Tunable electrical conductivity in metal–organic framework thin-film devices."
- [100]: So, M. C., Jin, S., Son, H. J., Wiederrecht, G. P., Farha, O. K. & Hupp, J. T., *J. Am. Chem. Soc.*, **135** (2013), 15698–15701, "Layer-by-layer fabrication of oriented porous thin films based on porphyrin-containing metal–organic frameworks"
- [101]: Yadnum, S., Roche, J., Lebraud, E., Negriger, P., Garrigue, P., Bradshaw, D., Warakulwit, C., Limtrakul, J. & Kuhn, A., *Angew. Chem. Int. Ed.*, **53** (2014), 4001–4005, "Site-selective synthesis of Janus-type metal–organic framework composites"
- [102]: Liu, H., Wang, H., Chu, T., Yu, M. & Yang, Y., *J. Mater. Chem. C*, **2** (2014), 8683–8690, "An electrodeposited lanthanide MOF thin film as a luminescent sensor for carbonate detection in aqueous solution"

- [103]: Li, W., Lü, J., Gao, S., Li, Q. & Cao, R., *J. Mater. Chem. A*, **2** (2014), 19473–19478, "Electrochemical preparation of metal-organic framework films for fast detection of nitro"
- [104]: Li, M. & Dincă, M., *Chem. Sci.*, **5** (2014), 107–111, "Selective formation of biphasic thin films of metal-organic frameworks by potential-controlled cathodic electrodeposition"
- [105]: Li, M. & Dincă, M., *J. Am. Chem. Soc.*, **133** (2011), 12926–12929, "Reductive Electrosynthesis of Crystalline Metal-Organic Frameworks"
- [106]: Cheng, K.-Y., Wang, J.-C., Lin, C.-Y., Lin, W.-R., Chen, Y.-A., Tsai, F.-J., Chuang, Y.-C., Lin, G.-Y., Ni, C.-W., Zeng, Y.-T. & Ho, M.-L., *Dalton Trans.*, **43** (2014), 6536–6547, "Electrochemical synthesis, characterization of containing coordination polymer, and application in oxygen and glucose sensing"
- [107]: Campagnol, N., Van Assche, T., Boudewijns, T., Denayer, J., Binnemans, K., De Vos, D. & Fransaer, J., *J. Mater. Chem. A*, **1** (2013), 5827–5830, "High pressure, high temperature electrochemical synthesis of metal-organic frameworks: films of MIL-100 (Fe) and HKUST-1 in different morphologies"
- [108]: Ameloot, R., Stappers, L., Fransaer, J., Alaerts, L., Sels, B. F. & De Vos, D. E., *Chem. Mater.*, **21** (2009), 2580–2582, "Patterned growth of metal-organic framework coatings by electrochemical synthesis"
- [109]: Hod, I., Bury, W., Karlin, D. M., Deria, P., Kung, C. W., Katz, M. J., So, M., Klahr, B., Jin, D., Chung, Y. W., Odom, T. W., Farha, O. K. & Hupp, J. T., *Adv. Mater.*, **26** (2014), 6295–6300, "Directed growth of electroactive metal-organic framework thin films using electrophoretic deposition"
- [110]: Zhuang, J. L., Ar, D., Yu, X. J., Liu, J. X. & Terfort, A., *Adv. Mater.*, **25** (2013), 4631–4635, "Patterned deposition of metal-organic frameworks onto plastic, paper, and textile substrates by inkjet printing of a precursor solution"
- [111]: Pullen, S., Fei, H., Orthaber, A., Cohen, S. M. & Ott, S., *J. Am. Chem. Soc.*, **135** (2013), 16997–17003, "Enhanced Photochemical Hydrogen Production catalyzed by a Molecular Catalyst Incorporated into a Metal-Organic Framework"
- [112]: Bala, S., Bhattacharya, S., Goswami, A., Adhikary, A., Konar, S. & Mondal, R., *Cryst. Growth Des.*, **14** (2014), 6391–6398, "Designing Functional Metal – Organic Frameworks by Imparting a Hexanuclear Copper-Based Secondary Building Unit Specifying Properties: Structural Correlation With Magnetic and Photocatalytic Activity"
- [113]: Liu, Y., Yang, Y., Sun, Q., Wang, Z., Huang, B., Dai, Y., Qin, X. & Zhang, X., *ACS Appl. Mater. Interfaces*, **5** (2013), 7654–7658, "Chemical adsorption enhanced CO₂ capture and photoreduction over a copper porphyrin based metal organic framework"

- [114]: Sumida, K., Rogow, D. L., Mason, J. a., McDonald, T. M., Bloch, E. D., Herm, Z. R., Bae, T. H. & Long, J. R., *Chem. Rev.*, **112** (2012), 724–781, "Carbon dioxide capture in metal-organic frameworks"
- [115]: Poloni, R., Lee, K., Berger, R. F., Smit, B. & Neaton, J. B., *J. Phys. Chem. Lett.*, **5** (2014), 861–865, "Understanding Trends in CO₂ Adsorption in Metal-Organic Frameworks with Open-Metal Sites"
- [116]: Fracaroli, A. M., Furukawa, H., Suzuki, M., Dodd, M., Okajima, S., Gándara, F., Reimer, J. a. & Yaghi, O. M., *J. Am. Chem. Soc.*, **136** (2014), 8863–8866, "Metal-organic frameworks with precisely designed interior for carbon dioxide capture in the presence of water"
- [117]: Kim, S. H., Kim, K. H. & Hong, S. H., *Angew. Chem. Int. Ed.*, **53** (2014), 771–774, "Carbon dioxide capture and use: Organic synthesis using carbon dioxide from exhaust gas"
- [118]: Chen, Z., Dinh, H. N. & Miller, E., *CHIMIA International Journal for Chemistry*, (Springer, 2013), doi:10.1007/978-1-4614-8298-7, "Photoelectrochemical Water Splitting"
- [119]: Cassano, A. E. & Alfano, O. M., *Catal. Today*, **58** (2000), 167–197, "Reaction engineering of suspended solid heterogeneous photocatalytic reactors"
- [120]: Motagh, M., Cen, J., Appel, P. W., van Ommen, J. R. & Kreutzer, M. T., *Chem. Eng. J.*, **207-208** (2012), 607–615, "Photocatalytic-reactor efficiencies and simplified expressions to assess their relevance in kinetic experiments"
- [121]: Motagh, M., Ruud van Ommen, J., Appel, P. W., Mudde, R. F. & Kreutzer, M. T., *Chem. Eng. Sci.*, **100** (2013), 506–514, "Bubbles scatter light, yet that does not hurt the performance of bubbly slurry photocatalytic reactors"
- [122]: Ruckebusch, C., Sliwa, M., Pernot, P., de Juan, a. & Tauler, R., *J. Photochem. Photobiol. C Photochem. Rev.*, **13** (2012), 1–27, "Comprehensive data analysis of femtosecond transient absorption spectra: A review"
- [123]: Martiniani, S., Anderson, A. Y., Law, C., O'Regan, B. C. & Barolo, C., *Chem. Commun.*, **48** (2012), 2406, "New insight into the regeneration kinetics of organic dye sensitised solar cells"
- [124]: Cherepy, N. J., Liston, D. B., Lovejoy, J. A., Deng, H. & Zhang, J. Z., *J. Phys. Chem. B*, **102** (1998), 770–776, "Ultrafast Studies of Photoexcited Electron Dynamics in γ - and α -Fe₂O₃ Semiconductor Nanoparticles"

Appendix

A1: List of chemicals

Table A1: List of chemicals used in this work.

Description	Acronym	Supplier	Weight (g/mol)	Purity
Zirconium(IV)chloride	ZrCl ₄	Sigma-Aldrich	233.04	99.5+%
Copper(II)chloride	CuCl ₂	Merck-Schuchardt	134.45	Not available
Cobalt(II)chloride hexahydrate	CoCl ₂ · 6H ₂ O	Acros Organics	237.93	Pro analysis
Titanium(IV) n-butoxide	Ti(O-Bu) ₄	Sigma-Aldrich	340.32	97%
2-aminoterephthalic acid	ATA	Aldrich	181.15	99%
2,5-dihydroxyterephthalic acid	DHTA	Aldrich	198.13	98%
1,4-Diazabicyclo[2.2.2]octane	DABCO	Alfa Aesar	112.17	98%
Dimethylformamide	DMF	Acros Organics	73.09	99+%
Acetonitrile	MeCN	Sigma-Aldrich	41.05	99.8%
Hydrochloric acid	HCl	Emsure	36.46	Fuming 37% in water
Sodium hydroxide	NaOH	Emsure	40.00	99+%
Acetic acid	AcOOH	Acros Organics	60.05	99.8%
Ethanol	EtOH	Interchem	46.07	100% (Technical grade)
Methanol	MeOH	Interchem	32.04	100% (Technical grade)
Acetone	Acetone	Interchem	58.08	100% (Technical grade)
Polyethylene glycol	PEG	Sigma-	Average	Not

Description	Acronym	Supplier	Weight (g/mol)	Purity
diacrylate (average $M_n = 700$)		Aldrich	3.1×10^4	available
Silver nitrate	AgNO_3	Sigma-Aldrich	169.87	99+%
Tertbutylammonium bromide	TBAB	Acros Organics	322.37	99+%
Sodium nitrate	NaNO_3	Sigma-Aldrich	84.99	99+%
Monosodium dihydrogen phosphate	NaH_2PO_4	Sigma-Aldrich	119.98	99+%
Disodium monohydrogen phosphate	Na_2HPO_4	Sigma-Aldrich	141.96	99+%

Appendix A2: Cyclic Voltammetry on FTO

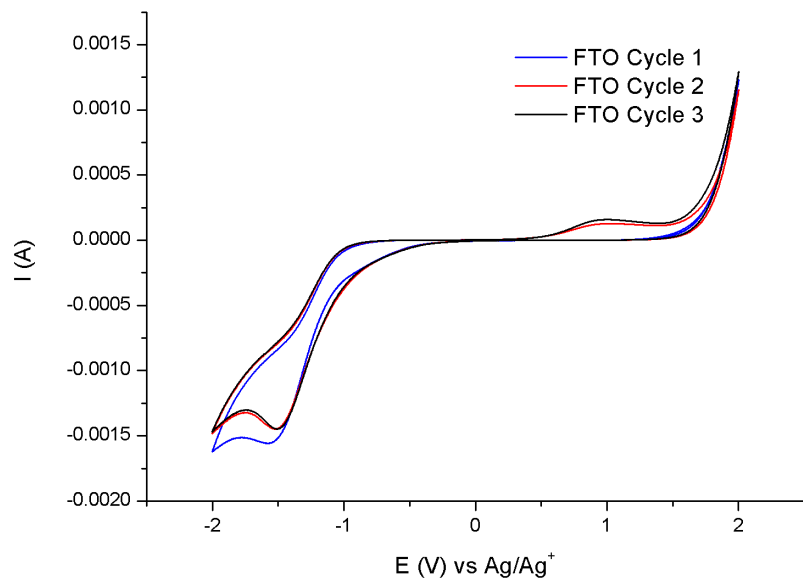


Figure A.1: CV of bare FTO, for 3 cycles in the dark. This measurement is performed in an MeCN based electrolyte with a non-aqueous Ag/Ag^+ reference electrode.

Appendix A3: Transient absorption spectroscopy

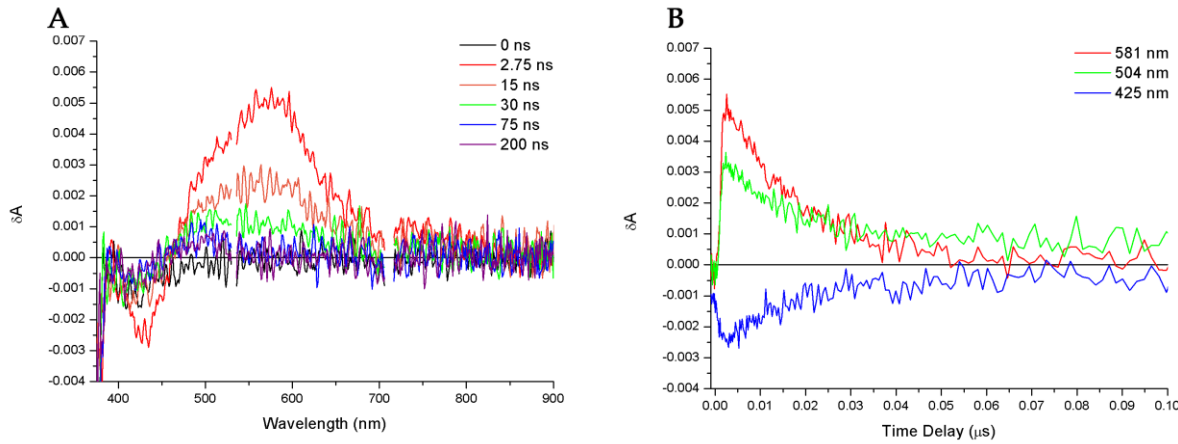


Figure A.2: TAS of data Cu(DABCO)(ATA), Bat-11. In A representative spectra are shown at different time delays. B gives the kinetic traces at different wavelengths.

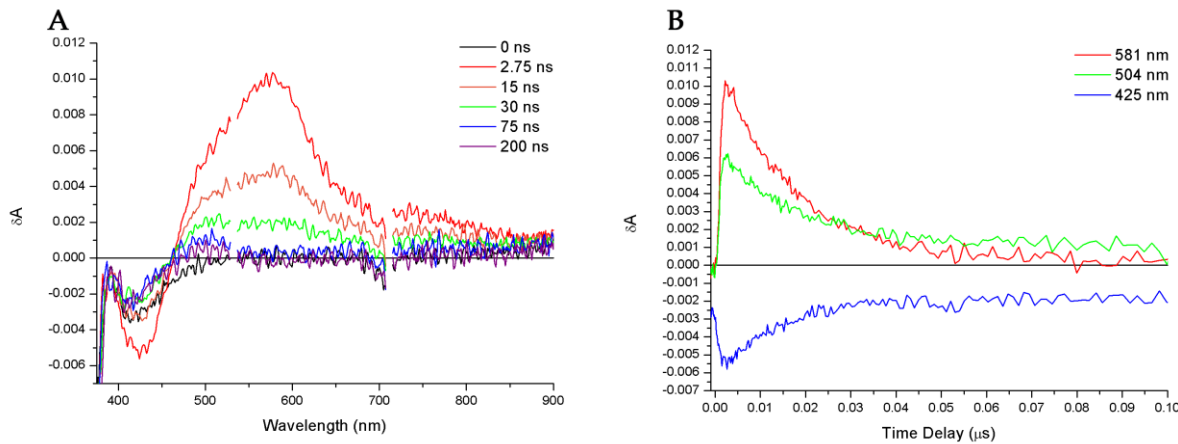


Figure A.3: TAS of data Cu(DABCO)(ATA), Bat-16 before purging with N_2 . In A representative spectra are shown at different time delays. B gives the kinetic traces at different wavelengths.

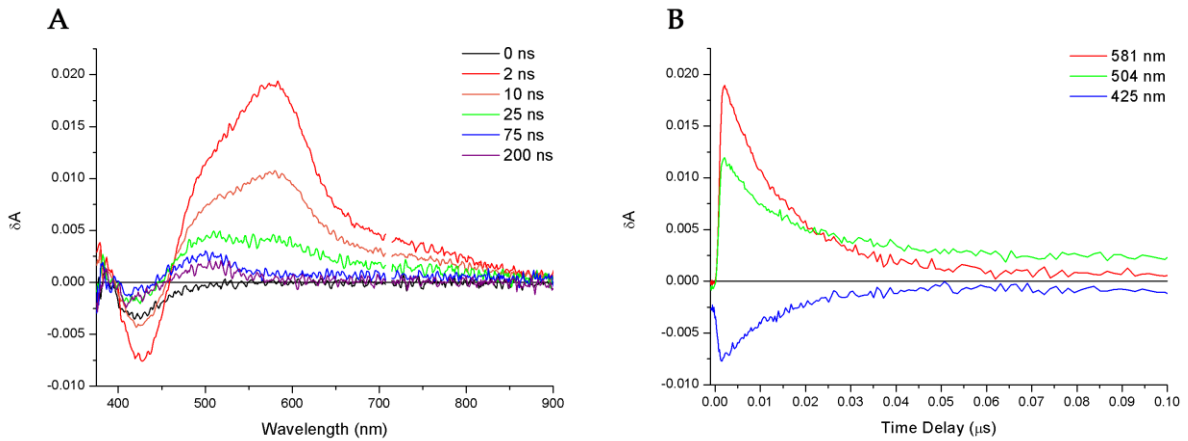


Figure A.4: TAS of data Co(DABCO)(ATA), Bat-18. In A representative spectra are shown at different time delays. B gives the kinetic traces at different wavelengths.

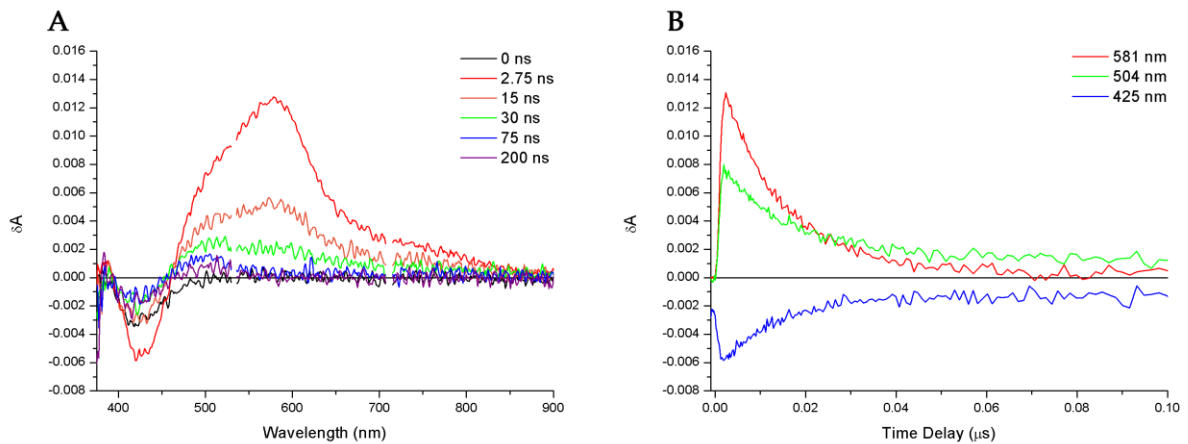


Figure A.5: TAS of data Co(ATA), Bat-17 before purging with N₂. In A representative spectra are shown at different time delays. B gives the kinetic traces at different wavelengths.

